Investigations of impurities in xenon gas with a cold-trap-enhanced quadrupole mass spectrometer

Alexander Fieguth

Master thesis

Institut für Kernphysik
Mathematisch-Naturwissenschaftliche Fakultät
Westfälische Wilhelms-Universität Münster

October 2014

Referent: Prof. Dr. C. Weinheimer

Koreferent: Prof. Dr. A. Khoukaz

WESTFÄLISCHE
WILHELMS-UNIVERSITÄT
MÜNSTER

Eigenständigkeitserklärung

Ich versichere, dass ich die vorliegende Arbeit selbstständig verfasst und keine anderen als die angegebenen Quellen und Hilfsmittel benutzt habe. Die Stellen der Arbeit, die anderen Werken dem Wortlaut oder Sinn nach entnommen wurden, wurden unter Angabe der Quelle kenntlich gemacht.

_____

Ort, Datum   Unterschrift

CONTENTS

Introduction

Various observations of a dominating non-baryonic, non-luminous matter component, the dark matter, induced a theoretical and experimental research for its origin and nature. Among diverse theories for particle candidates accounting for dark matter, the concept of weakly interacting massive particles (WIMPs) is outstanding, due to the possibility of experimental detection with existing technologies. One ambitious project searching for these WIMPs is the XENON dark matter project, using a dual-phase time projection chamber filled with liquid xenon for a possible detection of WIMP-Nucleon scatterings. The XENON collaboration is preparing its next phase, the XENON1T detector, which uses 3 tons of liquid xenon. While the preceding step, XENON100, was a leading experiment in terms of sensitivity and recently has been surpassed by the LUX experiment, the new stage XENON1T will probe a new space for spin-independent WIMP-Nucleon cross sections. A projected sensitivity of $\sigma_{SI} = 2 \cdot 10^{-47} \mathrm{cm}^2$ for a WIMP mass around 50 GeV exceeds the actual sensitivity limit by more than an order of magnitude. The name of the game for achieving new sensitivities is background reduction. One of the main backgrounds within xenon is the krypton isotope ^{85}Kr. This anthropogenic isotope decays with a half-life of 10.76 years, and thus is an intrinsic background not vanishing on a short time scale, which makes a removal necessary. The technique used for depleting the xenon in terms of krypton, is cryogenic distillation. Therefore a cryogenic distillation column is prepared and tested at the University of Münster, which purifies the xenon in terms of krypton down to the desired limit of less than 0.5 ppt. However, not only the reduction but also the knowledge of the background is of great importance. Measuring concentrations of krypton at the sub-ppb level requires technically challenging setups, which are usually working on a large time scale. Therefore, a different technique, using a residual gas analyzer behind a cold trap, providing online results and consuming only a fraction of a standard liter, is presented within this thesis. A mobile setup using this method, which is dedicated to measure directly at the XENON1T facility,

has been designed, built and extensively tested.

This thesis starts with a brief introduction of dark matter and its pieces of evidence. Especially the WIMP will be explained and also the search for it, namely with the XENON dark matter project, which will be introduced. Following this, the krypton background and its detection with different techniques are explained. As the main task of the thesis was the building of a new mobile setup, its design and properties will be explained in detail. Investigative measurements on this and another setup, as well as the calibration method used for this setups will be shown. Furthermore, first concentration determinations of unknown gas samples will be presented as a proof of principle, followed by a completing discussion on the obtained results and an outlook for improvements.

DARK MATTER

During the last century, the composition of the universe became a challenging question for the field of astrophysics and astronomy. While the baryonic fraction is well understood, an overwhelming number of observations since the early 20th century lead to the evidence of existing unknown components, contributing to over 95 % of the present universe energy density. These can be divided into two different types of constituents, namely *dark energy* and *dark matter*. Although providing around 70 % to the energy density of the universe and causing its accelerated expansion, the nature of dark energy remains puzzling, whereas the gravitational influence of dark matter can be observed from the galactic scale to very large and distant structures. Different hypothesis aroused to explain the nature of dark matter, where the theory of weakly interacting massive particles (WIMPs) is outstanding, due to the fact that it is possibly verifiable by different experimental approaches. Furthermore, beside different other theories, the promising supersymmetric theory (SUSY) provides a natural WIMP-candidate.

This chapter will show important examples of evidence for dark matter and introduce the WIMP as a dark matter aspirant. Moreover, the possible detection of dark matter particles will be explained.

(a)   (b)
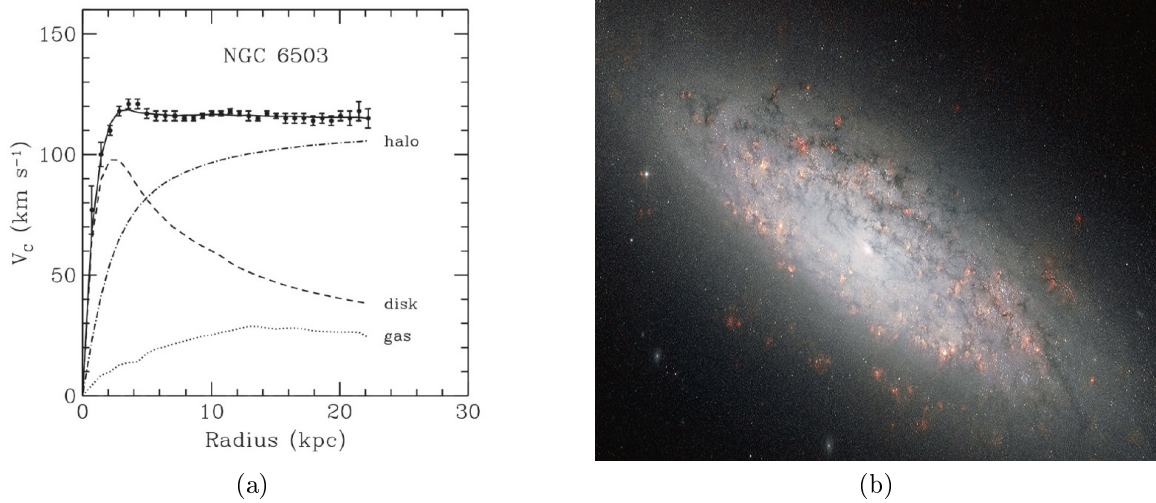
Figure 2.1: (a) Rotational velocity of stars in the spiral galaxy NGC 6503 compared to their
distance to the galactic center. The solid line shows the fitted data, while the
expected distribution is represented by the dashed line. Additional distribution of
gas throughout the galaxy does not explain the discrepancy, while an additional
halo of non-luminous mass (dash-dotted line) can explain the observed velocities
[Beg91]. (b) Spiral galaxy arms of NGC 6503 as observed by the Hubble Space
Telescope [ESA10].

2.1 Evidence for dark matter

Fritz Zwicky observed first traces of dark matter in 1933 by investigating the mass content
of the Coma cluster by measuring the number of its galaxies, their luminosity and kinetic
energy. As a result of this, he observed a significant discrepancy between the luminous mass
and the total mass content, which he obtained by application of the virial theorem [Zwi37]:

$$M_{tot}^2 \ \sim \ \langle E_{pot} \rangle = -2 \langle E_{kin} \rangle \ \sim \ v_{kin}^2 \tag{2.1}$$

The idea of hidden mass as an explanation for this discrepancy was not directly accepted as
a viable concept, although the following years brought further supporting observations (e.g.
mass-light-ratio in the Andromeda nebula by H. Babcock [Bab39]).

2.1.1 Galactic rotational velocity curves

New spotlight to the idea of existing hidden mass was given in the 1970s, when Vera Rubin
evaluated systematically the rotational velocities of stars at the edge of spiral galaxies with
high precision by measuring the Doppler shifted 21 cm hyperfine transition line of hydro-
gen.

Due to the fact that most of the luminous mass is centered in the bulge, and the assumption that the gravitational mass M matches this luminous mass, it was expected that the stars have a decreased rotational velocity v_{rot} in dependence of the distance r according to Newtonian dynamics:

$$v_{rot} = \sqrt{\frac{GM(r)}{r}} \tag{2.2}$$

However, the observation has not shown the expected drop with $\sim \frac{1}{\sqrt{r}}$ but an almost constant rotational velocity for large radii, independent of the distance to the mass center (see figure 2.1). This points to a different mass distribution than the luminous one, which can be explained if a dark matter halo is added to the model.

2.1.2 Gravitational lensing

In the framework of general relativity theory, the effect of gravitational lensing provides a powerful tool for mass astronomy and hence for observation of non-luminous matter. Light rays of any source in the universe are deflected by the gravitational fields created by matter in their path towards us, where the deflection angle is directly depending on the mass content. This way the mass of objects, acting as a lens for passing light rays, can be determined.

The Bullet Cluster

An impressive application of gravitational lensing is shown at observations of the Bullet Cluster, which strongly supports the concept of dark matter.
As seen in figure 2.2, the Bullet Cluster actually consists of two clusters, which collided in the past. Evidence for that is given by the fact that x-ray spectroscopy of the hot gas, the main fraction of the galaxy's baryonic mass, reveals a shockwave-like shape of the smaller galaxy when passing through the larger one. Unlike the point-like stars, which pass almost
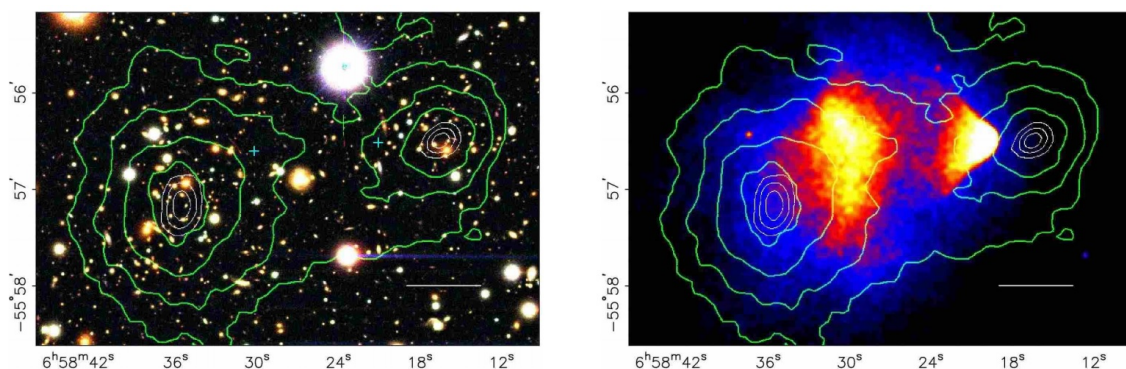

Figure 2.2: *Map of the gravitational potential (green contours), obtained from gravitational lensing, comparing the distribution of visible galaxies (left panel) and the hot gas distribution measured by the x-ray telescope Chandra (right panel)[Clo06].*

unaffected, the hot gas is diffusely spread and consequently friction takes place causing it to slow down. Classically it would be expected that the gravitational center is consistent with the center of baryonic mass at the hot gas. Nevertheless, surveys of the gravitational potential, using gravitational lensing, point to a gravitational center, consistent with a mass center unaffected by the collision. Since the stars clearly have less mass than the gas, it is an indication for additional mass, which has a low cross section for interactions with the hot gas and itself, pointing to a non-luminous and weakly interacting nature [Clo06]. This technique has also been applied to further galaxies supporting these observations (e.g. [Bra08]).

2.1.3 Cosmic Microwave Background (CMB) radiation

Additional support to the theory of dark matter and also further understanding of its nature is provided by the cosmic microwave background(CMB) radiation. This uniformly spread $2.73\,\mathrm{K}$ radiation fingerprint of the decoupling of photons from baryonic matter, $380\,000$ years after the big bang, reveals detailed information about the consistence of the universe. More precisely, small fluctuations on the μK-level in the macroscopic isotropic radiation, developed into an angular power spectrum (see figure 2.3), provide data for the total energy density and its components. According to recent measurements of the Planck satellite[1], the contribution of matter to the total energy density is about $31.7\,\%$, while the fraction of baryonic matter is only about $4.9\,\%$. Thus, over $80\,\%$ of the matter content has to be non-baryonic matter [Pla13a], which clearly points towards physics beyond the standard model, since it does not contain a viable explanation for this discrepancy.
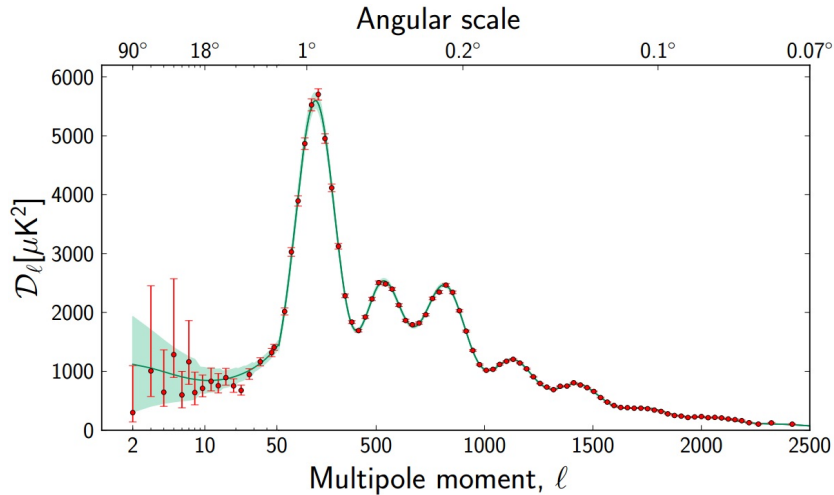
Figure 2.3: *The angular power spectrum of the CMB. A multipole moment ℓ development of the temperature fluctuations (D_ℓ) is shown with an additional angular scale. For small multipole moments below 50 the plot is linear, while for large multipole moments it has a logarithm scale. The fit (green) to the data is based on the ΛCDM model, which represents the standard cosmological model [Pla13b].*

---

[1] These results are not completely matching the past results from WMAP and are still disputed, but the difference is only in within few percent, so the general statement is confirmed.

2.2 Nature of dark matter

As previously described the concept of dark matter relies on strong observational evidence and is hence favored in modern physics, but the nature of dark matter is a heavily discussed topic. Alternatively discussed theories without additional non-baryonic matter, as for example the Modified Newtonian Dynamics (MoND), are almost ruled out since they fail for instance at explaining interactions at the Bullet Cluster [Clo06].
Considering the fact that dark matter is not detected so far, it can be assumed that dark matter particles are interacting possibly only through weak interaction, besides the proven gravitational influence, and not strongly or electromagnetically. Classically, particle candidates for dark matter are divided by their velocities into hot dark matter (HDM), moving close to the speed of light at relativistic velocities, and cold dark matter (CDM), moving with non-relativistic velocities. Structure forming N-body simulations of the early universe showed that the structure observed today fits with a cold dark matter concept [Ho12]. As a result of this, the natural dark matter candidate of the standard model of particle physics, the neutrino, a hot dark matter particle, is ruled out as the main component of dark matter. This is also supported by measurements of the neutrino mass and its abundance, which come to the result that the neutrino is simply not heavy nor abundant enough to account for a large fraction of dark matter [Ber04]. Nevertheless, additional sterile neutrinos could contribute as a warm dark matter (WDM) particle candidate (see section 2.2.2), but have not been detected yet.
Reasonably, the cosmological standard model (ΛCDM) assumes cold dark matter as the dominating component of the matter universe, although there are still fundamentally open questions, e.g. the discrepancy of dwarf galaxies abundances [Kuz08].

2.2.1 Weakly Interacting Massive Particles (WIMPs)

Although WDM (see next section) is possibly an alternative explanation, the main focus of research is set on cold dark matter, since the standard cosmological model proved to be very successful despite the unsolved problems.
A promising concept for CDM particle candidates is the particle class of weakly interacting massive particles (WIMPs). Particles belonging to this class, fulfill the necessary properties dictated by observations. They are massive ($\sim$ GeV), therefore moving with non-relativistic velocities, either long-lived with a lifetime greater than the age of the universe or even stable, and have a cross section scale comparable to the weak interaction. The latter property leads to a coincidence, which is sometimes referred to the "WIMP-miracle". Assuming a thermal production mechanism in the early universe, the relic abundance of a possible dark matter particle $\Omega_{dm}h^2$ is given by (see figure 2.4):

$$\Omega_{dm}h^2 = \frac{3 \cdot 10^{-27}\,\mathrm{cm^3/s}}{\langle \sigma_A v \rangle} \qquad \text{[Gel10]} \qquad (2.3)$$

The natural relic density, as measured today, is dependent on the dark matter particle annihilation cross section $\langle \sigma_A v \rangle$. This is a result of the thermal freeze-out, where the cool-down
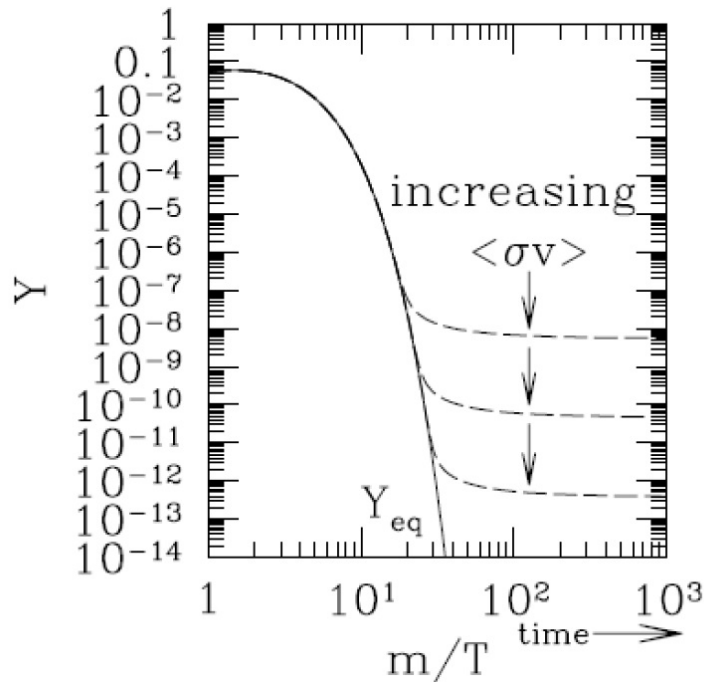
Figure 2.4: *Evolution of the WIMP number density in the early universe following the*
ΛCDM-Model. The solid line represents the equilibrium line, where the den-
sity Y follows the thermal equilibrium Y_{eq}, which means a decreasing density
of particles, due to the cooling of the early expanding universe. At a certain
point, the density is too low for further annihilation, leading to freeze-out of a
specific particle density. This freeze-out is depending on the annihilation rate of
the WIMP (dashed lines) [Gel10].

of the universe stopped the production, but not the annihilation of dark matter particles. It
continued until the density dropped below a certain level, so that the interaction likelihood
became almost zero. For this natural relic density, a weak-like cross section is needed, as
the WIMP model postulates [Jun96]. Another trait of the weak-like cross section is the fact
that it is possibly detectable with particle experiments using ordinary matter.

Supersymmetry (SUSY)

Several theories provide particles fitting the WIMP criteria. One promising theory, extending
the standard model, is the supersymmetry (SUSY). Motivated by unsolved problems of
standard model physics (e.g. the hierachy problem[2]), SUSY suggests an additional symmetry
providing a fermion partner for every boson and vice versa. Due to the absence of these
particles in collider experiments this symmetry must be broken, leading to difference in
masses between the supersymmetric and standard model partners. In its minimal form,
known as the minimal supersymmetric theory (MSSM), a conservation of the R-parity is

---

[2]The hierachy problem describes the unsolved fact that the weak force is much stronger than the gravi-
tational force. Closely related to this is the question, why the mass of the higgs boson is so far off the Planck
scale.

required, resulting in a stable suypersymmetric particle, referred as the lightest stable particle (LSP). This LSP is a natural dark matter candidate, fulfilling the properties of a possible WIMP. For deeper understanding literature is widely available, as for instance information can be found in [Jun96].

2.2.2 Warm dark matter?

Recently, focus started growing for an in-between solution, called warm dark matter (WDM), where particles with masses in the keV regime are introduced as possible dark matter candidates. This arose from the fact that different aspects of the N-body simulations with cold dark matter showed some discrepancies, e.g. the number of dwarf galaxies in the present universe.

A viable candidate for WDM is the sterile neutrino, which is, in contrast to the standard model particle neutrinos, not charged under the weak interaction. This hypothetical particle was introduced at the explanation of the non-zero mass of standard model neutrinos, but could additionally explain dark matter since it fulfills the required properties. Also, it is possibly stable and interacts only gravitationally with ordinary matter, which limits its detectability. Although, recent observations of an unexpected X-ray line in galaxy clusters, explainable by annihilation of sterile keV-Neutrinos [Bul14], renewed the attention to this topic, various experiments, looking for direct or indirect detection of sterile neutrinos, found no trace of additional neutrinos, which makes this candidate a topic of upcoming research (e.g. in the KATRIN experiment [Esm12]).

2.3 Experimental detection of dark matter
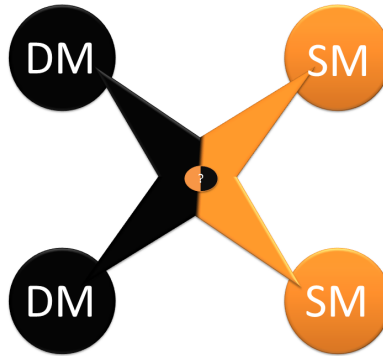
Figure 2.5: *Visualization of the three possible interaction channels between dark matter (black) and standard model(orange) particles. For the WIMP model, the exchange particle is not directly fixed, but favored interactions working through Z-Boson, via Higgs-field interactions, through hypothetical or unkown ways [Kam97].*

As already mentioned, the assumption of thermally produced WIMPs with a weak-scale cross section makes a detection possible via standard model particles. In fact, three possible ways of interaction between dark matter (DM) and standard particle matter (SM) provide detection channels (see figure 2.5):

$$DM + DM \rightarrow SM + SM$$

Here the annihilation, transforms dark matter particles into standard model particles as it occurred in the early universe. This indirect signal could possibly be detected, if the density of dark matter is increased, as it could be the case in the center of galaxies or around black holes.

$$SM + SM \rightarrow DM + DM$$

As in thermal equilibrium, there has to be the possibility that interactions of standard model particles produce dark matter particles. In experimental research this can be probed at large collider providing enough energy for creating a massive dark matter particle, where the detection is registered as missing mass and momentum.

$$DM + SM \rightarrow DM + SM$$
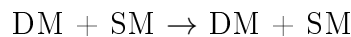
Interaction of dark matter particles directly with standard model particles could be possible, for example through exchange of Z-Bosons or interaction via the Higgs-field. Detection of this channel could possibly be achieved, by measuring the energy deposition of a colliding dark matter particle in a low-background detector, assuming a surrounding halo of dark matter in our solar system.

ENLIGHTENING THE DARK - THE XENON DARK MATTER PROJECT

Out of the three described potential detection channels, the direct detection approach for WIMPs is one of the favored in recent research. Therefore, a broad spectrum of possible detector designs, based on different materials, is set up for direct detection experiments. As seen in figure 3.1, there are basically three ways to measure the energy deposition of WIMPs, scattering off ordinary matter, namely heat, charge and light. For a proper signal-background discrimination, two different signal channels are advantageous. Additionally, experiments exist, using only one channel, e.g. the DAMA/Libra experiment with the scintillation channel of NaI only. However, such experiments gain additional information by checking the signal for an annual modulation, as it is expected, if the earth moves through a dark matter halo during a solar year. Although the DAMA/Libra collaboration claims to see this signal, the outcome is heavily disputed, since many other two-channel experiments come to contradictory results [Bel08].

Experiments, which use two channels for detection, can be divided basically into two main fractions:

On the one hand, there are cryogenic bolometer experiments (e.g. EDELWEISS, CDMS), which measure at ultra-cold temperatures ($\mathcal{O} \sim \mathrm{mK}$) the heat and charge signals in high-purity semiconductors, as e.g. germanium. On the other hand, there are liquid noble gas detectors filled with xenon looking for light and charge signals (e.g. LUX and XENON), which are leading experiments for spin-independent WIMP-nucleon scattering (see figure 3.2).
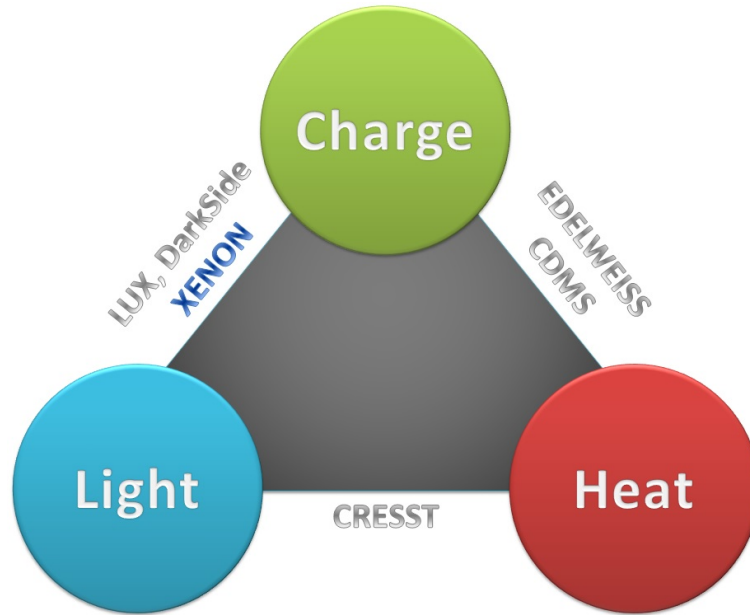
Figure 3.1: *Scheme of three possible ways to detect an energy deposit of a colliding WIMP and the respective examples of direct detection experiments, enclosed by their chosen signal channels.*

The use of liquid xenon provides different advantages as:

- A high atomic number with $Z = 54$ provides self-shielding of external backgrounds.

- No short-lived radioactive isotope[1].

- Scintillation light of 178 nm VUV-light detectable with photomultiplier tubes without a wavelength shift.

- Transparency for its own scintillation light, due to excimer production.

- Even and odd isotopes at about the same abundance provide sensitivity, not only to spin-independent, but also to spin-dependent scattering.

- easy cryogenics, as the temperature of liquid xenon is around 178 K

- An ability to enlarge the scale of experiments without strong disadvantages.

In the following chapter, the direct detection approach of the XENON Dark Matter Project, which was successfully applied within the XENON10 and XENON100 experiment and is prepared for the upcoming XENON1T experiment, will be explained in detail. Additionally difficulties in the background reduction and measurement, where this thesis contributes towards the project, will be explained.

---

[1]The only radioactive isotope is ^{136}Xe, which decays trough double-beta decay with a half-life of about $2.11 \cdot 10^{21}$ y [Exo11].
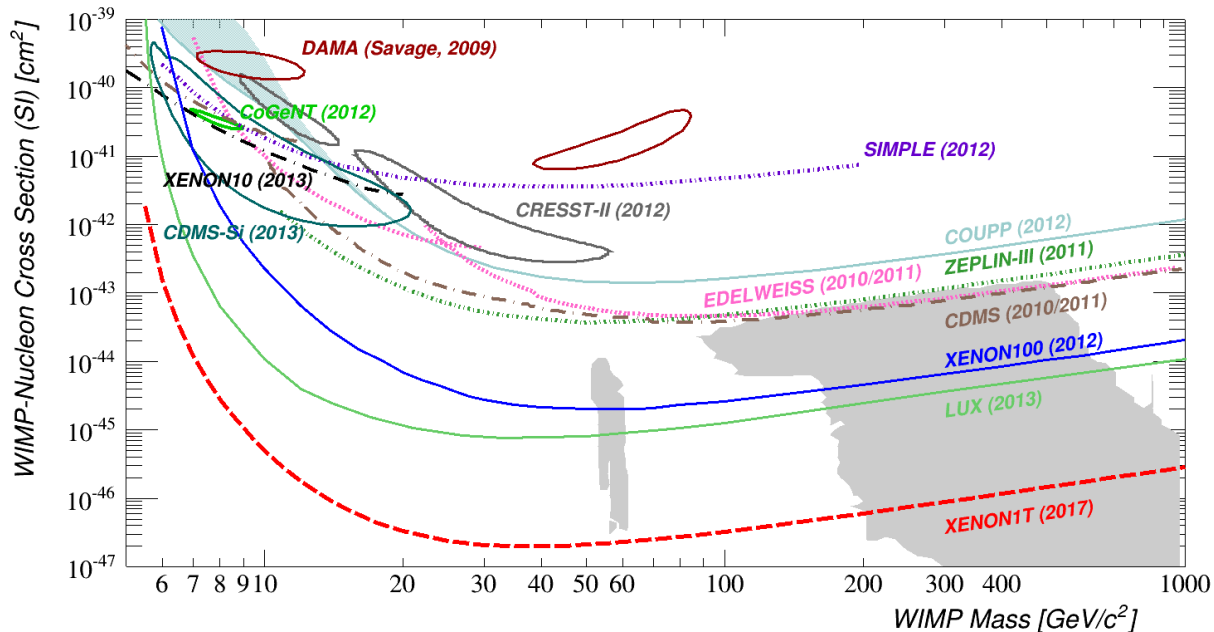
Figure 3.2: *Experimental results on spin-independent cross section limits in dependence of the WIMP mass. A projection for the XENON1T experiment, surpassing the leading experiment LUX by up to two orders of magnitude, is also added. Theoretical expected values from supersymmetry are indicated by the grey shaded area. Figure in courtesy of the XENON collaboration.*

3.1 Detection principle

The detection of any interaction with xenon particles is based on the understanding of the signal production, identification of the signal origin, as well as a suitable detector technology for proper registration of the signals. Especially the discrimination of various signal sources (e.g. the difference between WIMP-nucleon interactions and background signals) is essential for an actual dark matter particle detection.

3.1.1 The origin of signals

If a WIMP, from the assumed dark mater halo in our galaxy, scatters off a xenon nucleus, two different mechanisms, ionization and scintillation, take place, producing signals detectable by suiting detector technology.

The underlying process for a direct scintillation signal starts with the scattering-induced excitation of a xenon atom [Apr09]:

$$\text{Xe}^* + \text{Xe} \rightarrow \text{Xe}_2^*$$
$$\text{Xe}_2^* \rightarrow 2\text{Xe} + h\nu \tag{3.1}$$

Due to the creation of an excimer, the xenon itself is transparent to the emitted light at de-excitation. Additionally, another process exists, ionizing the xenon primarily:

$$\text{Xe}^+ + \text{Xe} \rightarrow \text{Xe}_2^+$$
$$\text{Xe}_2^+ + e^- \rightarrow \text{Xe}^{**} + \text{Xe}$$
$$\text{Xe}^{**} \rightarrow \text{Xe}^* + \text{heat} \tag{3.2}$$
$$\text{Xe}^* + \text{Xe} + \text{Xe} \rightarrow \text{Xe}_2^* + \text{Xe}$$
$$\text{Xe}_2^* \rightarrow 2\text{Xe} + h\nu$$
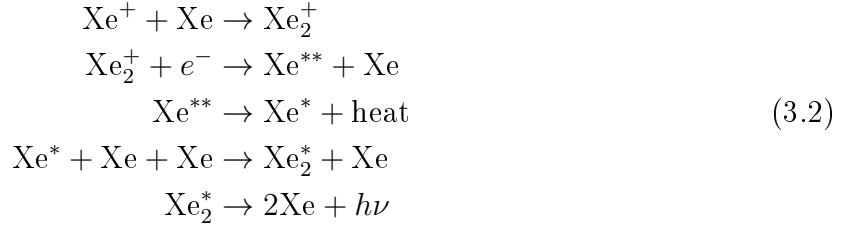
As equation 3.2 shows, this process ends in emission of a photon if recombination occurs directly, producing also a scintillation light signal. Consequently, to fulfill the need of two different signal channels, it is straightforward to make use of the ionization signal. This can be achieved by separating the electrons before recombination takes place and measuring their charge. However, since an expected energy deposit of a few keV per interaction would only produce a very faint ionization signal, it is necessary to implement an amplification of this signal, as described in the following section.

3.1.2 Detecting signals - the dual phase time projection chamber (TPC)

A powerful technology for maximizing information gain from the scattering, is the dual phase time projection chamber. This detector principle (see figure 3.3) makes use of a cylindrical detection chamber, consisting of polytetrafluoroethylene (PTFE) for high VUV-light reflectivity (see [Lev14] for more details), which is filled with liquid xenon, but additionally, a gaseous phase of xenon is constantly kept above the liquid.
If an incoming WIMP scatters off a xenon nucleus, the processes described in equation 3.1 and equation 3.2 produce directly scintillation photons with a wave length of 178 nm, which is registered by optimized photomultiplier tube (PMT) arrays on the top and the bottom of the TPC as a so called S1-signal.
Furthermore, two electric fields for collection of the electrons produced by the ionization channel (see equation 3.2) of the scattering are applied along the detector. First, there is a constant drift field pointing towards the gaseous phase, where secondly, a stronger extraction field takes over, accelerating the electrons into the gaseous phase, where an electron avalanche produces a secondary light signal (S2-signal). This second signal, produced direct below the top PMT array, allows for a precise position determination in the x-y-plane and the time distance between the S1 and S2 signal provides information about the z-position of the scattering. For a more detailed description of the working principle of a dual phase TPC see [Sch11].
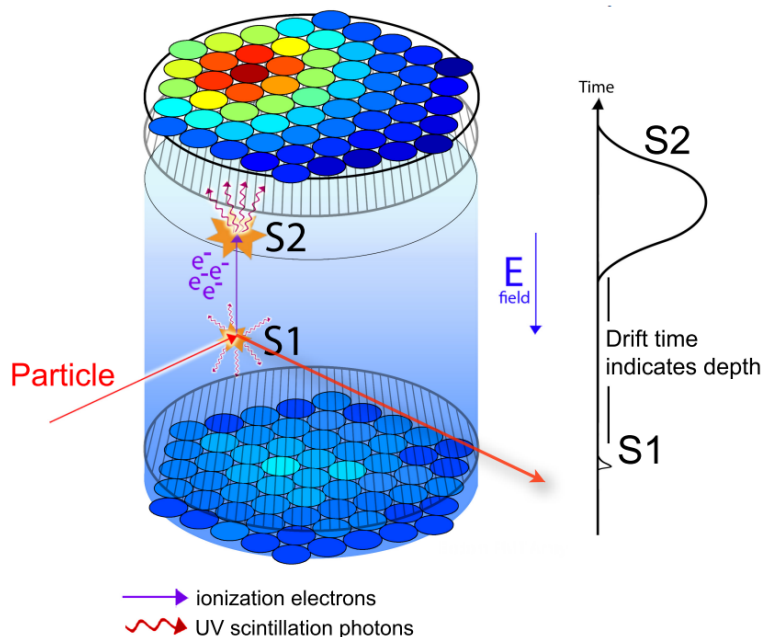
Figure 3.3: *Visualization of the signal production in a TPC. A particle interacting with the xenon nuclei firstly produces prompt scintillation light (S1) as shown in eq. 3.1 and also electrons due to ionization (see eq. 3.2). As a result of the applied electric field, which interrupts the recombination of electrons and nuclei, the produced electrons are guided to the gaseous phase, where an additional strong electric field extracts and accelerates them, leading to a secondary scintillation signal (S2). While direct detection of this signal, close to the top PMT array, allows for position reconstruction in the x-y-plane, the information about the z-coordinate (depth,) is obtained from the time difference between the S1 and S2 signal (shown on the right), thus completing a total 3-D reconstruction of the scattering. Figure taken from [LUX13a].*

3.1.3 Background signals

A key factor for dark matter detection lies in the understanding and suppressing of background signals, caused by particles from external or internal sources. External sources can be divided into two components - external background from radioactive materials surrounding the detector and external background induced by cosmic rays and air shower particles.

Due to the absence of a short-lived radioactive xenon isotope, the main fraction of intrinsic background signal sources are impurities like krypton and radon. While the latter one has four abundant short-lived isotopes, with the isotope ^{222}Rn as main contributor ($t_{1/2} \sim 3.8\,\text{d}$), krypton naturally has no radioactive isotope. Nevertheless, the isotope ^{85}Kr exists in traces since the last century, as a result of human-induced nuclear fission.

Controlling the background is possible through two different ways. First, the removal of background, either externally by expedient material selection and shielding, or internally by purification is a feasible option (details in chapter 4). Secondly the analysis of a signal itself provides possibilities of discrimination between background induced signals and WIMP-like signals. One possibility arises due to the different energy deposition of scatterings induced

by a nuclear recoil, as a WIMP or a neutron would produce, or by an electronic recoil, as a gamma or beta particle would produce, which leads to a different ratio of the S1/S2 signal (for more details see [Apr11]).

3.2 XENON10, XENON100 and XENON1T - dark matter experiments
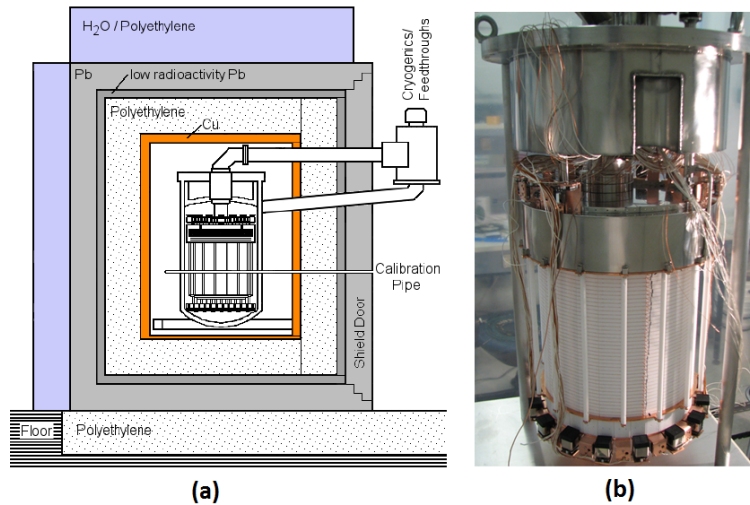
Figure 3.4: *(a) Sketch of the TPC as it is installed into the passive shielding at LNGS. (b) Picture from the assembled XENON100 detector with its PTFE structure. Figures from [Apr12b] and in courtesy of the XENON collaboration.*

In 2007 the XENON10 experiment set the best limit on a possible WIMP-nucleon cross section σ for spin-independent scattering at that time, proving that liquid noble gas detectors are highly competitive. This first experiment used a time projection chamber (TPC) detector design, as described in 3.1.2, filled with around 15 kg xenon. For reduction of the muon flux, it was located in 3600 mwe (meter water equivalent) depth at the Gran Sasso National Laboratory (LNGS) [Ang08].

As a follow-up, the XENON100 experiment started taking data in 2009 at LNGS. It reached its scientific goal in 2012, providing a new limit on the spin-independent cross section σ_{SI} for WIMP masses above 8 GeV with a minimum of $< 2.0 \times 10^{-45}\,\text{cm}^2$ for 55 GeV-WIMPs with a 90 % confidence level [Apr12a].

This experiment-stage uses a detector (see figure 3.4) filled with about 165 kg, where only a fraction of ~ 64 kg are used as active target material, while the other xenon is used as an active veto shield, embedded into different shielding layers consisting of copper, polyethylene, lead and water. Additionally, only a certain portion of the active target, the so called fiducial volume, is used for the actual WIMP-nucleon interaction search, chosen accordingly to benefit from the self-shielding, while maintaining as high statistics as possible.

3.2.1 XENON1T

Figure 3.5: *Schematic illustration of the XENON1T detector and its position inside the Hall B at LNGS. As seen on the right part the cryostat with the embedded TPC is surrounded by a 9.6 m diameter water tank, while the supporting structure is outsourced to the structure building, directly next to it. Figure in courtesy of the XENON collaboration.*

The upcoming next step - start of scientific data taking is planned for 2015 - is the XENON1T experiment. Designed for above three tons of xenon, with about one ton of fiducial volume, its scientific goal for the spin-independent cross section is at

$$\sigma_{SI} = 2 \cdot 10^{-47} \text{cm}^2$$

for WIMPs with a mass of 50 GeV. This would surpass actual limits by more than an order of magnitude (see figure 3.2).

The increased sensitivity of the detector is essentially limited by the level of background signals. Thus, especially the intrinsic background removal and monitoring is of crucial importance, since the external sources are already reduced by the additional self-shielding of xenon, careful selection of low-radioactive materials for the detector and the new active muon-veto, which consists of a water tank around the cryostat equipped with PMTs, for detection of muon-induced Cherenkov radiation [Apr14].

Removal and detection of ^{85}Kr

Internal backgrounds, as radon and krypton (see section 3.1.3), influence the sensitivity of the XENON1T detector drastically. Hence, large effort is put into three possible ways of dealing with this background sources:

1. Screening of the used material to avoid contamination.

2. Removal of the intrinsic impurities.

3. Determination of the impurity concentration level.

All three processes are applied on radon and krypton, but the focus of this work is set on the treatment of the krypton impurity. For a detailed description of radon screening, detection and removal see [Lin13].
This chapter will provide general information about the isotope ^{85}Kr, its removal and possible detection methods.

4.1 Krypton as a background source

Introduced by nuclear bomb tests in the last century, and since then constantly produced by nuclear reprocessing (see figure 4.1), the radioactive isotope ^{85}Kr is present today due to its half-life of $\sim 10.8\,\mathrm{y}$ with a measured concentration at the Gran Sasso National Labratory of about

$$\frac{^{85}\mathrm{Kr}}{^{nat}\mathrm{Kr}} \approx 2 \times 10^{-11}\,\mathrm{mol/mol} \quad [\mathrm{Du03}].$$
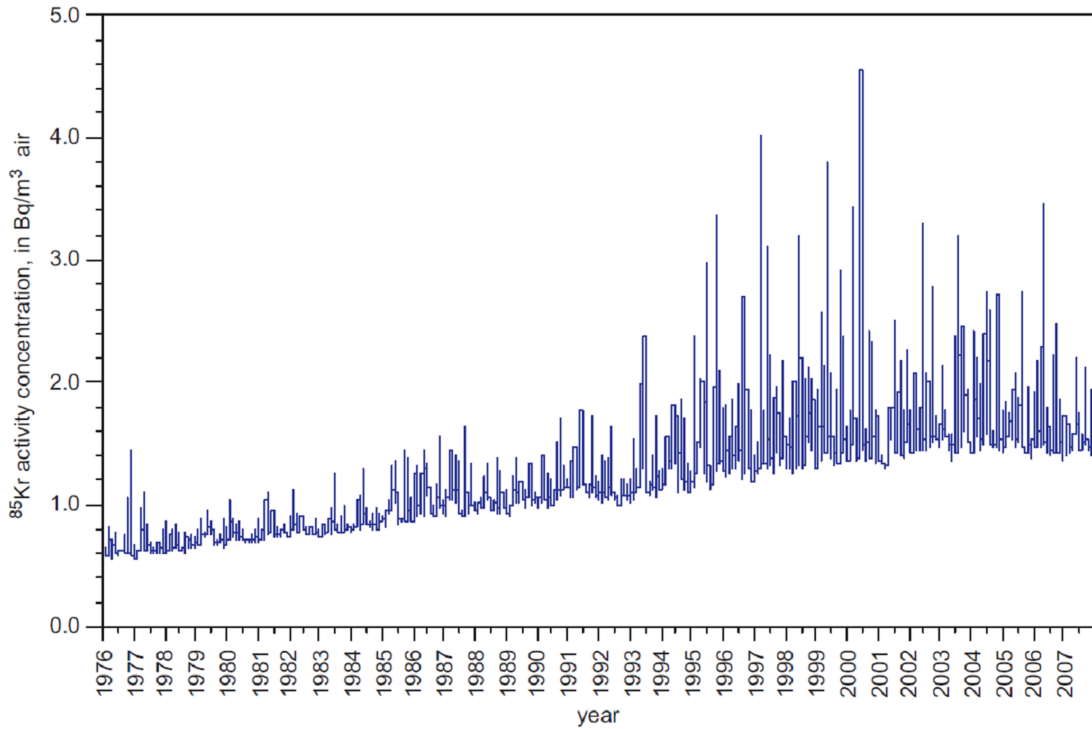
Figure 4.1: *Measurement of the ^{85}Kr activity in air samples taken at Mount Schauinsland. While the present level stays constant at about $1.5\,\mathrm{Bq/m^3}$, occasional spikes in the activity are caused by nuclear reprocessing in La Hague [Bie09].*

This β^- emitting isotope decays mainly (99.6 %) into ^{85}Rb, releasing an electron with an endpoint energy of 687 keV (see figure 4.2). Although, it would produce only an electronic recoil, which differs from the nuclear recoil a WIMP would produce, the detectors discrimination capability is not perfect, since the actual value for the S1/S2 discrimination at XENON100 is at roughly 99.5 % [Sel12], which makes a misinterpretation as a dark matter signal possible [Apr11].
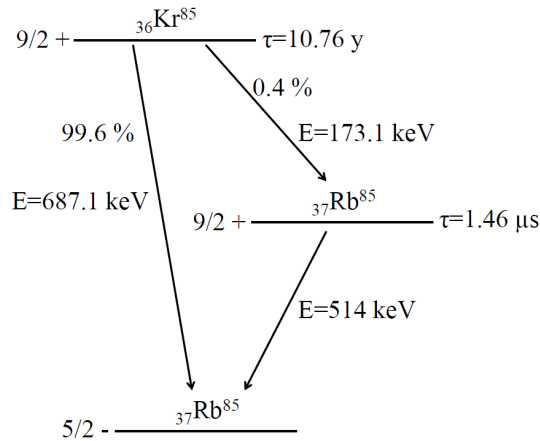
Figure 4.2: *Decay scheme of ^{85}Kr. Values from [Apr12b]*

Number of background events as a function of the Kr contamination in LXe
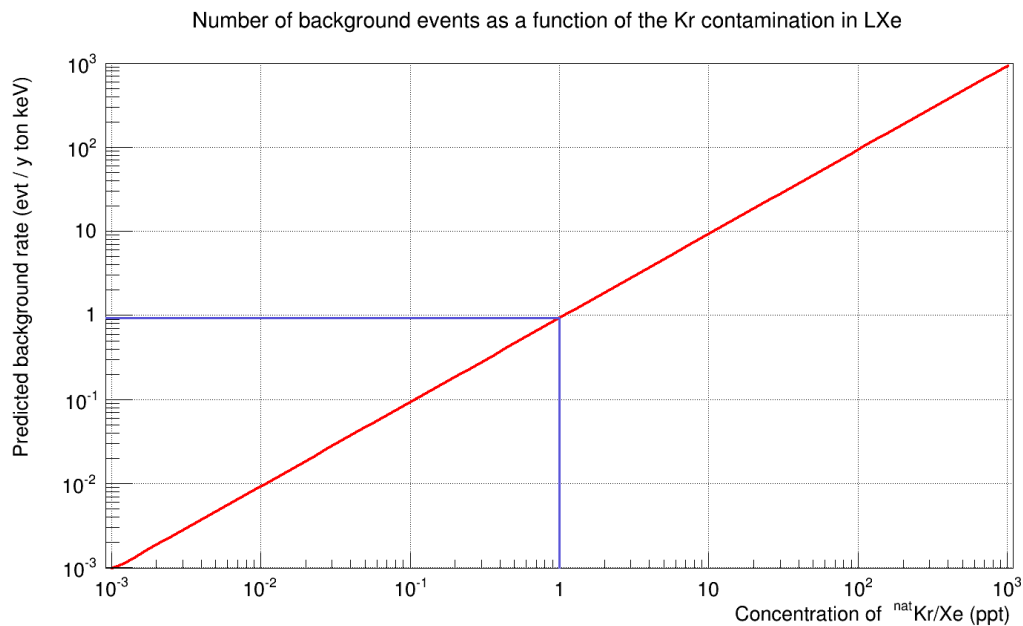
Figure 4.3: *The dependence of the background event in terms of time, mass and energy from the ratio of natural krypton in xenon is shown (red). Assuming a concentration of 1 ppt, a number of about one background event per year, ton and keV is expected (blue). Figure and caption from [Mur14].*

Using the constant ratio of ^{85}Kr compared to natural krypton, one can derive the amount of events that will be detected as WIMP-like signals for a certain natural krypton concentration. According to figure 4.3, an intrinsic concentration of 1 ppt[1] would correspond to about 1 event per ton of detector material, year of exposure and per keV energy of the β-particle. The 1 ppt concentration is set as the upper limit for the upcoming XENON1T experiment [Apr10], but even the most pure commercially available xenon gas has concentrations up to 10 ppb[2]. Consequently, a further purification is necessary, where the cryogenic distillation provides various advantages and is therefore the chosen method for the XENON100 and XENON1T experiments.

4.2 Removal with cryogenic distillation

A direct way of ^{85}Kr reduction is provided by cryogenic distillation, removing krypton from xenon by making use of the different boiling points of the two components in a binary mixture. This technique is the chosen way for the XENON Dark Matter Project, where a first commercial distillation column has achieved a contamination lower than 1 ppt [Lin14] for the XENON100 experiment. Although, this purity is below the desired value of 1 ppt, it was achieved with multiple distillations and even if multiple distillation of the xenon

---

[1] 1 ppt (parts per trillion) $= 10^{-12}$

[2] 1 ppb (parts per billion) $= 10^{-9}$
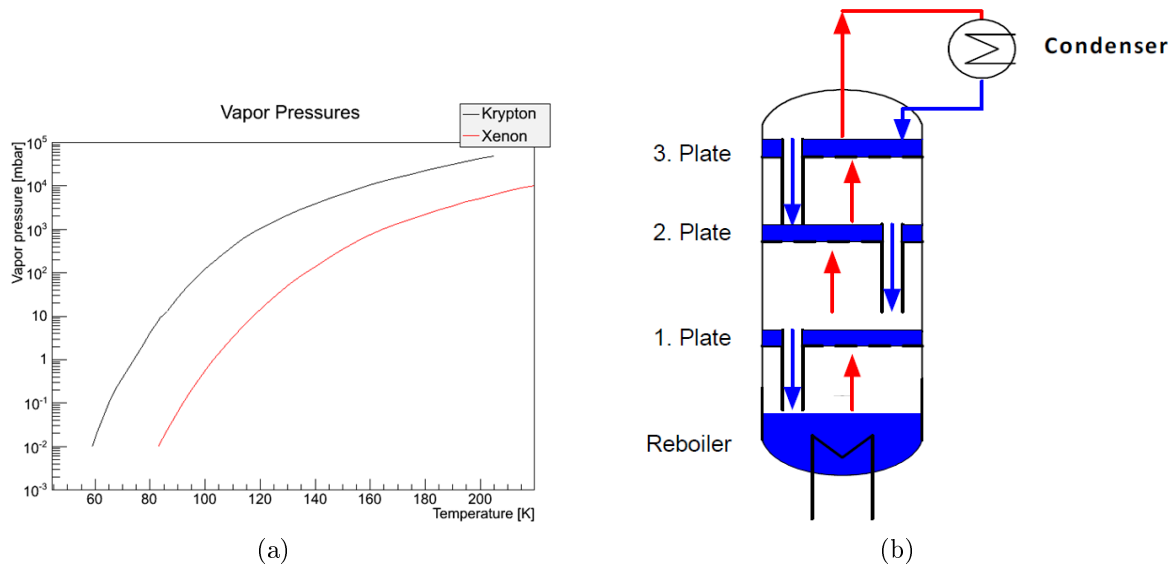
Figure 4.4: (a) Vapor pressures of xenon (red line) and krypton (black line) in dependence
of temperature. Data from [Lid07]. (b) Scheme of the working principle of a rec-
tification column. Shown is the reboiler and the condenser as main parts and dif-
ferent distillation stages (plates) in between. Figure in courtesy of C.Huhmann.

inventory would lead to any desired purity, the throughput of only 0.6 kg/h would not match
the time schedule for a multi-ton experiment as XENON1T. As a consequence of this, a new
column has been designed and is prepared for the XENON1T experiment at the Institut für
Kernpyhsik, University of Münster.

4.2.1 Working principle

The distillation principle itself depends more precisely on the difference in vapor pressures
(detailed description of the vapor pressure concept follows in chapter 5.2.3) of the binary
mixture. As shown in figure 4.4, krypton is compared to xenon the more volatile component,
which leads to a possible enrichment of krypton in the gaseous phase, while the remaining
liquid phase is depleted in terms of krypton, if there is a dual phase binary mixture. In the
technical process this is called one theoretical distillation stage.
This process is operated several times consecutively, leading to a liquefaction of the gaseous
phase in the following stage, thus building a new gaseous phase, where separation is repeated.
A scheme of the working principle of such a multi-stage distillation column is shown in
figure 4.4. One of the core elements of the distillation column is a reboiler at the bottom,
where the liquid mixture is partly evaporated. This evaporated gas is re-liquefied at the
top condenser, producing a partial re-flux which is guided through different stages. All of
them are a distillation step itself, causing their number to be depended on the requested
purity. Enhancement of this process is realized by using a special package material along
the distillation column, increasing the transition phase surface drastically.
Only a small amount of gas, compared to the total content, is released at the top, the so

called off-gas, which is krypton enriched, while the concentration of krypton is the lowest at the liquid reservoir inside the reboiler. This liquid will be used for filling the detector. A key parameter of the column is the separation factor, which describes the ratio between the krypton concentration at the inlet and at the liquid outlet. The number of stages necessary for a certain separation factor and accordingly, the height of such a column can classically be calculated by the McCabe-Thiele method. However, if this principle is feasible for low concentrations in the sub-ppb regime is questionable, because of the lack of krypton molecules to create a classical liquid phase. A detailed description of the working principle and a description of a test column can be found in [Mur14].

4.2.2 The distillation column of the XENON1T experiment

An example of a multi-stage distillation column, operated in partial reflux mode, is the distillation column prepared at the University of Münster for the XENON1T experiment (see figure 4.5). This column, with a total height of 5 m, has 3 m of package material and is built to operate with a feed through of 3 kg/h, while losing only 1 % gas at the off-gas line. A striking feature of the distillation column are 6 analysis ports, where gas can be extracted for analysis purposes to measure a krypton concentration gradient along the column. Tests of a version with only 1 m package material showed a concentration at the liquid output of less than 26 ppq at[3] 90 % CL. measured with a rare gas mass spectrometer (RGMS) supported by a gas-chromatograph (GC) at the Max-Planck Institut in Heidelberg (see 4.3.2 and [Sto14]), which surpasses the goal of the XENON1T experiment by almost two orders of magnitude. Furthermore, the measurement revealed a separation factor greater than 4500. These numbers are only upper and lower limits with a confidence level of 90 %, since the measurement of the liquid out concentration was at the sensitivity edge of the GC-RGMS-system. Detailed information can be found in the upcoming PhD thesis of S. Rosendahl [Ros14a].

4.3 Detection methods

The detection of ^{85}Kr is a challenging task since it is abundant only at traces in dark matter experiments as described in this chapter. Because of that, it is usually easier to refer to the total krypton concentration and assume a fixed ratio between the isotope ^{85}Kr and the natural isotopes. Still, the measurement of concentrations below the ppm-level[4] is also not trivial and often require methods, which are extensively time or gas consuming. This section will show examples of methods applied to determine the krypton concentration in the XENON100 and XENON1T experiments, referred as offline methods, since they do not provide a result directly at the gas sample taking or live at detector operation, whereas the chapter 5 presents an investigation of a specific method for an online analysis.

---

[3] 1 ppq (parts per quadrillion) $= 10^{-15}$
[4] 1 ppt (parts per million) $= 10^{-6}$

Figure 4.5: *Picture of the 5 m distillation column being prepared for the XENON1T experiment. The insulation vacuum vessel is lowered, providing a clear view on the reboiler.*

4.3.1 Direct measurement with the detector

Two possible methods can be used in order to analyze data provided by the TPC itself to classify the krypton concentration. These are directly related to the ^{85}Kr-isotope.

Delayed coincidence method

As shown in figure 4.3 the decay of ^{85}Kr into ^{85}Rb is possible over two ways. While the main fraction decays directly, there is also a two-step process with a branching ratio of 0.43 %, where firstly a β-decay into an excited state of ^{85}Rb takes place, which then relaxes into the next state by a γ-emission. This delayed release of a β-particle with 173.4 keV and a gamma with 514 keV can be searched for in the waveforms, recorded by the PMTs inside the detector. Then by simply counting this events and taking the detection efficiency into account, it is possible to put a number on the ^{85}Kr concentration. One disadvantage of this method is being given by the fact that a similar decay from the primordial decay chain of ^{232}Th[5] disintegrates with comparable conditions. Furthermore, the exposure time to collect sufficient statistics, which are heavily decreased, due to the small branching ratio, scales with the concentration and is in the scale of a few months for concentrations around 20 ppt [Lin13]. Therefore a statement is only possible after the scientific dark matter run and in the worst case only as an upper limit, if the sensitivity is limited by the statistics and external factors. Additionally, if the krypton concentration changes during the time, e.g. due to air leaks, it becomes difficult to distinguish this in time.

Spectral shape analysis of the electromagnetic background

Another option is a careful shape analysis of the low electromagnetic background, where all known background sources and detector energy resolution are used to fit the background. The advantage of this method lies in the fact that almost every decay of ^{85}Kr counts, but becomes insensitive, if krypton is not one of the main background sources anymore [Lin13].

4.3.2 External setups

Two external setups are developed and used for the XENON project. Both have in common that a sample taking and transport to the respective facilities is necessary, which is time consuming, additional to the already needed time for the measurement itself.

---

[5]The decay of ^{212}Bi into ^{212}Po can also occur as a two step process, and overlaps partly with the time and energy window of the ^{85}Kr decay.
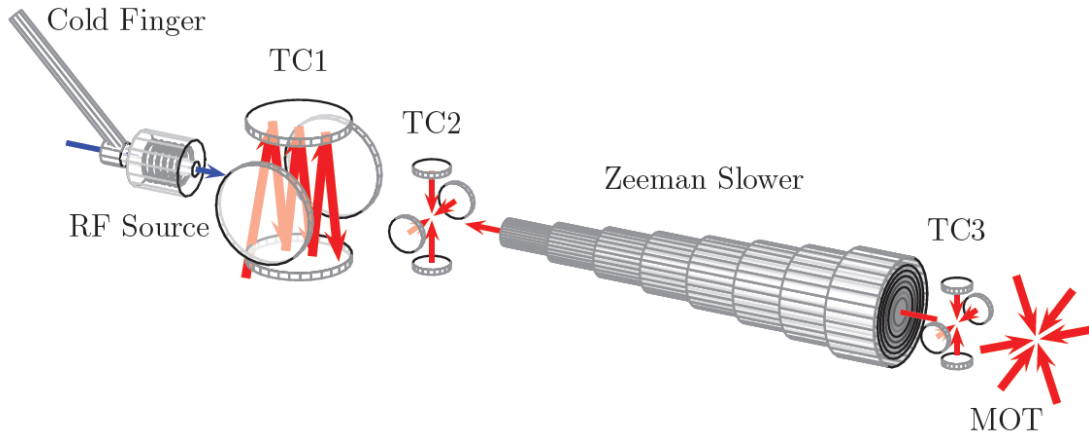
Figure 4.6: *ATTA system schematic. Selected components and laser beam directions (red arrows) are shown. Metastable atoms are generated and cooled by a RF source with an attached cold finger, collimated by three transverse cooling stages (TC1-TC3), decelerated with the Zeeman slowing technique, and captured in the magneto-optical trap (MOT) for detection. Figure and caption taken from [Apr13].*

Atom trap trace analysis (ATTA)

The atom trap trace analysis (ATTA) is a detection system, using laser cooling to trap target atoms (^{84}Kr in this case) and counting single atoms, thus extracting a total concentration in the gas probe.

The working principle is shown in figure 4.6. A gas sample is injected in a high-vacuum chamber with constant input pressure, creating a continual atom flow. These atoms are excited to a metastable state by a radio frequency plasma discharge. Afterwards this atom beam is collimated and slowed down (by Zeeman tuning) for periodical capture in a magneto-optic trap, which is all established by a semi-conductor based laser system. Detection is done by a measurement of the fluorescence light of the trapped atoms with an avalanche photo diode (APD). For known systematics, generated by calibration measurements, and known input flow, the atoms per unit time can be calculated and therefore also the concentration in the sample.

This technique is in development, and since it has shown proof of principle below the ppm-regime [Apr13], the actual sensitivity is under research. While the effective measurement time depends on the concentration itself (expected signal of 0.7 atoms per hour) and is in the order of hours, the transport of a sample to the setup itself takes order of days at the moment, due to its location at the Columbia University, which limits the possibility of live analysis. Detailed description can be found in [Apr13].
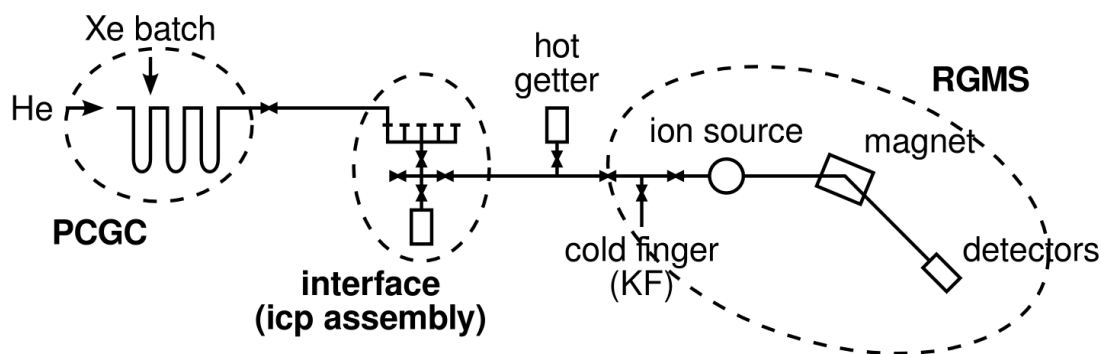
Figure 4.7: *Scheme of the setup for a gas chromatography supported rare gas mass spectrometer. The main devices for the measurement are the gas chromatograph to separate krypton from xenon and the sector field mass spectrometer working as a detector. A calibration device is installed in between these two components for reliably testing the system with pipettes with known concentrations of krypton. Figure from [Lin13].*

GC-RGMS

A natural approach for krypton in xenon measurements is the use of a mass spectrometer. However, the sensitivity of commercial mass spectrometers is far below the necessary limit (more details in the following chapter 5). For this reason different techniques of reproducible separation of krypton from the xenon gas sample are tested. One successful technique is the gas chromatograhpy (GC), where a gas sample is mixed with ultra-pure helium, acting as a carrier gas (*mobile phase*), and then forced through different stages of columns filled with special adsorbents (*stationary phase*). Differences in the interaction strength between the gas components and the adsorbent and consequently, in the retention time, which is depending on the characteristic moving velocity of each component, lead to clear separation. Since the whole system is cryo-cooled, the temperature can be adjusted to optimize for different vapor pressures of different components. For krypton in xenon this system has been successfully tested with a succeeding sector field mass spectrometer (MS) as seen in figure 4.7. The gas batch from the GC is collected at a cold finger at the ion source of the MS. A warm up distributes the gas inside the setup, and then gets ionized by electrons, focused and accelerated by electric fields towards a magnetic dipole field, separating the ions. Detection is achieved by a secondary electron multiplier or a Faraday cup.
With this setup a sensitivity limit of 8 ppq has been claimed [Lin14] and has been applied, e.g. to the measurement samples from the Münster column (see previous section). A detailed description of the method and its measurement can be found in [Lin13], [Lin14] and [Sto14].

An experimental method for online krypton detection

Several methods for the detection of krypton in xenon have been introduced in the previous chapter. All of them have in common that the results for the krypton concentration are not available directly at sample taking due to various reasons (thus they are called offline methods). Therefore, based on the technique of Dobi et al. [Dob11], a dedicated online system has been developed, focusing on fast results, while reducing the required amount of xenon to an absolute minimum. For this reason, different aspects have been tested on an existing setup (RGA-I) presented in [Bro13] and have been implemented into a new mobile system (RGA-II), which is designed to measure directly at the XENON1T experiment. This chapter will provide a general overview of the idea behind the method and detailed information about the detection technique itself, the realization at the two different setups and their characterization.

The experimental setup and the obtained result have been produced in collaboration with Michael Murra and Stephan Rosendahl, who will use a part of these results in his dissertation [Ros14a].

5.1 Overview of the measurement method

The centerpiece of this method is a mass spectrometer (in this setup used as a residual gas analyzer (RGA)), separating and detecting incoming particles by their mass-over-charge ratio (see section 5.2.2). However, without additional supporting techniques, the sensitivity of commercial available mass spectrometers is not sufficient, since the concentrations of interest

are below the ppm-level.

In figure 5.1 a basic scheme of the auxiliary structure is shown, which is used to overcome the sensitivity limit of a commercial mass spectrometer. A fraction of a standard liter of xenon gas, with unknown krypton concentrations, is introduced into a cold trap (see section 5.2.3), where a part of the gas routing pipe is cooled down to $77\,\mathrm{K}$ by submerging it into liquid nitrogen. This provides an artificial enhancement of the krypton concentration, as most of the xenon is frozen at this part, while the krypton passes almost unattached, due to its higher vapor pressure and low partial pressure (detailed description in 5.2.3). Additionally, to prohibit saturation at the RGA by the bulk of xenon, pressure reducing elements in form of differential pumping sections (DPS) (see section 5.2.4), are placed in front and behind of the cold trap. Moreover, the mass spectrometer is only used in the mass region of interest, which is selected to register krypton but prevent any xenon detection.

Furthermore, a special custom-made butterfly valve (BFV), is mounted before the turbo molecular pump (TMP), which allows to control the gas load inside the measurement chamber via control over the pumping speed. This increases the dynamic range and provides a higher sensitivity (described in section 5.2.5).
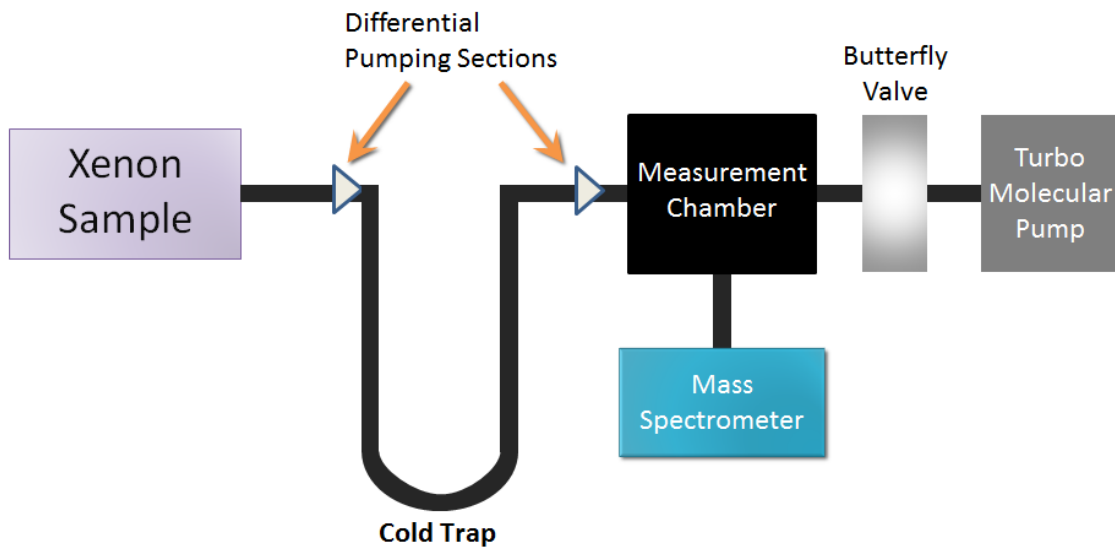
Figure 5.1: *Scheme of the detection setup. A mass spectrometer, used as a residual gas analyzer (RGA), supported by a cold trap (CT) for enhanced krypton concentration. Furthermore, two differential pumping sections (DPS) are included for reliable measurements and additionally, a butterfly valve (BFV) in front of the turbo molecular pump is necessary for measurements with increased sensitivity compared to a stand-alone mass spectrometer.*

5.2 Detailed description of the mobile measurement setup (RGA-II)
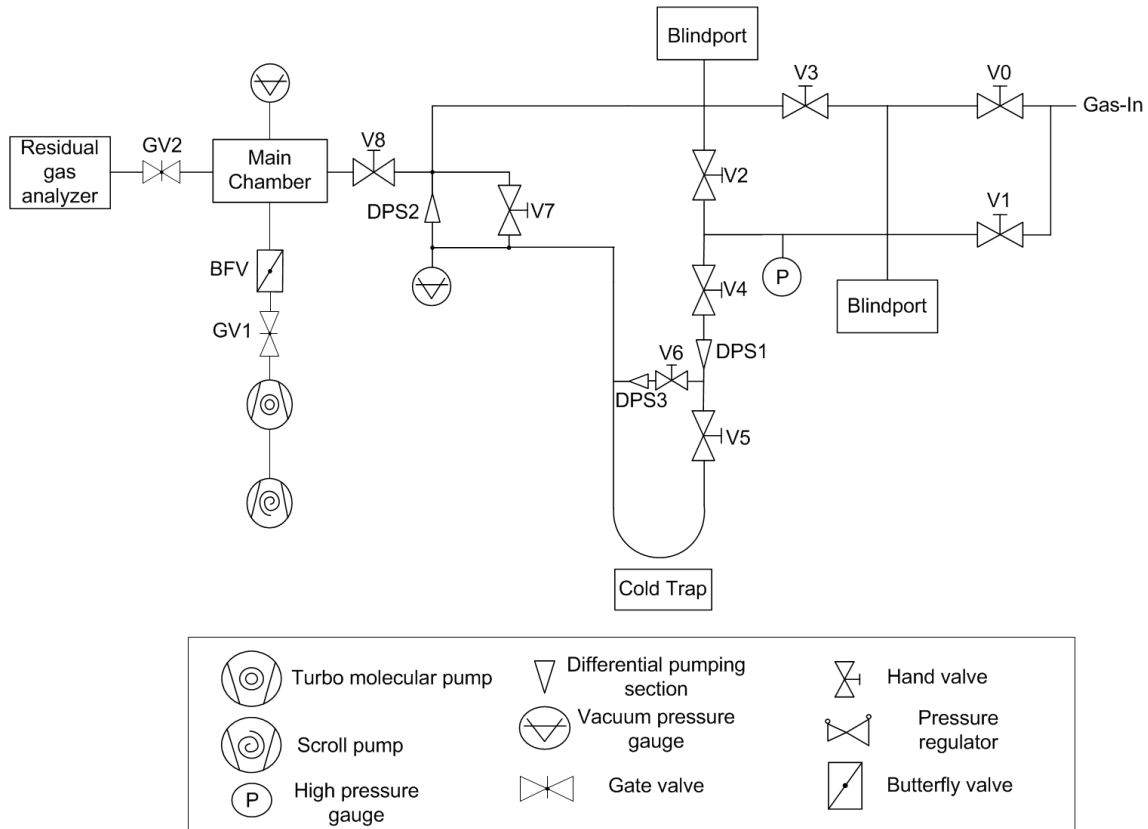
Figure 5.2: *Complete flow chart for the mobile online detection setup, referred as RGA-II setup. This version, containing a pressure regulator, is dedicated for systems providing an overpressure, as for example direct measurements at gas bottles for the XENON1T experiment. The DPS3, at the bypass of the cold trap, is not implemented yet, but is planned to be used for analysis of other impurities.*

One of the main tasks of this thesis was to improve the existing setup at the University of Muenster, described in [Sch12] and [Bro13], and implement its features into a mobile device, which is able to measure directly at the XENON1T facility at the LNGS. In figure 5.2 the underlying flow chart is shown as it was designed within this thesis. The completed setup attached to the distillation column for the XENON1T experiment at the University of Muenster is presented in figure 5.3.

The specific elements will be described and characterized for the RGA-II setup in this section, while the follow-up section will introduce an overview of the stationary setup (RGA-I) and outline the differences compared to the RGA-II setup.
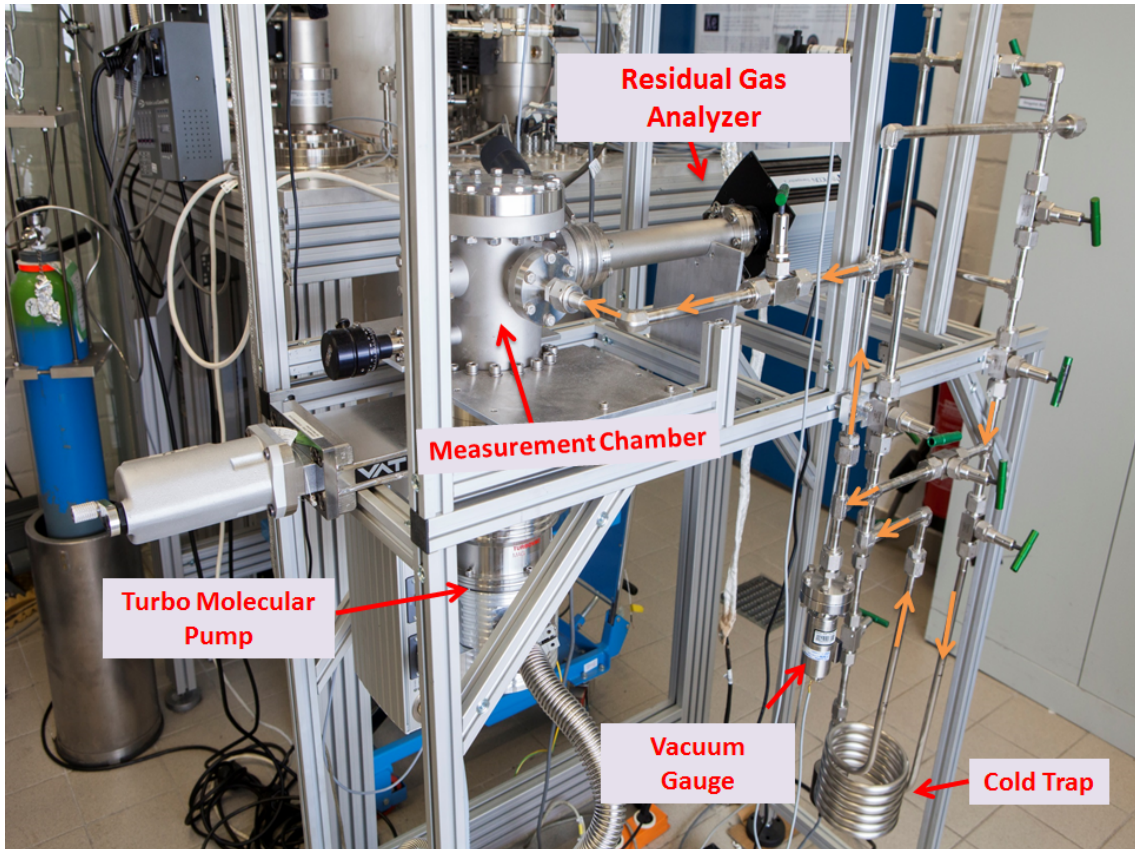
Figure 5.3: *Picture of the RGA-II setup attached to the distillation column at the University of Muenster. Marked are the quadrupole mass filter with the subsequent electronics attached to the measurement chamber and the bent stainless steel coil used as a cold trap, with its vacuum gauge, measuring the pressure at this point. The gas routing, important for a krypton detection measurement, is indicated by the orange arrows.*

5.2.1 Ultra-high vacuum conditions at the setup

A system achieving a sub-ppm sensitivity needs ultra-high vacuum (UHV) conditions for the operation to avoid impurities of the setup contaminating the analyzed gas sample. Furthermore, the used quadrupole mass spectrometer requires a pressure level below 1×10^{-5} mbar for its full functionality.

In the RGA-II setup a turbo molecular pump with magnetic bearing (type: *Oerlikon Leybold TurboVac Mag W300iP*) combined with an oil-free backing pump (type: *Oerlikon Leybold Scrollvac SC5D*) achieves pressures below 1.33×10^{-8} mbar at the RGA measured by a vacuum transducer (type: *mks 972B Dual Mag*). While these oil-free pumps are used, in order to avoid contamination by hydrocarbons, the removal of water and other impurities was achieved by baking out the system at temperatures of $220\,°C$ after every venting. Additionally it has been leak checked with a combined leak check system (type: *Oerlikon Leybold PhoeniXL 300*) down to leak rates lower then $1 \times 10^{-10} \frac{mbar \cdot l}{s}$.

A UHV gate valve (type: *VAT UHV mini gate valve 1032*) is placed in between the mass
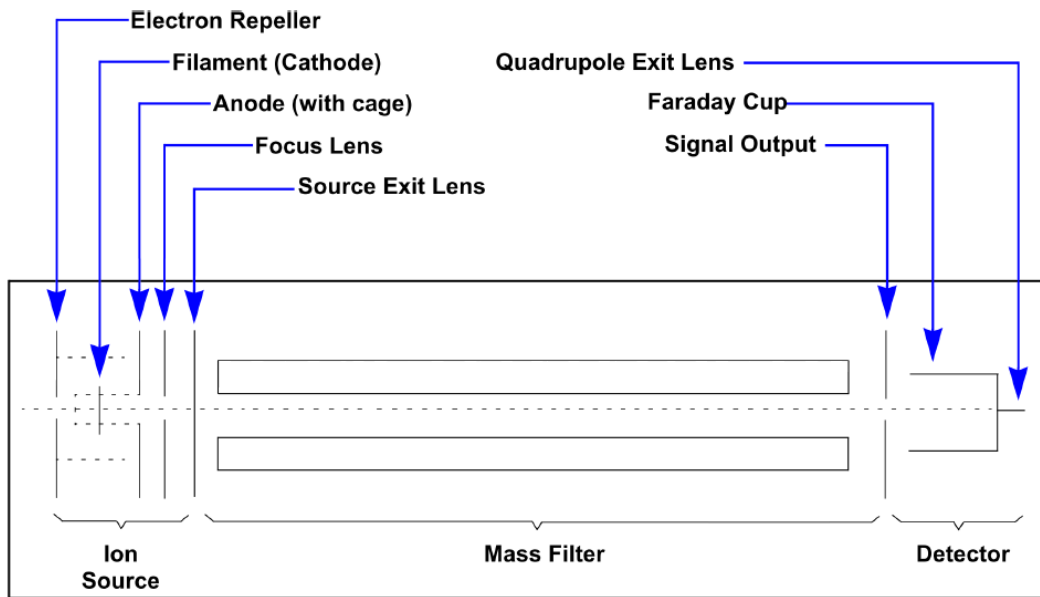
Figure 5.4: *Principle scheme of the used residual gas analyzer with its main elements (ion source, analyzing section and detector). Drawing taken from [Inf04].*

filter and the measurement chamber to avoid contamination of the mass filter, as it can be closed if the system is e.g. exposed to air. Furthermore, because of maintenance reasons a second gate valve (type: *VAT UHV gate valve 10840*) is placed in front of the turbo molecular pump.

5.2.2 Residual gas analyzer (RGA)

As already mentioned, the krypton detection is done by a mass spectrometer acting as a RGA. In this particular setup a quadrupole mass filter is used, which is advantageous because of its linearity over a wide range and its robustness in the practical use. Figure 5.4 shows the major components of the implemented *Inficon Transpector2 H200M* quadrupole mass filter as used for the RGA-II setup, which can be divided into three main parts providing the impurity detection:

1. **Ion source**

Neutral atoms of interest have to be ionized for detection with a quadrupole mass filter, which is realized by electron ionization. Therefore, an electron beam produced by heating a filament, made of an iridium wire mixed with thorium-oxide, is focused into an ion cage, which is mounted to an anode. As it is filled with the residual gas, the electrons ionize the neutral gas molecules, producing mainly single ionized particles. However, with less abundance, also multiply ionized atoms are generated this way, based on the energy of the incoming electrons, as well as on the gas species itself. This provides a possible discrimination of different components with same masses, due to the changing ionization probability for each element. The pressure of the residual gas is not allowed to overcome a threshold of

6.6×10^{-4} mbar for the *Transpector2*, as this would decrease the mean free path of the ions below a critical level.

Since the *Transpector2* detects positive ions, the focus lens, which forms an focused ion beam towards the mass filter, is on negative potential compared to the ion cage, as well as the source exit lens. By measuring the total current produced by the ions at this point, the RGA is able to measure the total pressure with an error of 30 %, providing a cross check of the additional vacuum gauge [Inf99].

2. Mass filter

A quadrupole mass filter works as the analyzing section of the RGA filtering ions by their mass-over-charge ratio[1] $\left(\frac{m}{z}\right)$. This device has four alternately charged cylindrically shaped rods[2], which are all connected to a potential Φ, consisting of a radio frequency voltage V with a frequency ω and a superimposed DC-voltage U, as shown in figure 5.5:

$$\Phi = U + V cos(\omega t). \tag{5.1}$$

Incoming ions perform harmonic oscillations in this potential, with an amplitude depending on their mass-over-charge ratio $\frac{m}{z}$, the applied frequency ω and the ratio of the set amplitudes $\frac{U}{V}$. The trajectories of these ions, in dependence of this parameters, can be calculated by the Mathieu differential equations, which are described in detail in [Gro11]. Solving this equations, it leads to the main conclusion, that for certain values stable trajectories exist, where the amplitude of the ion oscillation is less then the distance between the rods at all times. As a result of this, when choosing ω and $\frac{U}{V}$ properly, transmission of ions with the desired mass-over-charge ratio is established. This can be varied by changing the absolute values of the amplitudes U and V, while maintaining their ratio. If an ion does not match the correct mass-over-charge ratio, it will have an increasing amplitude, leading to decharging collisions with the rods, as soon as the amplitude of the oscillation exceeds the distance between them.

An important note is, that the choice of parameters is always a trade-off between mass resolution and sensitivity [Wut06] but is automated in the software provided by the company and hence not supposed to be changed for the *Transpector2*.

3. Detector

As the selection of the ions with correct mass-over-charge ratio is provided by the analyzing section, the detection part of the RGA is only a counter for the incoming ions. Therefore, the ion beam leaving the mass filter is focused towards a Faraday cup (FC), which is a metal cup on ground potential, connected to a measurement device registering the current produced by the ions, which can be read out directly as a signal based on the incoming ion amount. Additionally, the *Transpector2* has an electron-multiplier (EM), which can be activated as an amplifier of the incoming current into the Faraday cup. While the FC is directly measuring the charge, the EM increases the signal proportionally for every electron created by

---

[1]The mass-over-charge ratio $\frac{m}{z}$ is dimensionless, as the mass is defined here equal to the mass number A known from nuclear physics as well as the charge z, which is equal to the atomic number Z.

[2]Theoretically, an optimized quadrupole mass filter should consist of hyperbolic shaped rods, but for practical reasons the cylindrical shapes are used, which produce an electric field close enough to the theoretical description of the hyperbolic ones, if the radius is chosen properly to the length [Wut06].
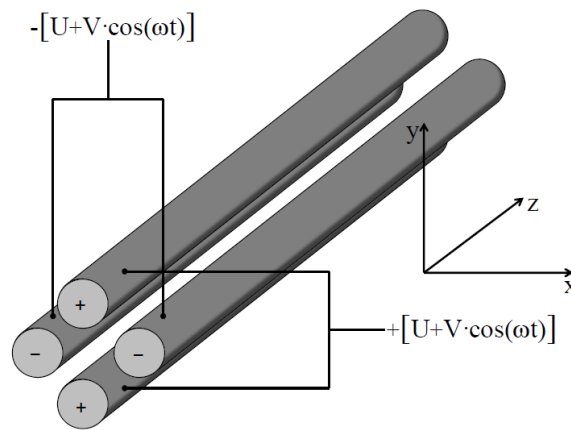
Figure 5.5: *Cross section of four cylindrical rods with marked potentials on each rod. As shown, opposite rods lie on equal potential. Only ions with the chosen mass-over-charge ratio will surpass the rods unaffected depending on the chosen values of U, V and ω. Figure taken from [Ket12]*

incoming ions. This amplifies the signal, and thus the sensitivity, from 7.6×10^{-5} A/mbar to 380 A/mbar according to the company [Inf09] but limits the measurable concentration, since an integrated signal exceeding 5×10^{-7} A is noted as potentially dangerous for the EM.

5.2.3 Cold trap

As the RGA is not capable of detecting gas traces in xenon below the ppm-level by itself, an enhancement of the concentration is a common approach in order to increase the sensitivity. A possible method to enhance the krypton concentration is the removal of the xenon, while keeping the krypton amount constant. This can be achieved by using the freezing behavior of these two components at low temperatures, which vary due to the difference in vapor pressures (see figure 5.6).

Vapor pressure

If a two-phase system, liquid-gas or solid-gas, is in thermal equilibrium, a gaseous phase, called vapor, is existing above the liquid/solid. The pressure P of this vapor is dependent on the temperature T in a non-linear way, described by the Antoine equation derived from the Clausius-Clapyeron-relation:

$$\log_{10} P = A - \frac{B}{C + T}. \tag{5.2}$$

All three parameters A, B and C are gas component-specific constants. As a result of this, the vapor pressure is characteristic for a specific component and differs for each substance. A derivation of this equation can be used to calculate boiling points, which are reached if the vapor pressure matches the ambient pressure.

As shown in figure 5.6, krypton has always a higher vapor pressure than xenon, thus called the more volatile component. At the temperature of liquid nitrogen (77 K) the vapor pressure of krypton (derived from [Lid07]) is around

$$P_{Kr} \approx 2\,mbar,$$

while xenon has a vapor pressure of ([Leo10])

$$P_{Xe} \approx 2.4 \times 10^{-3}\,mbar,$$

which is a difference of three orders of magnitude. Theoretically, this means that up to a pressure of $2\,mbar$ for krypton, respectively $2.4 \times 10^{-3}\,mbar$ for xenon, no transition into the liquid or solid phase takes place at this temperature.

Technically, this can be used for an enhancement of the krypton concentration, since the partial pressure of krypton, even for high concentrations at the ppm-level, does not exceed a partial pressure of $2\,mbar$, which means it should not freeze-out at the cold trap at $77\,K$. On the contrary, xenon freezes at the cold trap down to its vapor pressure forming xenon ice. This effectively reduces the content of xenon in the gaseous phase, while the krypton amount stays constant, thus increasing the krypton concentration depending on the gas amount used for a measurement.
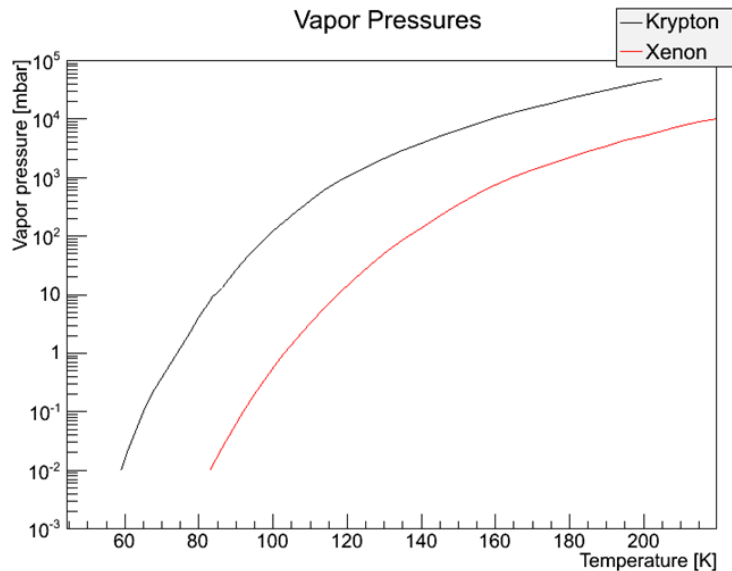

Figure 5.6: *Vapor pressure of krypton (black) and xenon (red) in dependence of the temperature [Lid07]. The region of interest at 77 K shows a pressure of about 2 mbar for krypton, while the extrapolation of xenon is around 10^{-3} mbar, thus separating them by 3 orders of magnitude.*

Technical realization

In figure 5.7 the technical realization of the cold trap concept is shown. A stainless steel (316L) tube with an inner diameter of 10.21 mm and a length of about 4 m has been bent into a coil for practical use, thus allowing for submerging it into a Dewar vessel filled with liquid nitrogen. During all measurements no influence of the immersion depth has been seen, as long as the gross of the coil is covered with liquid nitrogen. Investigation with ultra-pure xenon, provided by the cryogenic distillation column of the University of Muenster, has shown reproducible pressures inside the cold trap of

$$p_{ct} \sim 3.3 \times 10^{-3}\,\mathrm{mbar},$$

measured by an active gas-independent diaphragm capacitance gauge (type: *Oerlikon Leybold Ceravac CTR100*) with an 1 % error at read-out, being in good agreement with the value measured by [Leo10]. For the final setup, measurements with the RGA-II using a different sensor (type: *mks 972B DualMag transducer*) have been performed. This sensor, which operates either as a Pirani gauge or quantifies the pressure based on the cold-cathode ionization, showed a pressure value of $3.4 \times 10^{-3}\,\mathrm{mbar}$ at the cold trap including a correction factor of 2.87 [MKS14] to the read-out of $1.2 \times 10^{-3}\,\mathrm{mbar}$. As the sensor is working at this pressure on its transition region, the read-out error varies between 10 % and 30 % [MKS12], depending which mode is used, which means the pressure is consistent with the value obtained beforehand in any case.

Independent of the introduced amount of xenon, this pressure is constantly achieved, leading to the strong assumption that the cold trap works as expected and is able to reproducibly freeze-out the introduced xenon down to its vapor pressure. This is also an independent measurement of the vapor pressure of xenon at 77 K, where almost no data exists.

5.2.4 Differential pumping sections

Having the cold trap principle in mind, two important constraints at the inlet and the outlet have to be considered. On the one hand, to guarantee the complete freeze-out of xenon up to its vapor pressure it is necessary to limit the in-going flow of the cold trap. Additionally, if the xenon is contaminated with impurities, which are not freezing out in the cold trap (e.g. other noble gases like argon, helium or krypton), the pressure inside the measurement chamber will exceed the vapor pressure of xenon, which makes a reduction of the input flow essential to prohibit damages at the RGA.

On the other hand, as the provided pressure at the cold trap is at least the pure xenon vapor pressure of $\sim 10^{-3}\,\mathrm{mbar}$, the maximum operating pressure of the RGA of $6.6 \times 10^{-4}\,\mathrm{mbar}$ would always be exceeded, which makes a measurement impossible, and hence, the gas flow from the cold trap to the measurement chamber has to be reduced as well.

These issues are resolved with two differential pumping sections (DPS), where one is placed at the entrance (DPS1) and one at the outlet of the cold trap (DPS2). Figure 5.8 shows both DPS, which are simply low conductance elements with a slightly different design adapted to the specific needs of their positioning inside the system (see figure 5.7). While the inlet
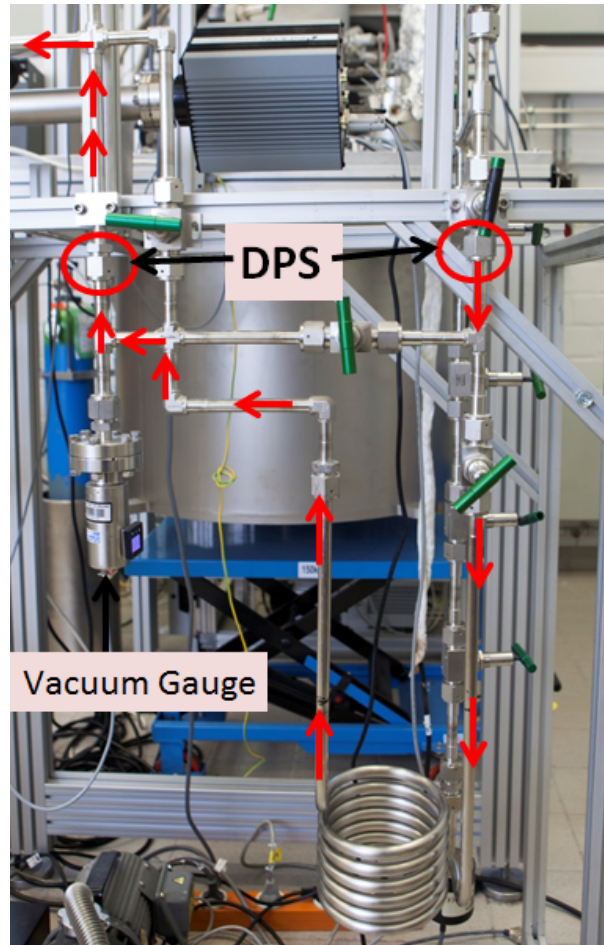
Figure 5.7: *Front view of the bent stainless steel coil referred to as cold trap. Additionally marked are the two differential pumping sections and the gas routing (red arrows) for a krypton measurement. The Dewar vessel used to submerge the coil into liquid nitrogen is not shown.*

DPS1 needs to provide a pressure reduction from 1 bar down to a pressure slightly above the vapor pressure of xenon, the DPS2 at the outlet of the cold trap needs to reduce the pressure from the vapor pressure further down to a pressure level suitable for operating the RGA safely.

Because of that, DPS1 is a capillary tube with a length of 20 mm and a diameter of 0.1 mm, which is laser welded into a VCR gasket for simple implementation into any VCR connection. Due to the machining process, which has a large tolerance especially for the diameter of the DPS1, these values may vary and because of that change the characteristics of the DPS1. For the DPS2, only a small hole with a length of 5 mm and a diameter of 1 mm has been drilled into a laser welded junction inside a VCR gasket. The pressure p_{in} of the flow into the DPS1 is monitored by a pressure transducer of the type *Swagelok PTU-S-AC931AD* while the pressure p_{ct} at the DPS2 is measured with a *mks 972B DualMag Transducer*.
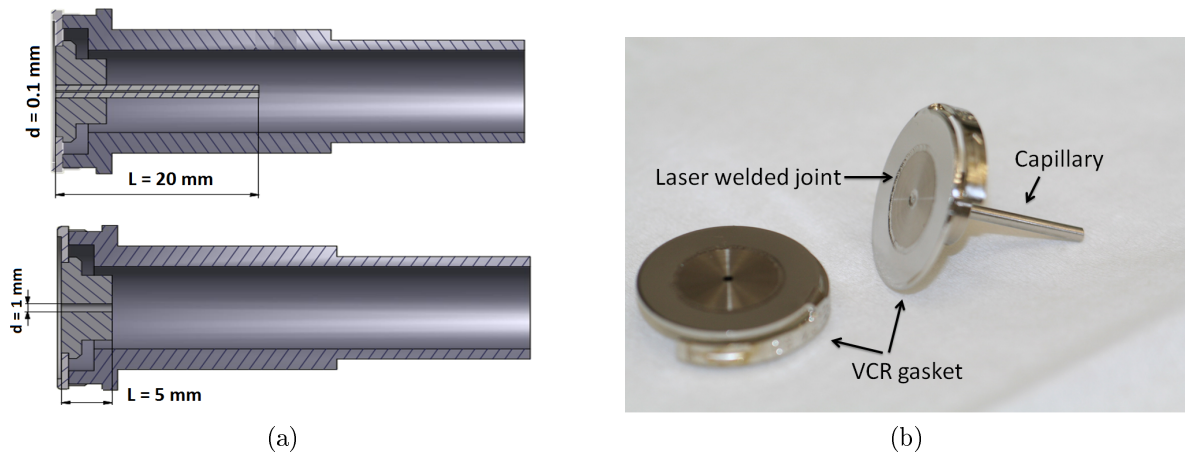
Figure 5.8: *(a) Technical drawing of the two differential pumping sections. While the inlet DPS1 into the cold trap consists of a capillary with a designed length of 20 mm and a diameter of 0.10 mm, the outlet DPS2 is a drilling with a diameter of 1 mm and a length of 5 mm. (b) Pictures of the two built DPS used in the RGA-I setup.*

Characterization of the flow

The comparability of different measurements depends strongly on the knowledge of the flow through the system, since the krypton amount is directly correlated to the total in-flowing gas, while the xenon amount is fixed to its vapor pressure. As a result of this, investigation of the flow through the system is of crucial importance. If not mentioned otherwise all equations are based on [Wut06] and errors are only shown, if necessary for a qualitative description.

Different kinds of flows are characterized by their dominating interaction of the particles. If the molecules are mainly interacting with the walls of the tubing, since their mean free path is larger than the diameter of the tubing, this is called a molecular flow. However, if the dominating interaction is between the particles itself, which is the case for a mean free path small compared to the dimensions of the tubing, it is called a viscous flow. Quantitative analysis lead to the so called Knudsen number Kn, which is defined as the ratio of the free mean path $\bar{\ell}$ and the pipe diameter d:

$$\text{Kn} = \frac{\bar{\ell}}{d} \tag{5.3}$$

A Knudsen number above 0.5 characterizes a molecular flow, while a ratio below 0.01 refers to a viscous flow. If the ratio is in between, it is classified as Knudsen flow, where it is in transition between molecular and viscous flow.

Using the expression of the mean free path through

$$\overline{\ell} = \frac{\pi}{4} \cdot \frac{\overline{c}\eta}{p},$$

(5.4)

with the viscosity η, the mean particle velocity $\overline{c}$ and pressure p of the particle flow, the Knudsen number can also be written as:

$$Kn = \frac{\pi}{4} \cdot \frac{\overline{c}\eta}{pd}$$

(5.5)

For the RGA-II the usual inlet pressures are in the order of $1\,\text{bar}$ and with the designed diameter of the DPS1 $0.1\,\text{mm}$, a viscosity for xenon at room temperature of $2.3 \times 10^{-5}\,\frac{kg}{m \cdot s}$ and a mean particle velocity of about $217\,\text{m/s}$ at $293\,\text{K}$, a Knudsen number of 4×10^{-4} for the flow into the DPS1 is estimated. However, since the flow inside the DPS1 changes due to the pressure reduction, it is also interesting to characterize the out-going flow. Using now the typical outlet pressure of around $5 \times 10^{-1}\,\text{mbar}$ (measured by the vacuum gauge at the cold trap) a Knudsen number of ~ 80 is obtained. Thus, while starting as a clearly viscous flow, it is transformed into molecular flow at the end of the DPS1.

As a result of this, the Knudsen number for the DPS2 is always above the molecular limit, since the input flow is already of molecular nature.

Additional characterization of a viscous flow is given by calculation or observation of the flow velocity profile. If the viscous flow is mainly moving along with a constant velocity profile, it is called laminar flow, which means it is faster in its center then on the edge, due to friction with the walls. If the flow is dominated by turbulence, it is called a turbulent flow. Depending on its mean flow velocity ν, density ρ, dynamic viscosity η and the diameter d, the so called Reynolds number is defined:

$$Re = \frac{\rho \cdot \nu \cdot d}{\eta}$$

(5.6)

For a circular profile, it has been found empirically, that a Reynolds number above 4000 indicates a turbulent flow, while a Reynolds number below 2300 refers to a laminar flow, with a transition region in between. The mean flow velocity ν can be obtained by the volume flow rate q through the system as described in the following relation:

$$\nu = \frac{1}{A} \cdot \frac{dV}{dt} = \frac{4}{\pi d^2} \cdot \frac{q}{p}$$

(5.7)

In contradiction to the mean flow velocity, the volume throughput and hence, the flow rate can be measured or can be derived from the pressure drop dp/dt at a fixed volume V in the following way:

$$q = -V \cdot \frac{dp}{dt}$$

(5.8)

For this purpose the pressure drop, which is recorded as a function of time (see figure 5.9), is fitted with an exponential function[3]:

$$p_{\text{in}}(t) = e^{a \cdot t + a_0} \tag{5.9}$$

Calculating the derivative dp_{in}/dt of the exponential fit, the flow q through the DPS1 for any given time (see figure 5.9) can be determined, if the volume is known (see chapter 6.1.2 for more details on volume determination). Inserting equation 5.7 into equation 5.6 allows for the calculation of the Reynolds number. From the example shown in figure 5.9, which is characteristic and reproducible for the RGA-II setup, an estimation of the Reynolds number range by using the upper value of the flow of $0.9 \frac{mbar \cdot l}{s}$ and the lower value of $0.3 \frac{mbar \cdot l}{s}$, is obtained. Thus, the Reynolds number is varying from ~ 2600 for 1.2 bar inlet pressure and ~ 900 for 0.4 bar inlet pressure, which indicates a turbulent flow changing into a laminar flow during gas introduction.
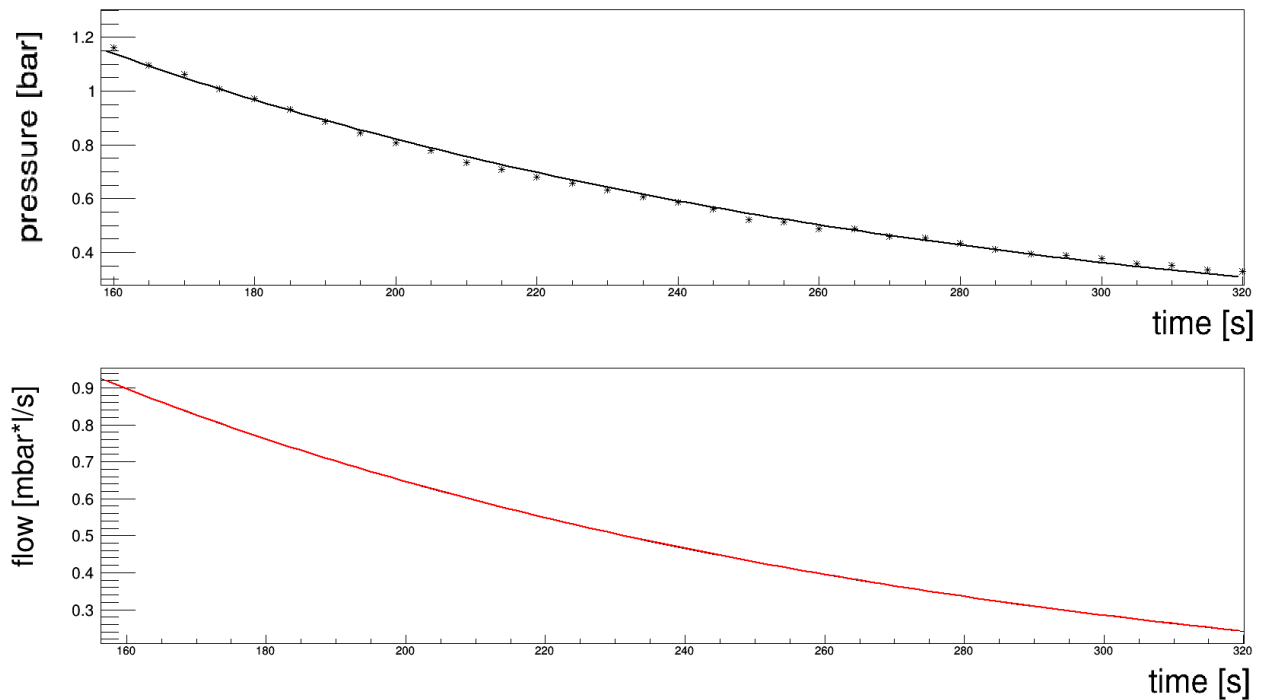
Figure 5.9: *Inlet pressure drop from 1.2 bar down to 0.35 bar versus time (upper plot) fitted with an exponential function (black line). The lower plot shows the calculated flow out of the derivative of the fit combined with a volume factor, representing the used volume for injection into the system.*

---

[3]An exponential fit is not clearly indicated by theory, but was chosen to fit the data for inlet pressures from 1.5 bar and below, as the pressure drop over time has similarity to an exponential drop.

Conductance (DPS1)

The main parameter of DPS is the conductance C, which is generally defined as

$$C = \frac{q}{\Delta p}, \tag{5.10}$$

with the volume flow q and the pressure difference $\Delta p = p_{in} - p_{out}$. Depending on the flow type, the conductance is either changing with the inlet pressure (viscous flow) or is only given by the physical dimensions of the DPS (molecular flow).

As already mentioned, the designed dimensions of the DPS1 can vary from the realized dimensions, which has a huge impact on the conductance C_{DPS1}, considering that the diameter has a strong influence on it independent of the flow type. As a result of this, directly determining the conductance via measurements of the pressure drop and use of equation 5.10 is chosen for a qualitative analysis of the conductance. Taking into account that the calculation of the Knudsen and the Reynolds numbers showed that the flow type changes inside the DPS1, a direct measurement of the conductance becomes more important, since approximations become more complex.

If the inlet pressure p_{in} is much larger than the outlet pressure p_{out}, which is the case for the DPS1 ($1000\,\text{mbar} \gg 5 \times 10^{-1}\,\text{mbar}$), the conductance from equation 5.10 can be written as:

$$C_{DPS1} = -V \cdot \frac{\frac{dp}{dt}}{p_{in}} \tag{5.11}$$

Using the exponential fit method described at equation 5.9, one can see that the conductance becomes a constant factor within a measurement, as the input pressure drop p_{in} and its derivative dp/dt, are only differing by a constant factor:

$$C_{DPS1} = -V \cdot \frac{a \cdot e^{a \cdot t + a_0}}{e^{a \cdot t + a_0}} \tag{5.12}$$

This way the conductance C_{DPS1} has been calculated to be around:

$$C_{DPS1} = 6.7 \times 10^{-4}\,\tfrac{l}{s}$$

It has to be noted that this is based on the approximation by an exponential function, and thus it is only an estimation for the value and behavior of the flow, but as it is recorded with every measurement, this can be considered at analysis.

Conductance (DPS2)

As the flow through the DPS2 is a molecular flow, it allows for the calculation of the conductance C_{DPS2} by the geometric dimensions of the DPS2, which are also more accurate than the DPS1, as this is a drilling with a diameter of $1\,\text{mm}$.

By using the equation

$$C_{\text{DPS2}} = \frac{\pi}{16}\bar{c} \cdot d^2 \cdot \frac{14 + 4\frac{l}{d}}{14 + 18\frac{l}{d} + 3(\frac{l}{d})^3}, \tag{5.13}$$

a theoretical value for the conductance C_{DPS2} can be computed. Inserting the DPS2 dimensions and the properties of the xenon gas used at room temperature, a conductance of

$$C_{\text{DPS2}} = 8.1 \cdot 10^{-3} \frac{l}{s}$$

is calculated, which is higher than C_{DPS1} as expected since it has a much larger diameter. The knowledge of the conductance provides the possibility to calculate the inflow to the measurement chamber q_{in} by transforming equation 5.10 into

$$q_{\text{in}} = C_{\text{DPS2}} \cdot \Delta p. \tag{5.14}$$

Approximating Δp with the pressure p_{ct}, which is allowed since the pressure p_{ct} on the inside is much larger than the pressure p_{mc} at the outlet, leads to a flow into the main chamber of

$$q_{\text{in}} = 2.7 \times 10^{-5} \frac{mbar \cdot l}{s}$$

5.2.5 Butterfly valve

An important instrument for increasing the sensitivity of the setup is the butterfly valve (BFV). As shown in figure 5.10, this valve consists of a metal plate mounted on a fully rotational feed-through. For reproducible positioning of the valve, a scale is added to the feed-through with a manual read-out, which is precise to 0.1°. The advantage of this valve lies in the fact that it provides a direct control of the pumping speed, if added as a variable conductance C_{BFV} in front of the turbo molecular pump, as expressed in this equation [Wut06]:

$$S_{\text{eff}} = \frac{C_{\text{BFV}} \cdot S}{C_{\text{BFV}} + S} \tag{5.15}$$

with the pumping speed S and the effective pumping speed S_{eff}. Due to the change in pumping speed, the gas load inside the measurement chamber is selectable, granting a dynamic range for measurements of different gas compositions, without risking to damage the RGA or losing sensitivity as it would be the case for a fixed system.

Influence on the effective pumping speed

In open mode (90° position) the effect of the BFV on the pumping speed is negligible since the active area towards the turbo molecular pump is small compared to the opening. In closed mode (0° position) the active area is at its maximum, but this does not lead to a complete close-off. For mechanical reasons the metal plate has been machined with a certain tolerance
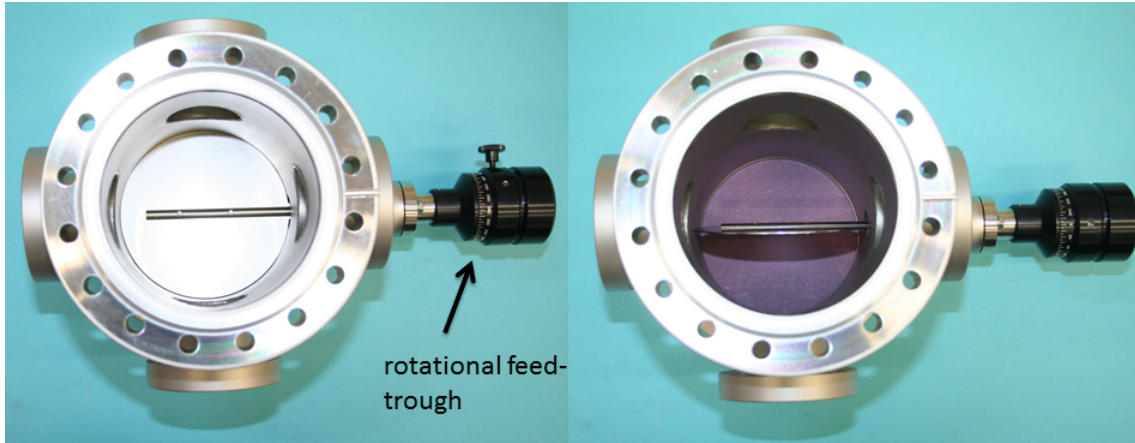
Figure 5.10: *Picture of the butterfly valve in its two extreme positions mounted in the mea-surement chamber of the RGA-II setup. On the left it is fully closed providing the lowest possible conductance and on the right it is fully open for almost no change in pumping speed. Control is granted by a fully rotational feed-through, which can be adjusted with a precision up to 0.1°. The measurement chamber is mounted directly on a turbo molecular pump for a maximum influence on the pumping speed.*

compared to the dimensions inside the main chamber, otherwise it would lose the ability to be fully rotational. Because of that, a small opening along the complete circumference exists, leading to a constant outflow even in fully closed position. The reduced pumping speed S_{eff}, introduced in equation 5.15, can also be calculated (see equation 5.16 [Wut06]), through the gas flow out of the chamber q_{out} and the gas load inside, which is expressed by the pressure p_{mc}.

$$S_{\text{eff}} = \frac{q_{\text{out}}}{p_{\text{mc}}} \tag{5.16}$$

If this pressure inside the measurement chamber is constant, the in-going flow q_{in} is equal to the out-going flow q_{out}. For the used turbo molecular pump the company specifies a maximum pumping speed S of $300\,\text{l/s}$ for nitrogen. Since this is based on the molecular mass, it will be at about $80\,\%$ for xenon [Pfe14]. Table 5.1 shows example measurements with the computed values for the S_{eff} using the in-going xenon flow $q_{in} = 2.7 \times 10^{-5}\,\frac{mbar \cdot l}{s}$, obtained from the DPS2 calculation. The expected result of a non-reduced pumping speed of $\sim 240\,\text{l/s}$ for full opening of the BFV is not proven by this measurements, since it is only around $10\,\%$ of the pumping speed at $90°$. This is most likely due to the fact, that the pressure sensor is connected via a CF40 connection to the measurement chamber, which is an additional conductance.

Table 5.1: Determination of the effective pumping speed S_{eff} for different opening angles α of the butterfly valve

α [°]	p_{MC} [10^{-6}mbar]	S_{eff} [l/s]	S_{eff} [%]
90	0.9	28.7	100
75	1.0	27.0	94.7
20	5.2	5.2	18.3
15	7.0	3.9	13.6
10	18.3	1.5	5.2
5	27.6	1.0	3.5
0	45.8	0.6	2.1

Therefore the pressure reading at the sensor is not equal to the pressure inside the measurement chamber. However, while an understanding of the absolute value is not important, the relative change of pressure, and thus in gas load, by a factor of 50, proves the working principle of the butterfly valve.

5.3 The fixed setup at the University of Muenster (RGA-I)

The fixed RGA-I setup (see figure 5.12), which is described in [Sch12] and [Bro13] was also used for diverse measurements within this thesis. This setup is fixed at the gas system at the University of Muenster and hence, not suitable for applications at the XENON1T experiment. However, due to gas routing specialties it was used for tests of the distillation column at its building phase and also for cross calibrating the RGA-II setup.

As the RGA-I setup was the first test setup, the basic measurement method is the same, but a couple of parts are different:

The size of the cold trap (see 5.12), which has about two times less surface than in the RGA-II setup, the length of the DPS1 capillary (10 mm in RGA-I compared to 20 mm in RGA-II) and the design of the butterfly valve (see figure 5.11) are remarkable differences. Additionally ,the RGA-I is missing any gate vales, which increases the risk of contamination of the system.

Another variation at the RGA-I setup is the pressure reading, which is provided at the measurement chamber by a cold cathode ionization/Pirani gauge-combination (type: *Oerlikon Leybold PTR 90*) with a read-out gas correction factor of 0.4 for xenon gas. The used pressure sensor at the cold trap of the RGA-I (type: *Oerlikon Leybold Ceravac CTR100*) provides a gas-independent check of the vapor pressure.
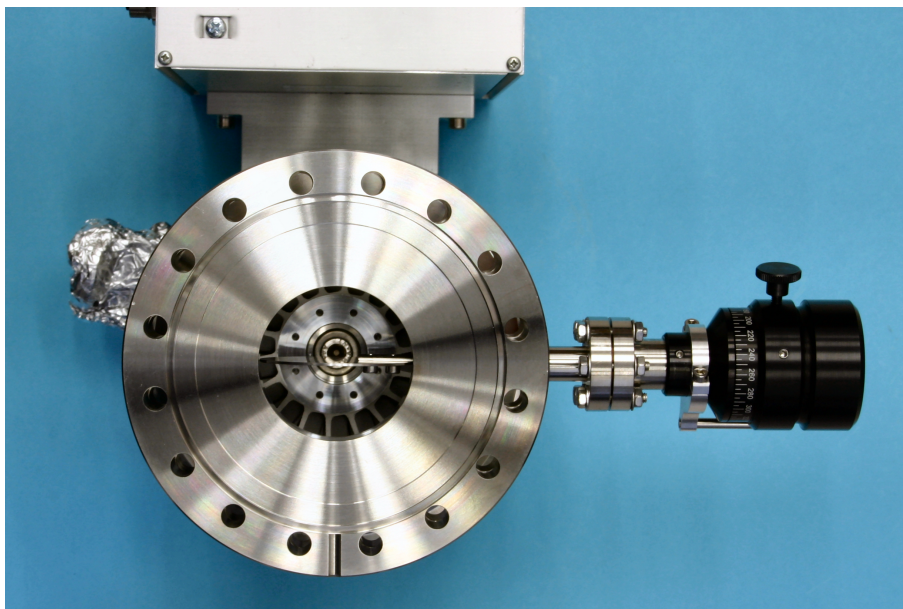
Figure 5.11: *Butterfly valve of the RGA-I setup. A metal plate on a rotational feed-through with an added scale is implemented in a low conductance flange directly mounted at the turbo molecular pump. The main difference to the butterfly valve, used in the RGA-II setup is the reduced pumping speed due to the already low conductance flange at the fully open position.*
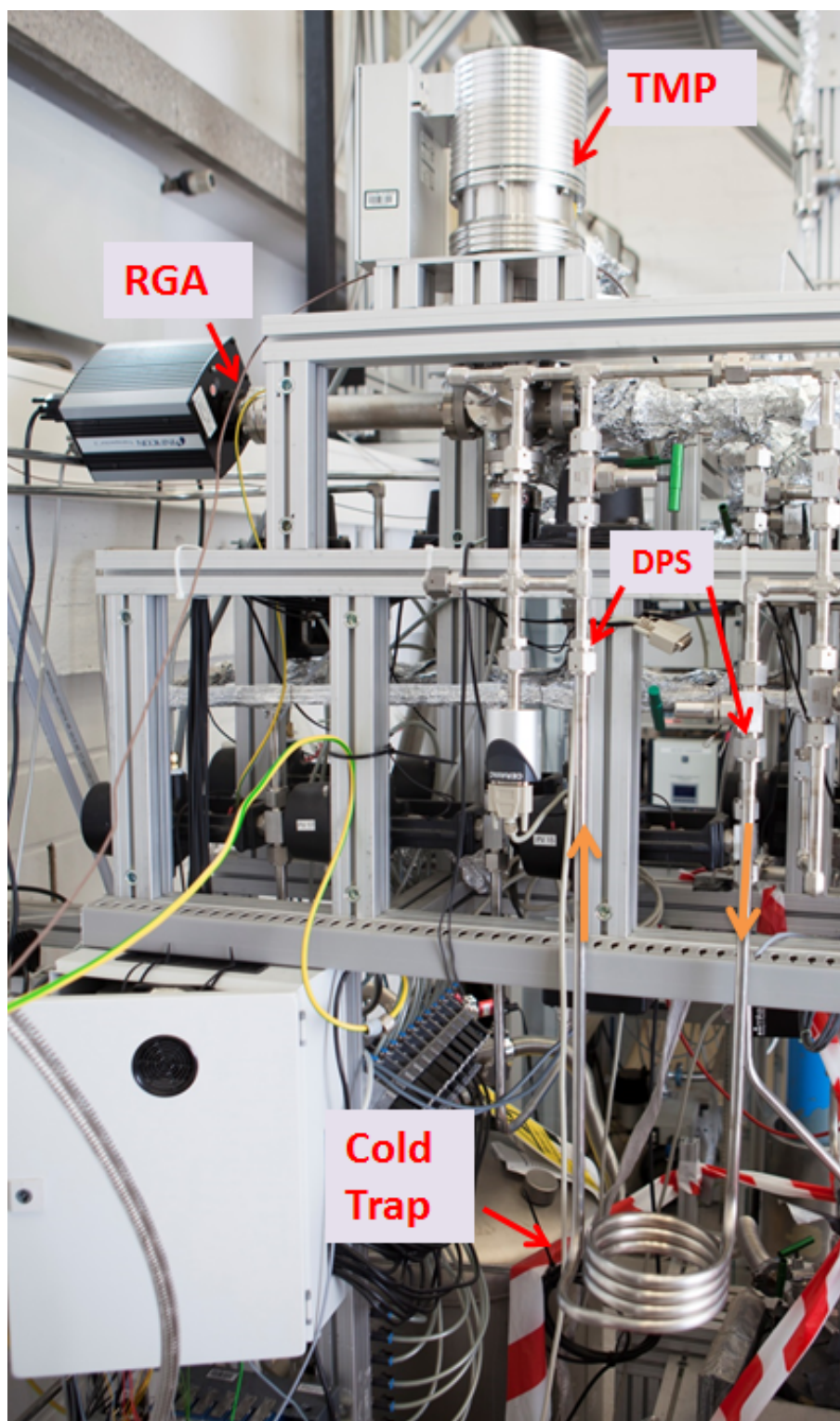
Figure 5.12: *RGA-I setup implemented into the gas-system at the University of Muenster. The direction of the gas flow is indicated (orange arrows). As seen, the cold trap used in this setup has less surface compared to the RGA-II setup by a factor of 2.*

Investigation and Calibration

The main task of the previously described method is the determination of unknown krypton concentrations in xenon gas samples provided by various sources. Thus, an extensive knowledge of the systems reaction towards changing properties of different gas samples is necessary. Therefore, qualitative measurements at different conditions, in terms of gas composition and flow dependence, are in the focus for a basic understanding of the detection method. Furthermore, as the particle behavior inside the cold trap is of crucial importance, but not well described theoretically, reproducible measurements with gas samples of known krypton content have to be studied for a calibration of the system.

In this chapter this investigative evaluation will be presented with possible explanations of different observations made within those measurements. Additionally, one of the main aspects of this thesis, the calibration of both systems (RGA-I and RGA-II) is presented in its technical realization, as well as the required steps in analysis for the obtained results, which are shown in the end of this chapter.

6.1 Gas flow behavior and purity analysis

Since the mass spectrometer itself provides a reproducible response for an equal krypton amount, the signal strength is only depending on the number of krypton particles introduced to the system. This number is given by the initial intrinsic concentration of the gas sample and the fraction of krypton reaching the measurement chamber, which is influenced by the flow behavior inside the system.
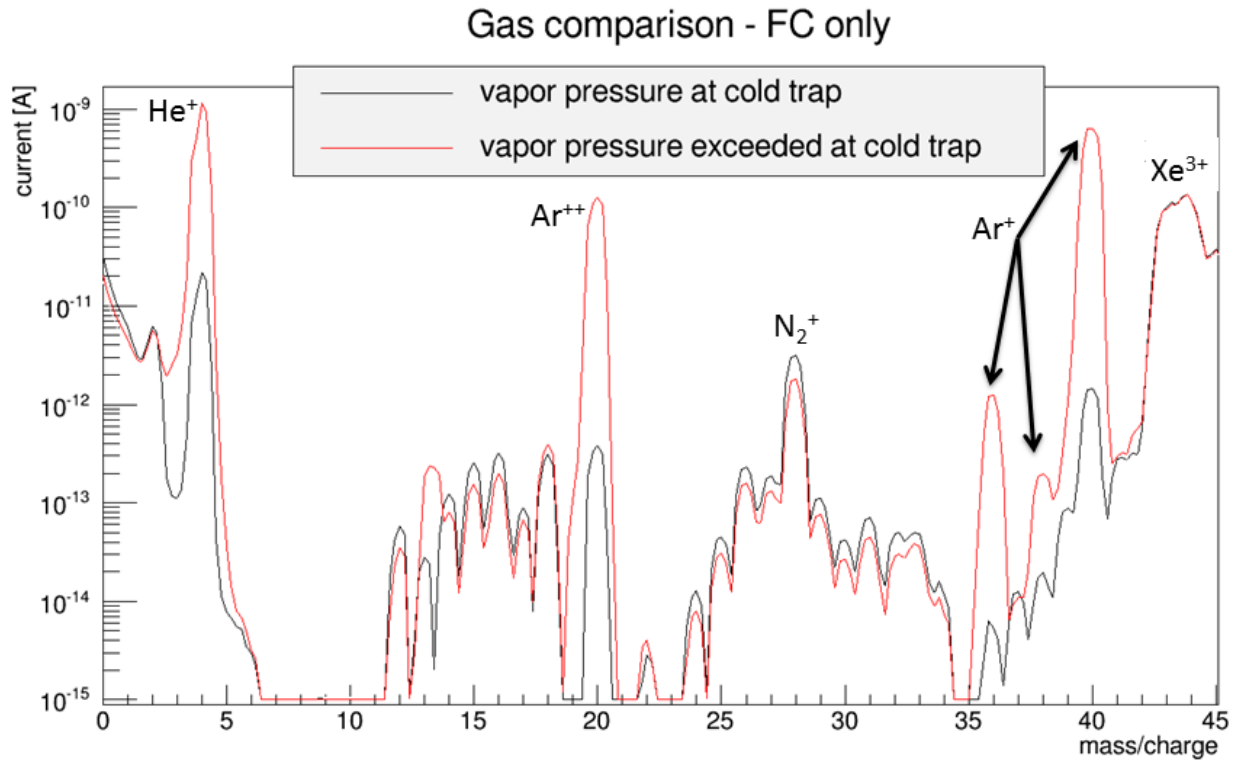
Figure 6.1: *Mass spectrum (signal current in dependence of the mass-over-charge-ratio) of masses between 1 and 45 for two different gas samples taken with the RGA-I in Faraday cup mode. While the first sample (red) was obtained from a gas bottle directly and exceeds the vapor pressure, the second sample (black) was purified gas from the distillation column, which provides vapor pressure at the cold trap.*

6.1.1 Gas purity analysis

Previous investigations made by [Bro13] and [Sch12] at the RGA-I setup, as well as [Ket12] on a preceding setup, have shown a pressure above the expected vapor pressure, when a commercial xenon sample, or any mixture derived from it, was introduced into the cold trap. This lead to the assumption, that the (different) cold traps have not been able to freeze the in-going xenon flow completely.

Due to the advantage of a working cryogenic distillation column ([Mur14]) and a first cleaning device beforehand, the so called pre-separator ([Ros14b]), it was possible to test gas samples which were purified from any gas with a higher vapor pressure than xenon, including main impurities as argon, nitrogen and helium. This kind of purified xenon gas samples have been introduced in the cold traps of both RGA setups, resulting in pressures p_{ct} (see 5.2.3) of around:

$$p_{\mathrm{ct}} \sim 3.3 \times 10^{-3}\,\mathrm{mbar}$$

A comparison to [Leo10], where a vapor pressure of 2.4×10^{-3} mbar is stated, shows a match within the error of the vacuum gauge. As within scope of this thesis, this has been observed for introduced gas volumes up to at least 1 standard liter, independent of the chosen inlet pressure, it can be assumed that the vapor pressure is achieved.

However, when gas from other sources (e.g commercial gas bottles) was measured with these setups, an excess in p_{ct} has been observed up to three orders of magnitude higher than the vapor pressure, depending on the gas source and the flow.

An analysis of the gas composition via mass spectrometry showed an increased concentration of impurities, as shown in figure 6.1. The main components of the contamination can be identified as Helium (peak at $\frac{m}{z} = 4$) and Argon (peaks at $\frac{m}{z} = 36$, 38, 40 and double ionized at $\frac{m}{z} = 20$, $\frac{m}{z} = 19$), whereas xenon is still the dominating gas. Both gases are not expected to freeze-out in the cold trap due to their high vapor pressure, so they can likely cause the excess in pressure. Another possible effect causing an overall pressure increase, is a coverage of the cold trap walls by these impurities and therefore leading to an incomplete freezing behavior of the xenon. Since this effect or the influence of the impurities on the krypton behavior in general could not be studied within this thesis (see chapter 8.1), only clean gas from the distillation column has been used for calibration and further investigation of the system.

6.1.2 The gas flow

Although, the conductance of both DPS is depending on the gas composition, it is sufficient to describe the gas flow through the DPS only in terms of xenon, as long as it is clearly the dominating component. This does not apply for the gas flow behavior inside the cold trap. Freezing inside the cold trap is the dominating process for the xenon bulk, if the pressure overcomes the vapor pressure limit at liquid nitrogen temperature, which is fulfilled for measurements within this thesis, with inlet pressures of 0.1 bar to 2.0 bar.

Nonetheless, also at pressures below this, sorption, mainly adsorption in the form of physisorption takes place, which can cause particles to be attached to the walls. This process of adsorption is energy dependent and the attachment time of an adsorbed particle increases towards lower temperatures [Wut06], leading to sticking time scales above the measurement time, which is in the order of minutes, and therefore, this particles will not reach the mass spectrometer. Despite the fact that it is even advantageous for the xenon component, due to the removing of xenon particles from the gas flow, it has disadvantages for the krypton particle amount because of the possibility of adsorption to the walls or to xenon molecules. Additionally, a reduction of the krypton amount is possible when freezing xenon traps krypton atoms within this process. The adsorption probability and the attachment time decrease with a growing particle coverage of the surface because of the change from particle - surface to particle - particle interaction, which is less stable due to the lower thermal conductivity. In spite of that the cryogenic trapping of krypton inside freezing xenon is possible as long as xenon freezes.

This kind of krypton removal is confirmed by the fact that krypton is present in the mass spectrum of the evaporating gas, when the cold trap is heated after a measurement.

Observation of the flow behavior

These effects have been observed, when comparing the flow of xenon through the system with a cold trap and without a cold trap attached.

For measurements without a cold trap, the pressure reading shows instantly the pressure provided by the in-going flow ($\mathcal{O} \sim 10^{-1}$ mbar). However, if the cold trap is used, the in-going xenon flow does not cause an instant pressure enhancement, but leads to a delayed pressure raise within a few tens of seconds up to the vapor pressure of 3.3×10^{-3} mbar. Since this is only a phenomenological observation for the xenon bulk, it still does not provide information about the krypton behavior.

Therefore, an evaluation of measurements with different inlet pressures and thus changing amounts of krypton has been made. By comparing the maximum signal height of the most abundant isotope ^{84}Kr (see table 6.1) for different inlet pressures but same krypton concentrations, the response of the system towards changing flows has been investigated (see figure 6.2). A linear dependence is indicated by these measurements and additionally, for same inlet pressures[1] a clear reproducibility has been found. These two observations allow for the assumption, that even if krypton is removed from the gas flow by the cold trap, it is a reproducible linear process, thus it is possible to apply a flow correction to account for the signal dependence on the in-going gas flow.
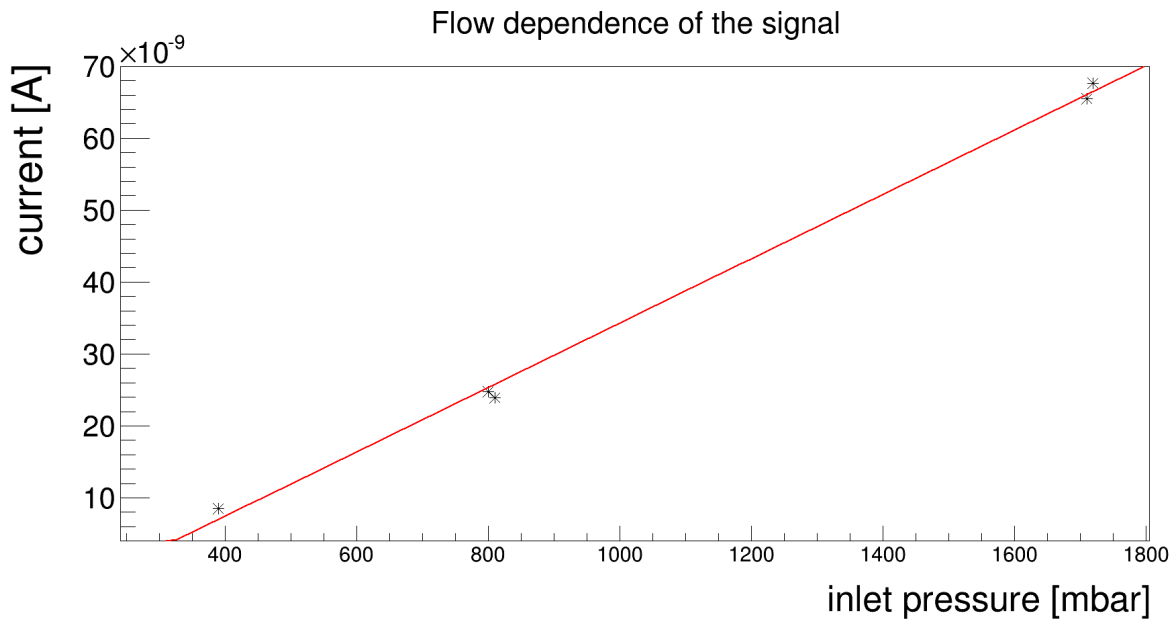

Figure 6.2: *Maximum signal height of the ^{84}Kr-signal in dependence of inlet pressure. A linear fit (red) is added to visualize the linear relation between signal and inlet pressure.*

---

[1]The pressure reading, provided by a *Swagelok PTU-S-AC931AD* pressure sensor, has a read-out error of 50 mbar
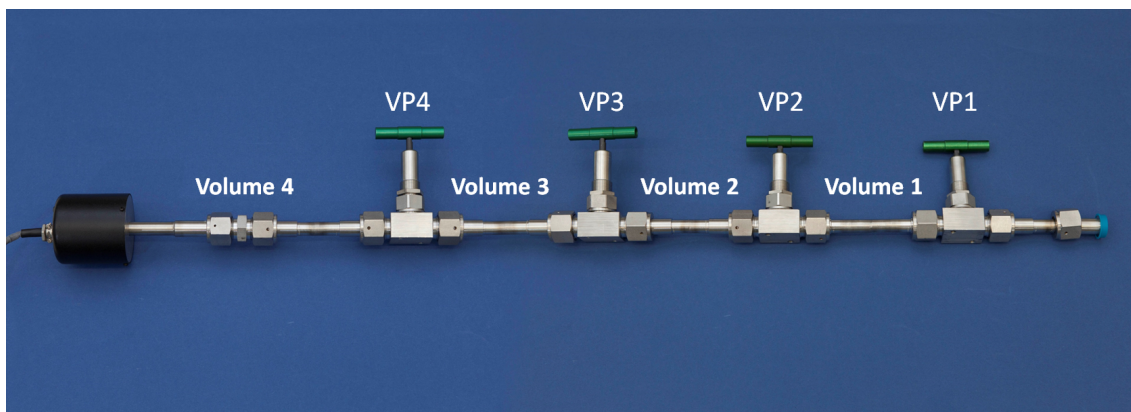
Figure 6.3: *The standard volume calibration pipette: Four valves (VP 1-VP 4) (type: Swagelok SS-8BG-VCR) have been connected via VCR to orbital welded volumes (Vol 1-Vol 4), which form an overall volume V of (69 ± 1) ml divided into four chambers. A pressure sensor (mks Baratron Type 121A) has been mounted to the last chamber for precision measurements of pressure changes during volume expansion. Additionally, this pipette is used for creating gas mixtures of known krypton concentrations (see chapter 6.2).*

Volume determination

As seen in equation 5.8, the flow is not only determined by the pressure drop over time but also by the volume used for injection. Thus, the classification of these two factors is important to make a correction for the flow behavior, if comparing signals of different samples. The pressure drop is directly measured, as already described in section 5.2.4, while the determination of the respective volume for all measurements has been done separately. For this reason a standard volume V (see figure 6.3) has been calibrated and by relative expansion measurements, using a high precision manometer (type: *mks Baratron Type 121A*) with a reading error of $0.5\,\%$ [MKS08], volumes of interest could be determined. A detailed description of the volume measurement technique and the calibration of the standard volume can be found in [Rot14]. The resulting volumes V_{meas} for the measurements, with their respective uncertainties, obtained by Gaussian error propagation, at both setups are:

$$
\begin{aligned}
\mathrm{V}_{\mathrm{meas}}^{\mathrm{RGA\text{-}I}} &= (83.0 \pm 2.6)\,\mathrm{ml} \\
\mathrm{V}_{\mathrm{meas}}^{\mathrm{RGA\text{-}II}} &= (96.0 \pm 2.7)\,\mathrm{ml}
\end{aligned}
$$

These volumes filled with around 1 bar of xenon, are the usual consumption of gas during a measurement.

6.2 Experimental calibration method

The calibration of the RGA setup requires the reproducible measurement of xenon gas with known krypton concentrations, covering a wide range of contamination, from the sensitivity

limit of the setup ($\sim$ ppt) up to concentrations at the ppm-level. Therefore, a calibration technique has been used, introduced as a so called *doping method* in [Ket12], which was improved within the work of this thesis. This method is based on an artificial enhancement of the krypton concentration in the xenon gas, by a controlled dilution and mixing procedure described in the next section.

Acting as a mixing device, the pipette shown in figure 6.3 has been attached to the RGA-II setup (see figure 6.4), which had a direct connection to the distillation column, ensuring the supply with ultra-pure xenon gas at concentrations below the ppt-level. This is important for three reasons:

- For a precise creation of a certain doping level, it is necessary to mix krypton into xenon gas with intrinsic concentrations of krypton far below the desired doping concentration.

- Before measuring a doped sample, it is crucial to check the system response to purified xenon gas.

- If any contamination occurs, it is possible to clean the system by flushing pure xenon through.

6.2.1 The doping method

Following always the same procedure[2], doping a sample for the calibration started with filling pure krypton ($>$99% purity) into the pipette (see a basic scheme of the first steps in figure 6.5) at a pressure of about 200 mbar. This pressure value was fixed as the lowest possible value, in order to reduce the impact of the pressure sensor sensitivity limit of 1 mbar to the consecutive calculated doping level (see 6.3.3). Starting with this, the concentration of interest has been created by different steps of dilution and mixing:

After pressure equilibrium, the valve above the pressure sensor (VP 4) has been closed and the three other volumes (Vol 1-Vol 3) were pumped down to at least 1×10^{-5} mbar with a dedicated pump system, which was not connected to the system for avoiding contamination. In the next step, pure xenon has been filled into the evacuated volumes Vol 1-Vol 3 with a pressure of about ~ 2300 mbar and the valve VP 1 has been closed. For starting the first mixing of krypton into xenon the valve VP 4 has been opened leading to a total pressure of 1500 mbar. Investigations on the equalization time of the krypton concentration showed (see section 6.2.2) that this process has a larger time scale than the pressure equalization, which happens instantly at valve opening. Therefore the waiting time was chosen to be at least 24 h for every mixing step in this calibration.

---

[2]The numbers used here for explanation are not exact, and just illustrating the order of magnitude used in the different calibrations
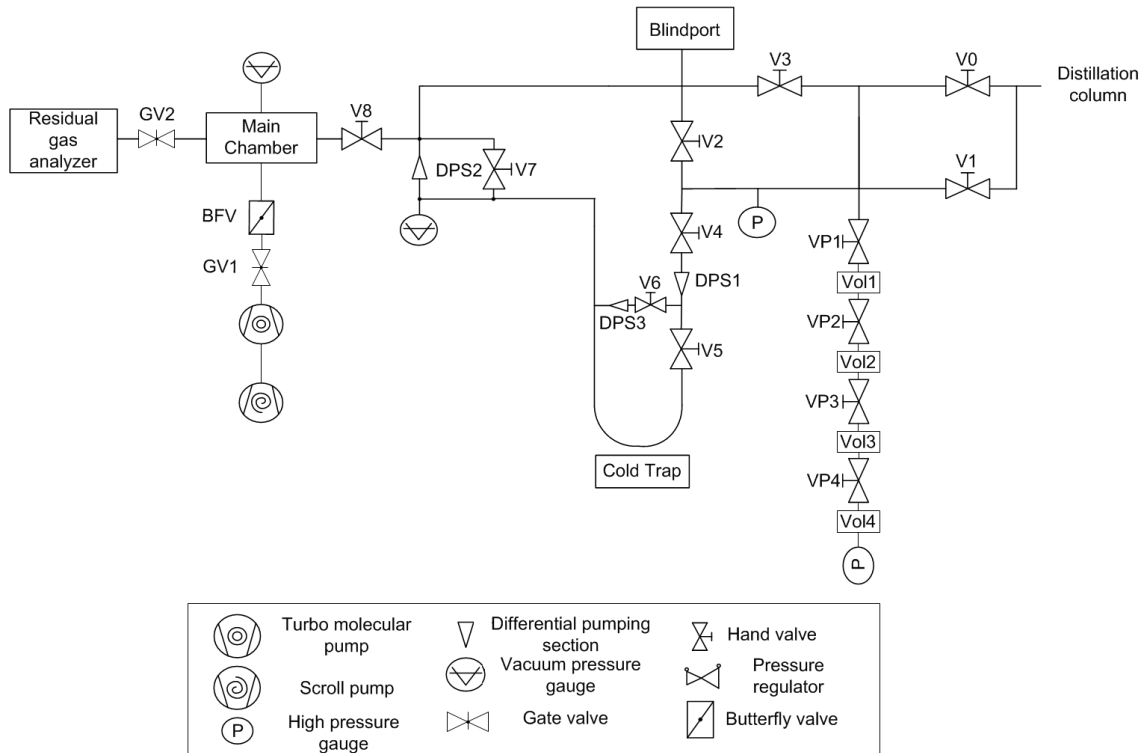
Figure 6.4: *Flow chart of the RGA-II setup with the pipette attached at the measurement volume. The first doped sample is created before attachment of the pipette.*

As the krypton partial pressure changed, due to the dilution from Vol 4 into $\mathrm{Vol}_{\mathrm{tot}} =$ Vol 1-Vol 4, the volume ratio $R_V = \frac{\mathrm{Vol\,4}}{\mathrm{Vol}_{\mathrm{tot}}}$ has to be known precisely for further calculations of the krypton concentration. Therefore the pressure change $\left(\frac{p(\mathrm{Vol\,4})}{p(\mathrm{Vol}_{\mathrm{tot}})}\right)$ of any expanding gas from Vol 4 into Vol 1-Vol 4 has been determined each time, and by calculating the mean, a ratio of

$$R_V = \frac{\mathrm{Vol\,4}}{\mathrm{Vol}_{\mathrm{tot}}} = 0.380 \pm 0.005 \tag{6.1}$$

can be obtained, with the uncertainty being the standard deviation σ_{R_V} over all measurements. By comparison of the measured total pressure p_{tot} to the calculated partial pressure of krypton p_{Kr} the concentration of krypton c_{Kr} inside the sample can be calculated with:

$$c_{\mathrm{Kr}} = \frac{p_{\mathrm{Kr}}}{p_{\mathrm{tot}}} \tag{6.2}$$

As this first mixing leads to a concentration in the order of $c_{\mathrm{Kr}} \approx 5 \times 10^{-2}$, a further dilution of the mixture was needed in order to achieve the desired concentration c_{Kr} of around 5×10^{-6}. Consequently, the valve VP 4 has been closed again and by opening VP 1, the volumes Vol 1-Vol 3 have been evacuated again, while the pressure of the gas mixture in Vol 4 stayed at a value of about 1.5 bar. This has been expanted two more times into Vol 1-Vol 3 to get a left-over sample in Vol 4 of $\sim 200\,\mathrm{mbar}$, which could be mixed with purified xenon again. Therefore, the steps done beforehand were repeated for this sample until the concentration of interest was achieved.
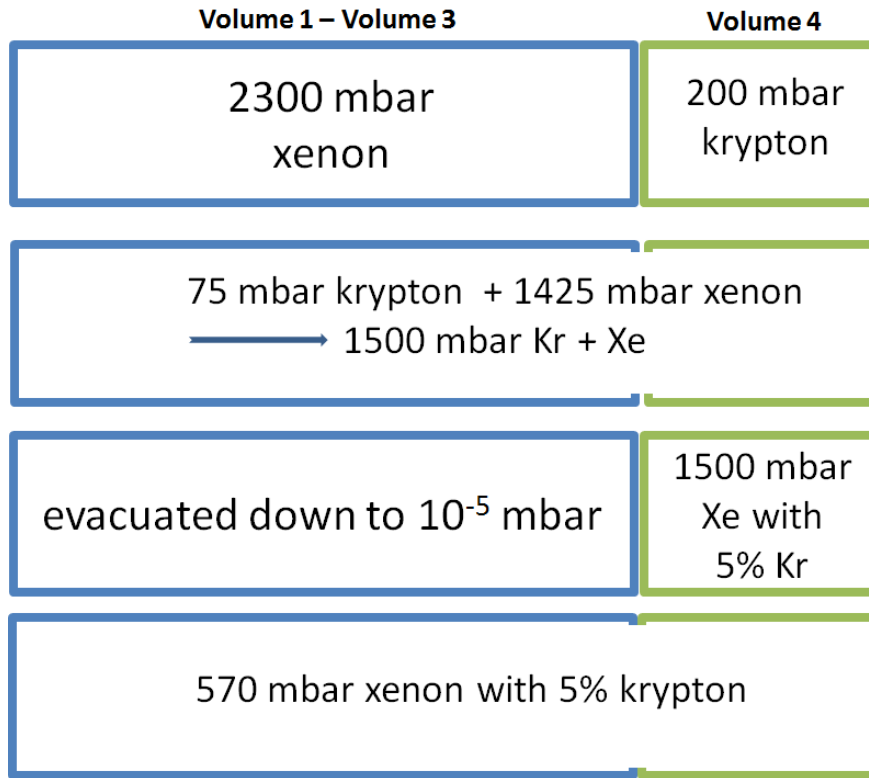
Figure 6.5: *Scheme of the first doping steps. Vol 1-Vol 3 is indicated by a blue box, while the mixing volume Vol 4 is represented by a green box. If the contours are closed the valve VP 4 is closed, if the connection is open, it indicates that VP 4 is open. Every mixing dilutes gas from Vol 4 by a factor of 0.38 and gas from Vol 1-Vol 3 by a factor of 0.62 as indicated roughly by the exemplary figures calculated here.*

For the first measurement the pipette was attached to the respective RGA setup as shown in figure 6.4 for RGA-II. Before any calibration measurement, a krypton-depleted gas sample has been measured, to ensure a correct response of the system. The pipette has been opened afterwards and the gas with the ppm-concentration was diluted from Vol 1-Vol 4 into the measurement volume V_{meas} of the RGA system. Before an actual calibration measurement, the pipette was closed off at VP 1 and VP 4 to prohibit a flow increase by adding this extra volume. After the measurement, Vol 1-Vol 3 were evacuated again and filled with a pure xenon sample taken from the distillation column. Consecutively, closing VP 1 and opening VP 4, has lead to a further dilution of the ppm-sample due to the mixing with the purified xenon. The dilution factor R_c for this mixing is given by:

$$R_c = \frac{c_{\mathrm{Kr}}^{\mathrm{start}}}{c_{\mathrm{Kr}}^{\mathrm{end}}} \tag{6.3}$$

As $c_{\mathrm{Kr}}^{\mathrm{start}}$ is known already, the calculation of $c_{\mathrm{Kr}}^{\mathrm{end}}$ leads to a direct determination of R_c:

$$c_{\mathrm{Kr}}^{\mathrm{end}} = \frac{c_{\mathrm{Kr}}^{\mathrm{start}} \cdot R_V \cdot p(\mathrm{Vol\,4})}{p(\mathrm{Vol\,4}) \cdot R_V + p(\mathrm{Vol\,1} - \mathrm{Vol\,3}) \cdot (1 - R_V)} \tag{6.4}$$

As the volume ratios are fixed by the pipette design (see equation 6.1), the further dilution depends only on the pressure ratio of the purified xenon gas in Vol 1 - Vol 3 to the mixed xenon gas in Vol 4. For the calibration measurements a dilution factor of around 7.5 was used.

The sample with the new concentration has been measured after fulfilling the waiting time of 24 h. Applying this method, a complete calibration set from 10^5 ppb down to 10^{-2} ppb has been created. Theoretically, since the provided mixing gas was purified down to the ppq-level, a calibration down to this value could also be achieved, but the sensitivity of the setups is the limiting factor at this point(see 6.3.4.)

6.2.2 Diffusion of krypton in xenon
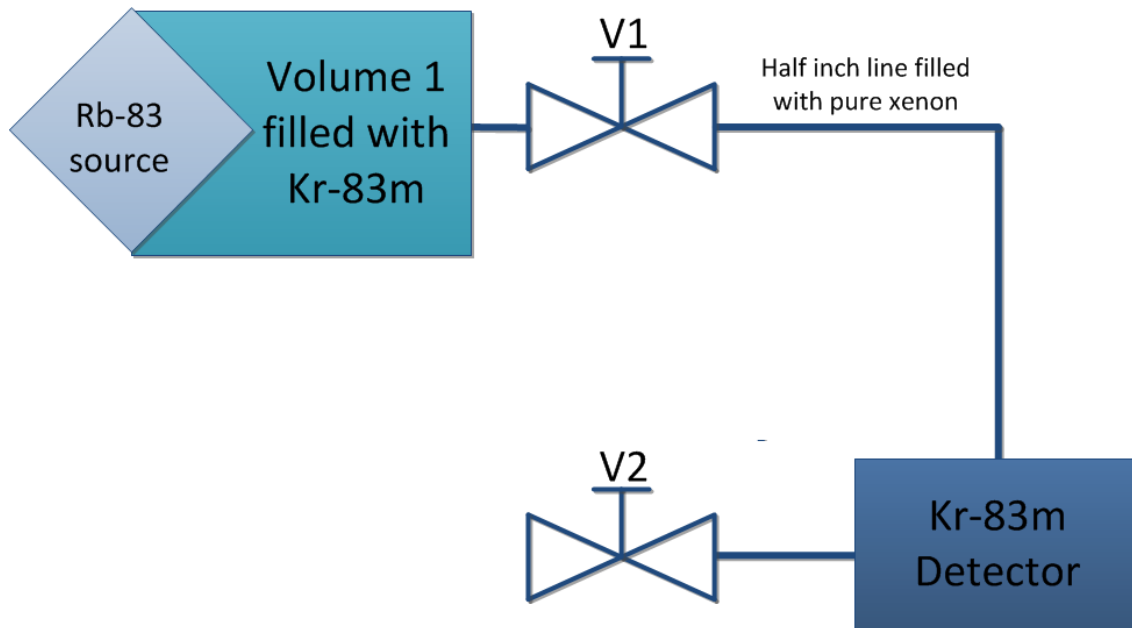
Figure 6.6: *Setup for the determination of the diffusion time scale. A radioactive* ^{83}*Rb is used to produce the short-lived radioactive isotope* ^{83}*Kr, which is released after accumulation into a volume monitored by a detector system. The signal rate is directly proportional to the concentration of the krypton particles, as detected signals are produced by the decay of* ^{83}*Kr.*

During the calibration process non-linear results have been observed if the measurements, and thus the mixing of xenon, were executed on a time scale of ~ 2 h. Therefore, to validate a relation between the mixing time and the results, two different methods, described in this section, have been applied.

Firstly, a cross check measurement has been performed using the calibration pipette (see figure 6.3), where Vol 1 - Vol 3 have been filled with purified xenon and Vol 4 was already filled doped xenon gas. As the valve in between has been opened, the pressure directly equalized. As soon as this happened, the valve VP 3 has been closed to separate the two volumes again. While volumes Vol 1 and Vol 2 of the pipette were measured without any further contact to the other volumes, the volumes Vol 3 and Vol 4 of the pipette have been left connected for one additional day.

A measurement of these two different volumes (Vol 1 + Vol 2 vs Vol 3 + Vol 4) showed a difference by four orders of magnitude in the signal level. A possible explanation for this is a large time scale for the equilibrium diffusion process of krypton into the xenon, contrary to the process of pressure equalization.

For an understanding of this time scale, a second dedicated measurement has been performed using the diffusion of the radioactive ^{83}Kr into a xenon volume without a forced flow and detect its decay over time. Figure 6.6 shows the setup for the diffusion time scale measurement. A radioactive ^{83}Rb-source (details see [Han11]), with an activity level of about 60 MBq, has been attached to a small volume (Volume 1), which was evacuated before the measurement. Afterwards it has been filled with ~ 2 bar of purified xenon gas and then isolated from the rest of the setup by closing of valve (V1). As ^{83}Rb decays into ^{83m}Kr, the volume has been filled constantly with this isotope, which has a half-life of 1.83 h until a secular equilibrium was reached. Therefore, a waiting time of one day was maintained before V1 was opened. This allowed the krypton particles to diffuse into the xenon gas in the volume between V1 and V2. It is important to point out that the xenon pressure here was equal to the pressure in Volume 1. A detector, mainly consisting of an optimized photomultiplier tube (PMT), is mounted at the end of this volume in a T-piece made of stainless steel. This detector is able to register the VUV-scintillation light of xenon, which is produced due to the interaction with the decaying isotope ^{83m}Kr (details on the detection method can be found in [Ros14c]). Hence, the concentration of ^{83m}Kr atoms in the detector volume is directly proportional to the signal rate at the detector. This signal rate is shown as a function of time in figure 6.7. For an extraction of the equilibrium time, the time constant τ of the system has to be known. Thus, an approximation by fitting an analytical integration of the charging function[3] $(1 - e^{-t/\tau})$ with a Gaussian[4] has been performed. This fit function, which is theoretically well-motivated, has been selected because of the similarity of this process to the charging of a capacitance, but as the krypton particles have a finite speed, a delay with an additional Gaussian smearing has to be included, accounting for this. The fact that the signal is delayed in the beginning points towards this finite particle velocity, as it takes at least about 1 h before any signal rate is observed. As the fitting parameters, provided by MINUIT, showed that the standard deviation (width) σ of the Gaussian is smaller by a factor of 4, compared to the time constant of the charging function $\tau \approx 12\,000$ s, only the charging function has been taken into account for the equilibrium time scale estimation.

---

[3]This function is motivated by the solution of a differential equation derived from Fick's first law.

[4]The theoretical basement for the assumption lies in Einstein's diffusion law [?].
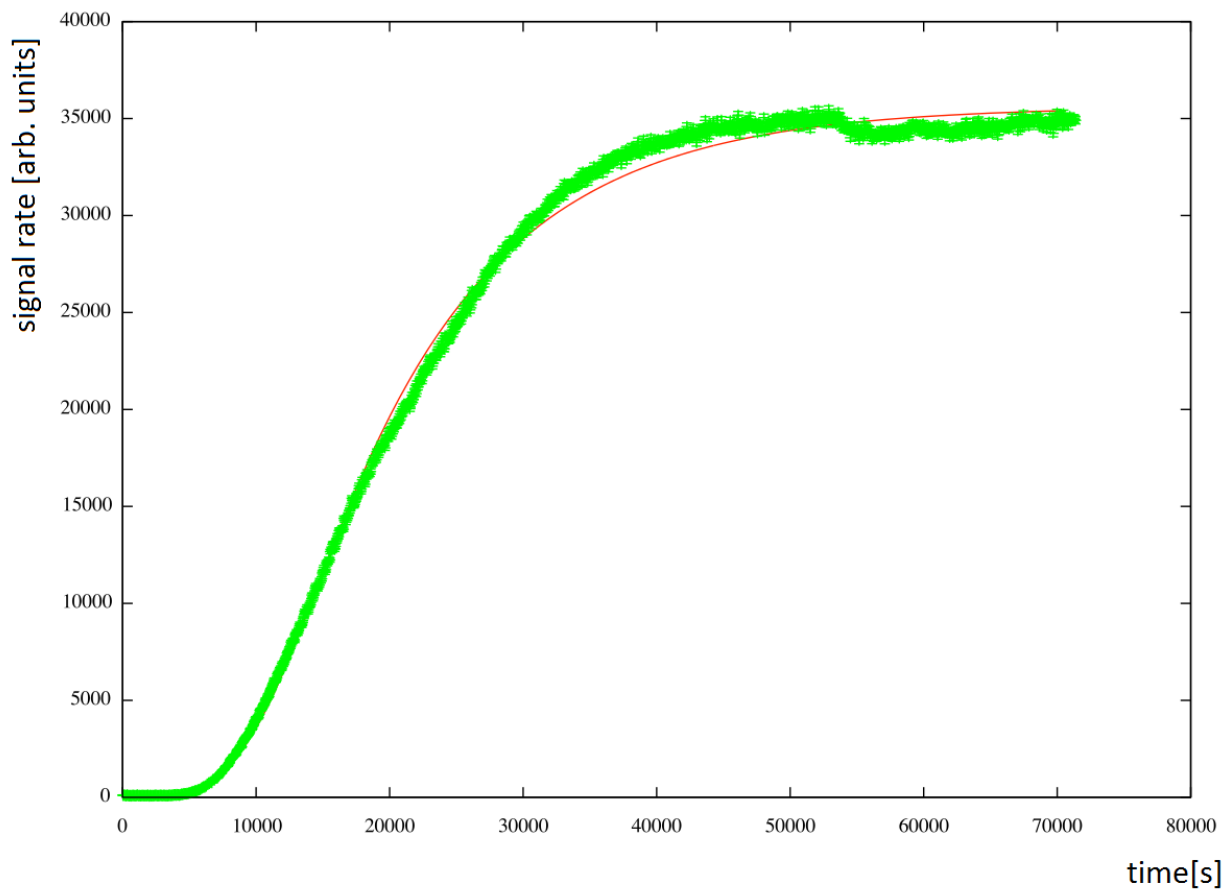
Figure 6.7: *Signal rate over time for the ^{83m}Kr. The valve was opened at $t = 0$ s. As described in the text a fit function is approximated. The reduced χ^2_{red} is 21.5, calculated by the MINUIT package. Although this differs from the optimum value 1, the approximation looks sufficient for an estimation of the equilibrium time. It has to be noted that the data was binned over 60 seconds.*

Therefore a calculation of the time t_{diff}, where the charging function has reached 99 % of its signal height by

$$0.99 = 1 - e^{-t_{\mathrm{diff}}/\tau} \tag{6.5}$$

provides a value of

$$t \approx 55\,000\,\mathrm{s} = 15.3\,\mathrm{h}$$

for $\tau \approx 12\,000$ s. This time value can be approximated as the time scale needed for equilibrium, as the signal is already at 99 % of its total height. For the diffusion process, this means that the amount of particles leaving the volume of interest (in front of the detector) and particles entering the volume of interest are almost in equilibrium.

Although this is only an estimation, as the geometry of this test setup differs from the actual pipette, the measurement itself verifies the assumption of a diffusion on the scale of hours, instead of an instant process. This makes a waiting time between the separate mixings necessary and also shows that 24 h waiting time was sufficient as it was maintained within all calibration measurements.

Table 6.1: Isotopes of Krypton and their relative abundance [Lid07]

Isotope	Abundance in %
^{78}Kr	0.35
^{80}Kr	2.25
^{82}Kr	11.6
^{83}Kr	11.5
^{84}Kr	57.0
^{86}Kr	17.3

6.3 Analysis results of calibration

This section will introduce the analysis method used for analyzing the prepared dopings by reference to one high doping example and one low doping example. Afterwards the calibration of both RGA setups will be presented. In addition to this, the sensitivity limit of each setup will be discussed.

6.3.1 Measuring a highly doped sample

Calibration measurements have been started by filling the measurement volume V_{meas} determined in section 6.1.2 for the respective RGA-setup.
After opening the inlet valve V 4 (see figure 6.4) the gas has surpassed the differential pumping section DPS1 into the cold trap. From the cold trap it has proceeded through the DPS2 into the measurement chamber, where the butterfly valve has been closed to 0° for a maximum in sensitivity during all calibration measurements. The detection was done by the residual gas analyzer, which was used in the combined Faraday cup (FC) and electron multiplier (EM) mode. An operating voltage of 1500 V has been set at the EM and an integration time of 64 ms has been chosen for each of the 5 data points between two different masses. This has lead to an average measurement time of 4.31 s for the chosen mass-over-charge $\frac{m}{z}$-range from 76 to 88. Accounting for the sensitivity and eventual slight peak shifts from the center of mass, a current shown within this thesis, has always been averaged over 3 data points for each mass. For example, a signal shown for the mass-over-charge ratio at 84.0 is an averaged integration of the data points at 83.8 , 84.0 and 84.2 (see [Ket12] for analysis of the integration range).
The signal for each isotope (current in dependence of mass-over-charge ratio) as a function of time is shown in figure 6.8 for an example measurement at the RGA-II setup, with a total doping level of 1380 ppb. After introduction of the gas sample, a signal increase by several orders of magnitude can be observed, which is delayed by 5 to 10 seconds, depending on the respective krypton isotope. The shoulder-like signal behavior between 30 and 50 seconds after valve opening, was clearly visible in every doping measurement above 1 ppb, but is not understood. Most likely it is a characteristic effect of the RGA-II system, as the RGA-I setup has not shown such a behavior during any measurement made in the scope of this thesis. As this is an effect at the gas introduction, before the system reaches equilibrium, it is interesting for understanding the system. Nonetheless, it is not necessary for calibration,
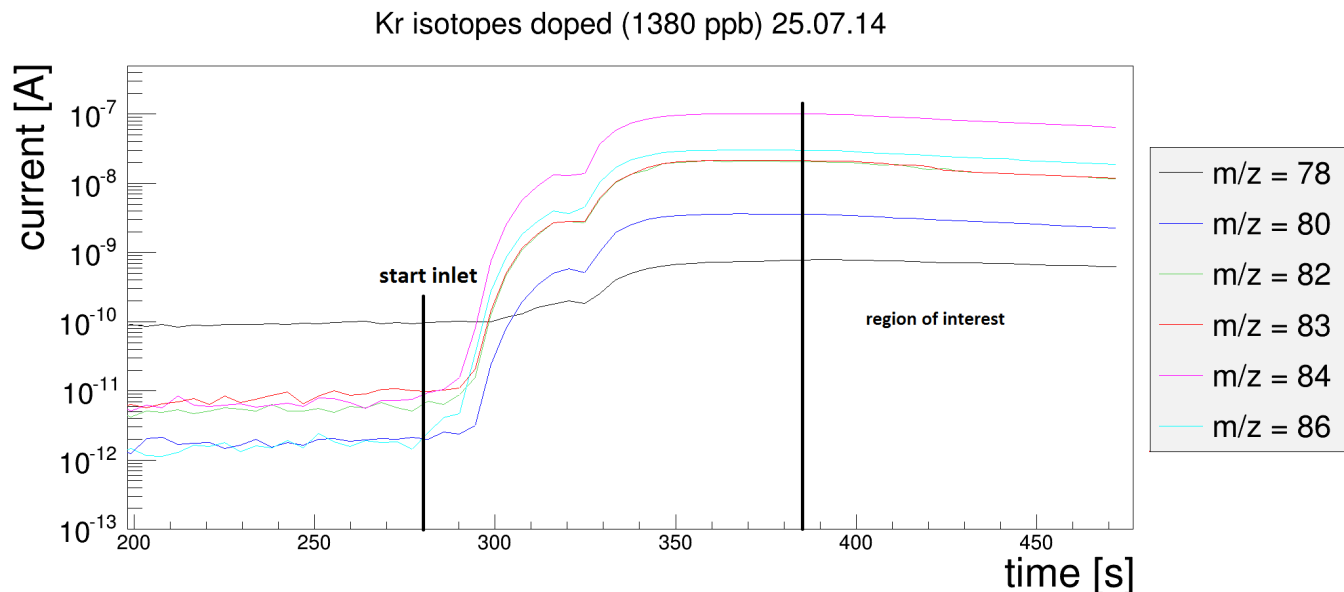
Figure 6.8: *Current (signal) time evolution for the krypton isotopes (see table 6.1). It has to be noted that the ordinate has a logarithmic scale. The moment, where the gas flow into the system starts, is indicated by a black line at $t = 280\,$s. As the data is only recorded around every four seconds for a specific mass value, the shown lines are only a linear interpolation of discrete data points. This data has been recorded with the Faraday cup and the electron multiplier activated, working at 1500 V.*

since only data which can be corrected by the inflow is used, in order to guarantee comparability of different measurements.

For this correction, the inflow has been calculated as described in section 5.2.4 and a region of interest has been selected, where the flow correction can be applied (see figure 6.8). This selection has been performed by choosing the part of the signal, where it follows the expected behavior analogous to the flow, which means a gradual decrease in signal height. This is justified, as the increase beforehand is not theoretically motivated by the inflow, while the decrease can be explained by the decreasing inflow.

A signal in the region of interest $I(t)$ can be corrected into $I_{\text{corr}}(t)$ by the inflow $q(t)$ as following:

$$I_{\text{corr}}(t) = I(t) \cdot \frac{q_{\text{normal}}}{q(t)} \tag{6.6}$$

For normalization a constant normal flow q_{normal} with a value of $0.317\,\frac{mbar \cdot l}{s}$ has been used, which is an average flow value of a typical xenon gas measurement. Figure 6.9 shows the flow correction applied to the signal in the region of interest and it can be seen, that a part of the corrected signal is nearly constant, which is caused by a direct relation to the inflow without any (non)-linear effects, as described in chapter 6.1.2. Only this almost constant part of the corrected signal, which starts at about 380 s after data taking, is used in order to determine a signal mean $\bar{I}$ of each isotope. Hence, the signal for every isotope is averaged
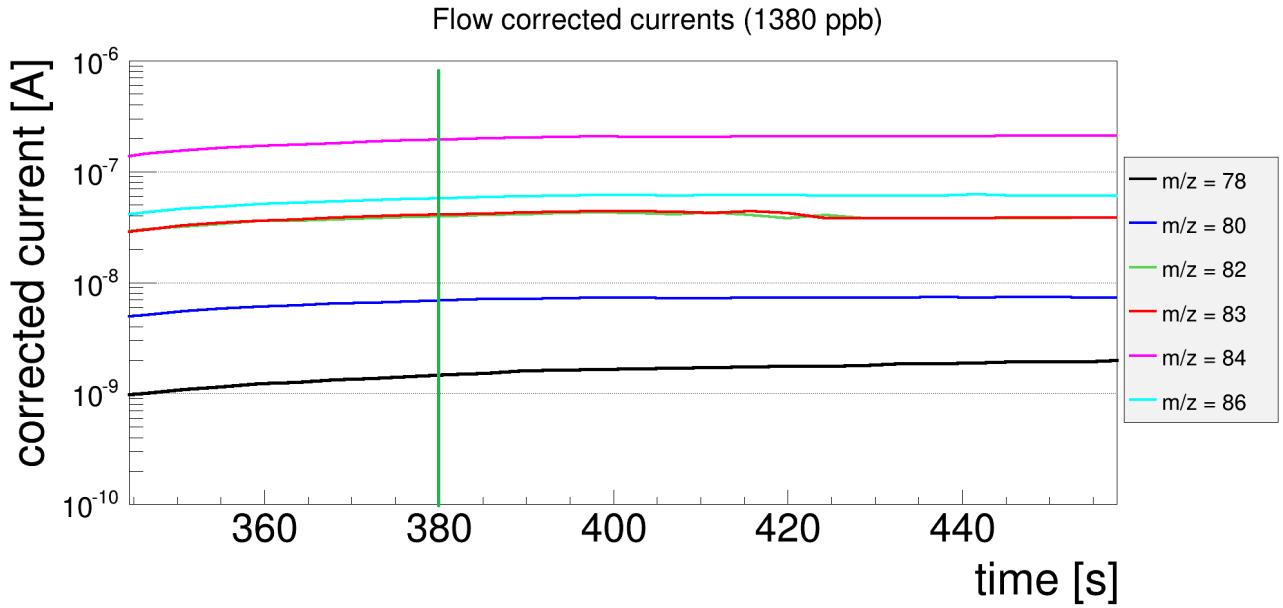
Figure 6.9: *Corrected current versus time. A zoom into the signals within the region of interest with the flow correction applied is shown. Additionally a green line marks the beginning, where the flow correction leads to a constant corrected signal, indicating that krypton inflow is in equilibrium and therefore correlated to the flow.*

over this sector and the corresponding uncertainty is given by the standard deviation $\sigma_{\overline{I}}$.

An analysis done in this way is neglecting background effects of the mass spectrometer, which is justified by the observation that all isotope signal levels (except ^{78}Kr) are at least three orders of magnitude above the background level. This can be seen in figure 6.8 at the time before gas introduction (0 s - 280 s). However, since it is not verified that the background level does not change with a general pressure increase, an independent cross check can be performed by comparison of the theoretical isotopic fraction with the measured krypton isotope signal ratios. Therefore, the recorded data of the most abundant isotope ^{84}Kr has been fixed to its theoretical relative abundance 0.57 by introducing a conversion factor α based on its signal mean:

$$\alpha = \frac{0.57}{\overline{I}(^{84}\mathrm{Kr})} \tag{6.7}$$

This way the signal ratio R_{8X} of each isotope ^{8X}Kr has been calculated relative to the signal of ^{84}Kr by:

$$R_{8X} = \alpha \cdot \overline{I}(^{8X}\mathrm{Kr}) \tag{6.8}$$

In figure 6.10 the comparison of the calculated values from the measurement with the theoretical values (see table 6.1) is shown. As it can be seen, the isotopes match the natural abundance. The isotope ^{78}Kr is not included because of two reasons: It is the least abundant isotope and additionally, the background level at the mass-over-charge ratio of 78 is about two orders of magnitude higher than for any other isotope (see figure 6.8). A high background at this mass-over-charge ratio has been observed in both setups and by other measurements [Ket12] beforehand, explained presumably by a hydro-carbonic impurity.
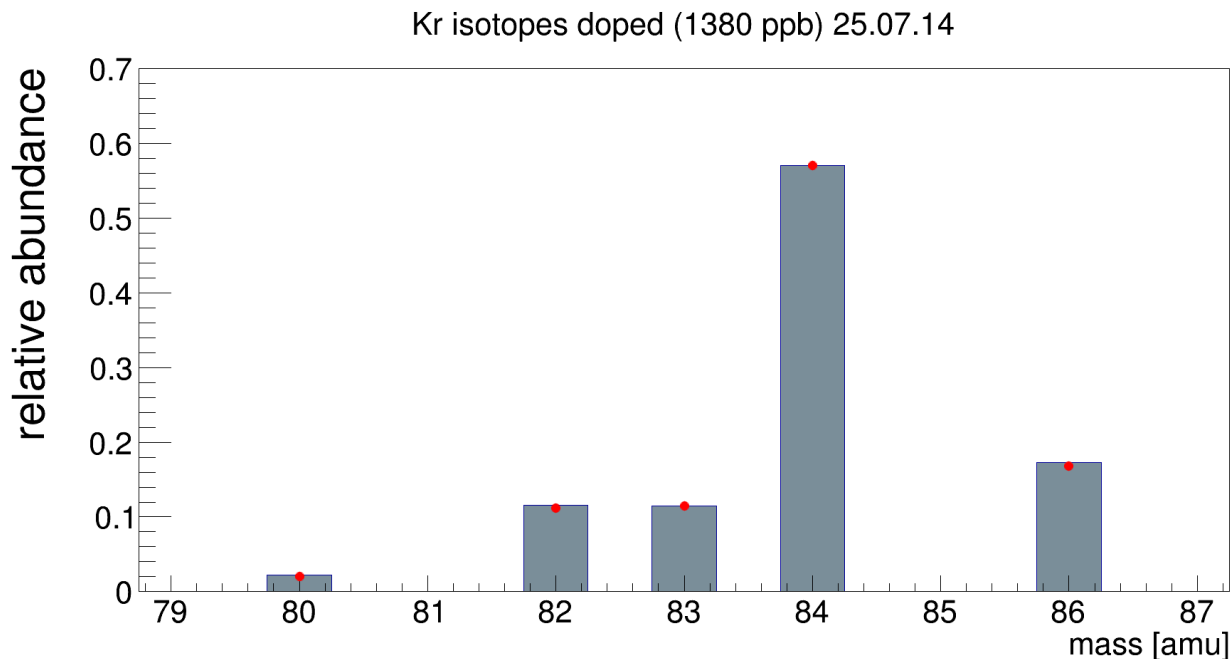
Figure 6.10: *Comparison of the relative abundance for the different krypton isotopes. While the theoretical relative abundance is indicated by the height of the grey columns, the measured relative abundance is marked with red markers. The value for the measured data of ^{84}Kr is fixed to its theoretical value (0.57) and the others are calculated relatively by the measured signal value according to equation 6.7 and 6.8.*

6.3.2 Analysis of a low doped sample

As the concentrations approach the sub-ppb level, the cross check for the isotopic krypton composition reveals an increasing discrepancy of the theoretical expected values for the relative abundance and the measured signals (see figure 6.11). Considering this, an analysis of low concentrations can not neglect the background, as it is close to the signal at this point. For the isotopes ^{82}Kr and ^{83}Kr this effect is already observed above the ppb-level, because of the high background at mass 82 and 83 in combination with their lower abundance compared to ^{84}Kr and ^{86}Kr (see 6.1). Consequently, these two most abundant isotopes, which also have the lowest background, are used for further analysis. As their background signal does not show the correct relative signal strength for these two isotopes[5] coincidentally, it is sufficient to compare the measured signals of ^{84}Kr and ^{86}Kr for a clear distinction of a krypton signal from the background.

Figure 6.12 shows the time evolution of the current at the RGA-I setup for a gas sample artificially doped with a concentration of about 0.37 ppb.

The gas inlet valve has been opened 410 s after data taking started, which confirms a signal delay of 5 to 10 seconds also in the RGA-I setup. Although, a clear increase in signal rate compared to the background level before injection has been observed, the relative abundance does not match the natural values (see figure 6.11). However, the signals of ^{84}Kr and ^{86}Kr

---

[5]The ^{84}Kr is 3.29 times more abundant than ^{86}Kr in the natural composition.
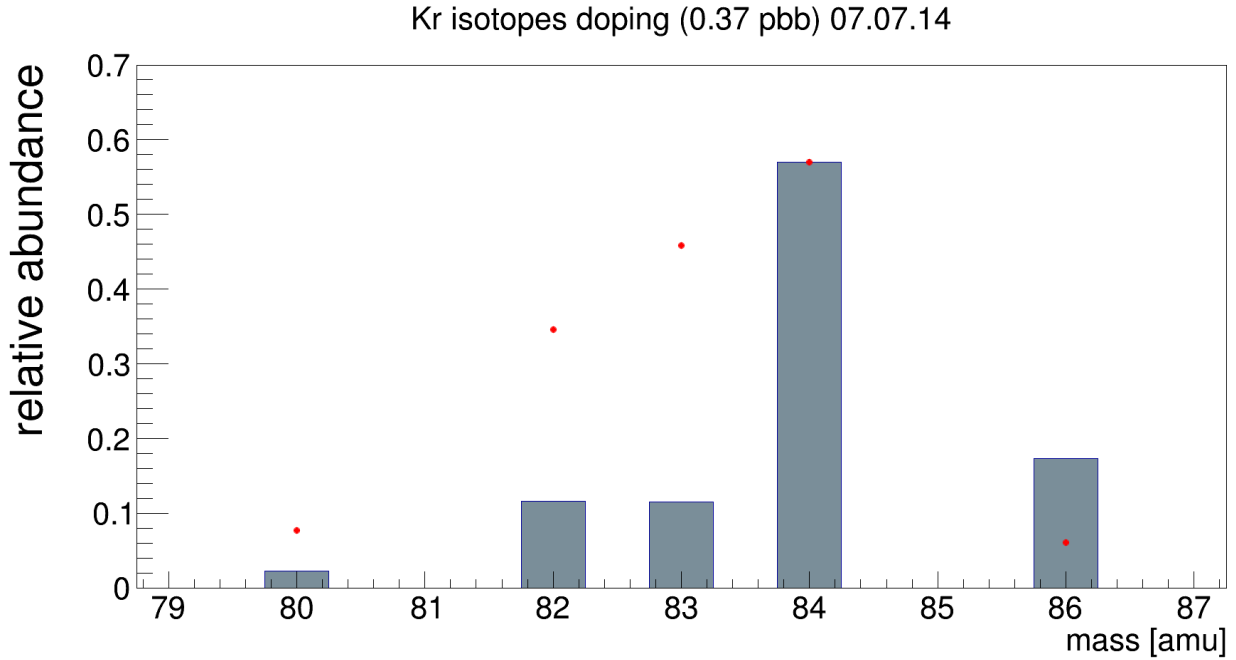
Figure 6.11: *Comparison of the relative abundance for the different krypton isotopes in the gas sample with an intrinsic concentration of 0.37 ppb. The measured relative fraction of ^{84}Kr towards the other isotopes is not matching the theoretical values anymore. An offset in the ^{84}Kr signal can be excluded, as the relative abundance of the other isotopes is shifted in both directions.*

show a pattern, in contrast to the lesser abundant isotopes, which leads to the conclusion that a signal is present:

First, both signals rise after injection by at least one order of magnitude, while this is not the case for the clearly background dominated ^{78}Kr or the presumably background dominated isotopes ^{82}Kr and ^{83}Kr. Second, the expected decrease in signal strength with reduced flow is observed at the most abundant isotopes, while it is not for the background dominated ones (e.g. ^{80}Kr). Additionally, if the flow correction is applied, as it was in the high-doping analysis, the corrected signals are not becoming constant, but are increasing with different slopes depending on the respective isotope. This is explainable through a background signal, which is flow-independent, but corrected by the flow. In order to account for the influence of the constant background at the signal detection, a different analysis approach is applied. Therefore, a fit function $\gamma(t)$ is directly approximated to the raw signals $I(t)$ of the isotopes with a term accounting for the flow-depending signal and one term for the consideration of the constant background signal I_0. This fit function can be defined as:

$$\gamma(t) = I_s \cdot \frac{q(t)}{q_{\mathrm{normal}}} + I_0 \tag{6.9}$$

The constant factor I_s describes the flow-corrected signal component, which is approximately the same as $\bar{I}$ in the high-doping analysis, if the background is small compared to the signal. For an approximation to the raw signal, this flow-corrected signal mean needs to be multiplied by the flow to account for the time evolution. The flow-normal q_{normal} could be included

also
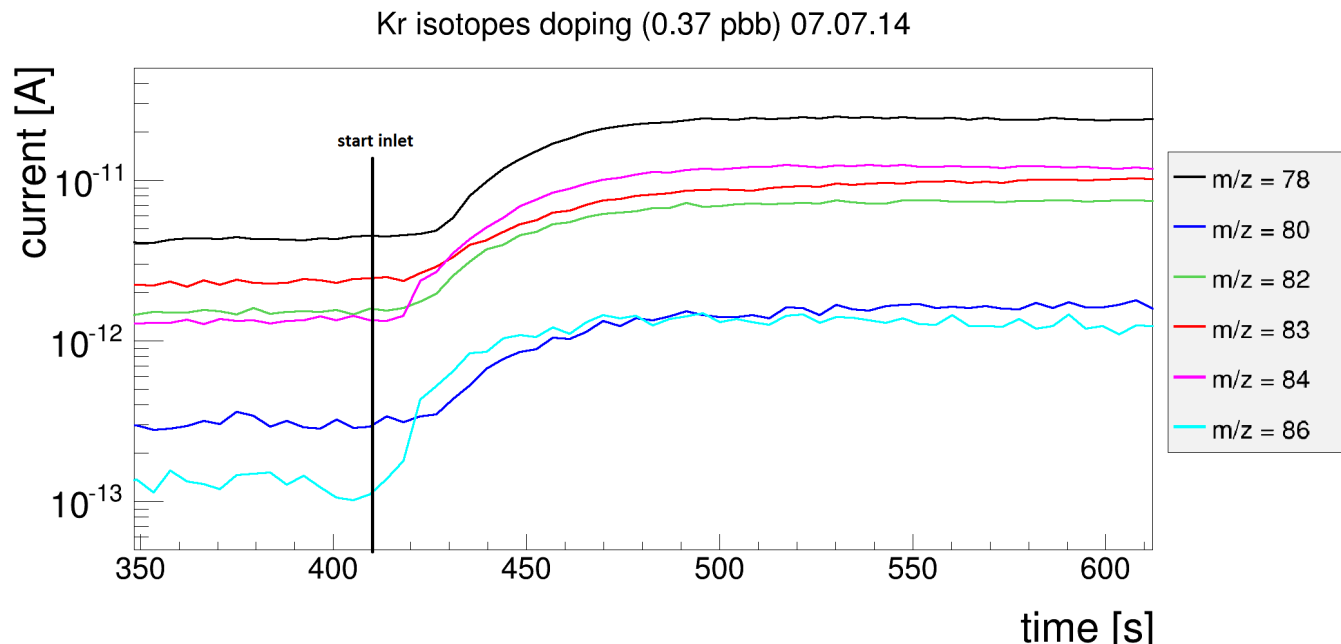
Figure 6.12: *Signal time evolution for the different krypton isotope masses for a doping of about 0.37 ppb. The valve was opened at $t = 410\,\mathrm{s}$, and the butterfly valve was set to $0°$.*

into the I_s component, but this way the low-doping analysis and the high-doping analysis are comparable and this values can directly be used for an overall calibration of the systems. In figure 6.13 the resulting approximation, which has been performed by the ROOT package MINUIT using the MIGRAD fit routine, to the raw current of the isotopes ^{84}Kr and ^{86}Kr is shown. For a comparison of the two methods (high-doping analysis and low-doping analysis) the example with a calculated concentration of 0.37 ppb has been analyzed both ways, resulting into two different corrected signal means $\overline{I}/I_s$ for each isotope[6]. Using the low-doping analysis method, the obtained relative abundance is close to the natural value (3.50 vs 3.29) while for the high-doping analysis method it differs by a factor of ~ 3 from the natural ratio.

Table 6.2: Comparison of the corrected isotopic signal mean for the low-doping I_s and the high-doping $\overline{I}$ analysis.

	I_s [A]	$\overline{I}$ [A]
$(^{84}\mathrm{Kr})$	$(4.42 \pm 1.65)10^{-12}$	$(4.53 \pm 0.27)10^{-11}$
$(^{86}\mathrm{Kr})$	$(1.23 \pm 1.01)10^{-12}$	$(4.84 \pm 0.31)10^{-12}$

---

[6]For discrimination of the two analysis methods the corrected signal mean is noted as I_s for the low-doping analysis, and $\overline{I}$ for the high-doping analysis. As the calibration will use both values, depending on the doping, the notation for the corrected signal mean will be $\overline{I_s}$.

Kr isotopes doping (0.37 pbb) 07.07.14
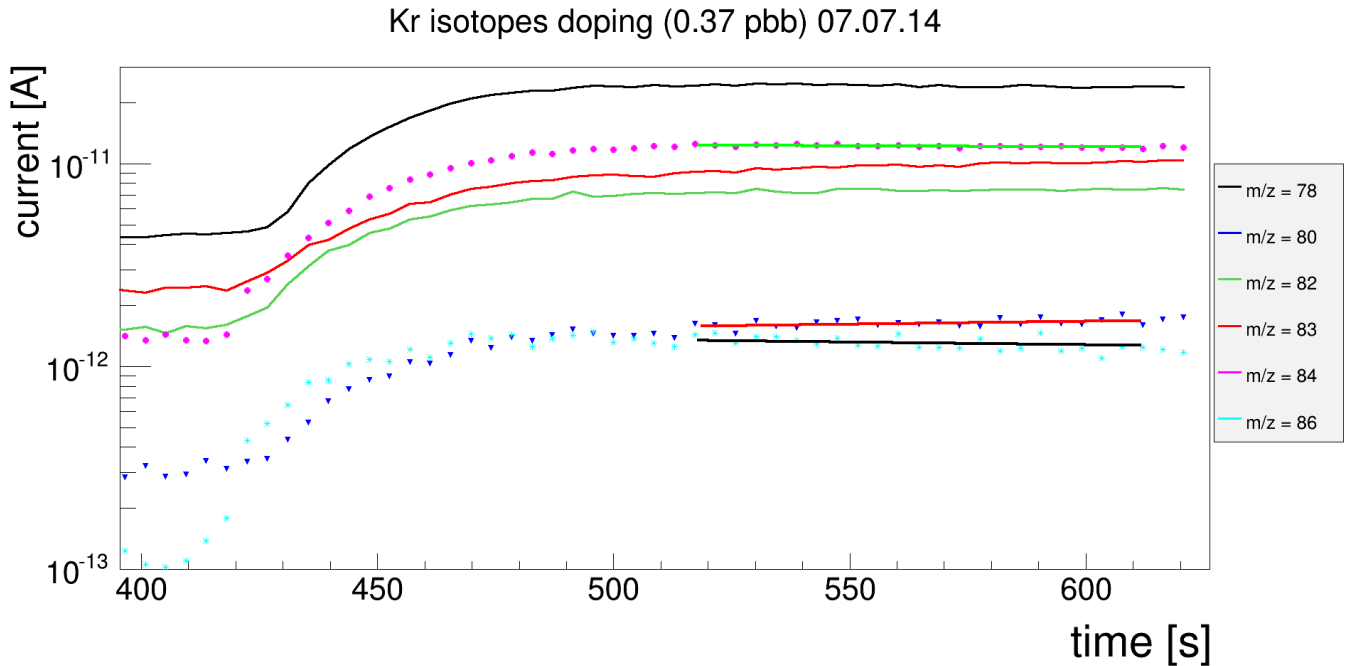
Figure 6.13: *Uncorrected signal time evolution for different krypton isotopes. Three fit func-tions for the isotopes ^{84}Kr (green) and ^{86}Kr (black) and the presumably back-ground dominated ^{80}Kr (red) have been approximated as described in the text. For a better visibility these data sets are indicated with markers instead of the interpolated lines. The different behavior of the current at mass-over-charge ratios 86 and 80, directs towards the existence of a signal at $\frac{m}{z} = 86$, since this measured current is decreasing over time, while the current of $\frac{m}{z} = 80$ is not.*

6.3.3 Calibration

One calibration set, including seven different dopings from the ppm-level down to the the sub-ppb level, has been prepared for each RGA setup in the described way (see section 6.2.1). For ^{84}Kr and ^{86}Kr a correction of the signal by the inflow has been applied by one of the two different analysis methods previously presented. The method was chosen depending on the artificial doped concentration and the investigation of the isotopic fractions. Although, the low-doping analysis method should also be applicable to high-doping samples, the ap-proximation for samples above 100 ppb was not possible, as the software package was not able to fit samples, where the background was several orders of magnitude below the signal. In the transit-region of high-doping samples and low-doping samples (1 ppb - 100 ppb), both analysis methods generate equal values for the signal mean within the uncertainties. This was used as a cross check, but generally the low-doping analysis provides physically reason-able values for any measurement, where the background becomes significant, and thus, the isotopic fractions do not match anymore, without correcting for the background.

A calibration is now given by the dependency of the corrected current signal mean for the two most abundant isotopes $\overline{I_s}(^{84}\text{Kr},\,^{86}\text{Kr})$ and the total krypton concentration c_{Kr}. Therefore, as the RGA has supposedly a linear response to equal concentrations, a fit function of the form

$$\overline{I_s}(^{84}\text{Kr},\,^{86}\text{Kr}) = k(^{84}\text{Kr},\,^{86}\text{Kr}) \cdot c_{\text{Kr}} \tag{6.10}$$

has been used for calibration. The conversion factors $k_{84\text{Kr}}$ and $k_{86\text{Kr}}$ can be directly used for transforming a given flow-corrected current into the intrinsic concentration and thus, they have the dimension $\frac{A}{ppb}$. As shown in figures 6.14 and 6.15 these fit functions, fitted again by MINUIT, match the measured calibration data, and thus a linear response can be confirmed. For the uncertainty estimation the uncertainties of both quantities (corrected current and the artificial doping level) have to considered. While the corrected current has an uncertainty given by its standard deviation $\sigma_{\overline{I_s}}$, which is indicated in the calibration plots by the vertical error bars (ordinate), the calculation of the uncertainties of the concentrations is more complex. This is due to the fact that by creating the samples as described in section 6.2.1, two different quantities lead to a propagating error through every dilution and mixing step. These are the pressure reading p_{Kr} in Vol 4, read-out by the pressure sensor, with a $0.5\,\%$ reading-error Δp_{Kr}, and the volume fraction R_V (see equation 6.1), which is used for calculation of the krypton partial pressure with every dilution. This leads to a correlation of the uncertainties of the different concentrations. Calculations showed that the error of the pressure reading is neglectable, as its influence is only measurable for an uncertainty at the first mixing, when a read-out of pure krypton is made. However, this still has an influence of less then $1\,\%$ and is small compared to the impact of R_V.

In order to account for the correlation of all artificial dopings, the following method has been used to determine an uncertainty Δk for a given calibration set:

While the corrected signals and its errors have been kept constant (error at the ordinate), the concentrations have been calculated for a variation $R_V \pm \Delta R_V$ of the parameter R_V by its uncertainty ΔR_V (see equation 6.1). This way the fit function 6.10 has been approximated for all three possible variations to determine the respective reduced χ^2 and the conversion factor k (see exemplary results for the RGA-I calibration function of the isotope ^{86}Kr in table 6.3).

The uncertainty Δk is now given by the maximum deviation of the obtained k factor, when R_V is changed:

$$\Delta k = k(R_V) - k(R_V \pm \Delta R_V) \tag{6.11}$$

In order to ensure a correct uncertainty calculation, a conservative choice is made, taking the larger discrepancy of $k(R_V \pm \Delta R_V)$, which is given by the variation $R_V + \Delta R_V$ (0.58×10^{-12}) instead of the variation by $R_V - \Delta R_V$ (0.48×10^{-12}) if calculated for the exemplary results from 6.3. This uncertainty has to be calculated for both isotopes separately. Also the application of both conversion factors $k(^{84}\text{Kr})$ and $k(^{86}\text{Kr})$ can be used, to check if the obtained concentration for a given sample match within the uncertainties, which is only fulfilled for signal ratios close to the natural isotopic fractions.

Table 6.3: Examplary determination of the conversion factor k and the uncertainty Δk for ^{86}Kr measured at the RGA-I setup.

	R_V	$R_V + \Delta R_V$	$R_V - \Delta R_V$
k $[\frac{A}{ppb}]$	3.30×10^{-12}	2.82×10^{-12}	3.88×10^{-12}
χ^2_{red}	2.06	1.46	2.94

RGA-I

For the calibration of the RGA-I setup dopings of 3260 ppb, 495 ppb, 81 ppb, 30 ppb, 2.4 ppb, 0.37 ppb and 0.06 ppb have been used. After applying the analysis steps previously described, the resulting calibration function can be seen in figure 6.14. By using the fit function, described in equation 6.10 and the uncertainty determination method from equation 6.11, a transformation relation with the conversion factor k can be determined in dependence of the chosen isotope:

$$k_{\text{RGA-I}}(^{84}\text{Kr}) = (1.112 \pm 0.195) \times 10^{-11} \, \tfrac{A}{ppb}$$
$$k_{\text{RGA-I}}(^{86}\text{Kr}) = (3.300 \pm 0.584) \times 10^{-12} \, \tfrac{A}{ppb}$$
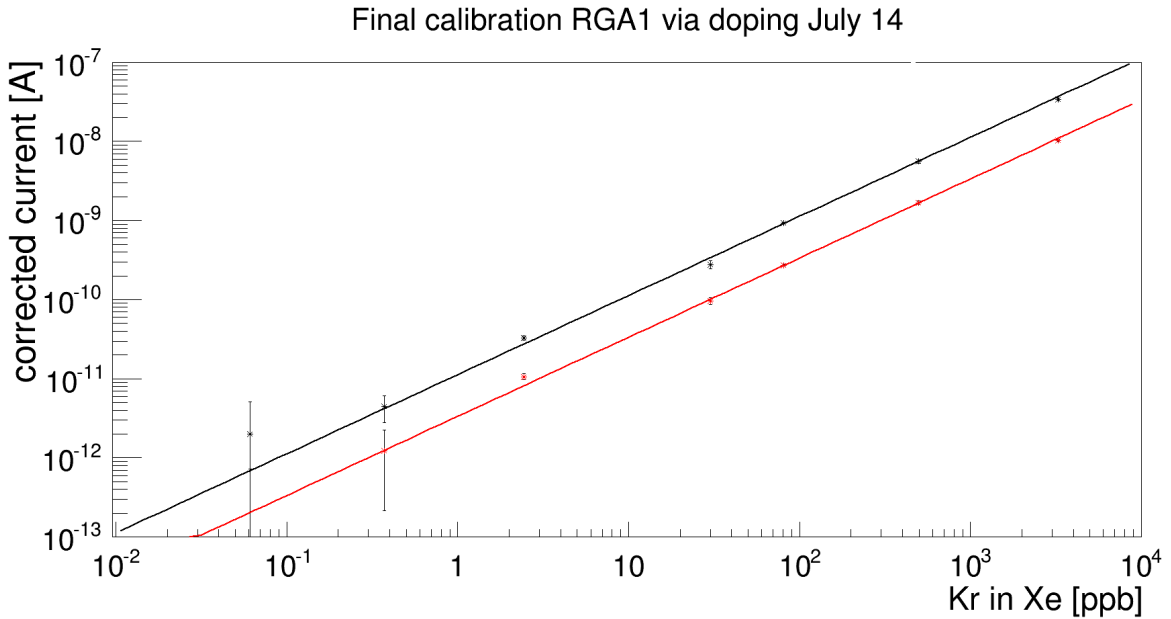
Figure 6.14: *Calibration function of the RGA-I setup. The relation of krypton concentration in xenon to the measured corrected signal strength for the isotopes ^{84}Kr and ^{86}Kr is shown from the sub-pbb to the ppm-level. The respective data is fitted with a fit function as described. While the uncertainty of the corrected current is obtained by the standard deviation of each signal, the uncertainty of the concentration is not included. For a better visualization both axis are on a logarithmic scale.*

RGA-II

Dopings of 9550 ppb, 1380 ppb, 216 ppb, 34 ppb, 5.8 ppb, 0.95 ppb and 0.16 ppb have been used for the RGA-II setup calibration. The resulting calibration data is shown in figure 6.15. An according determination of the respective k_{RGA1} gives:

$$k_{\mathrm{RGA\text{-}II}}(^{84}\mathrm{Kr}) = (1.488 \pm 0.258) \times 10^{-10} \, \tfrac{A}{ppb}$$
$$k_{\mathrm{RGA\text{-}II}}(^{86}\mathrm{Kr}) = (4.756 \pm 0.883) \times 10^{-11} \, \tfrac{A}{ppb}$$
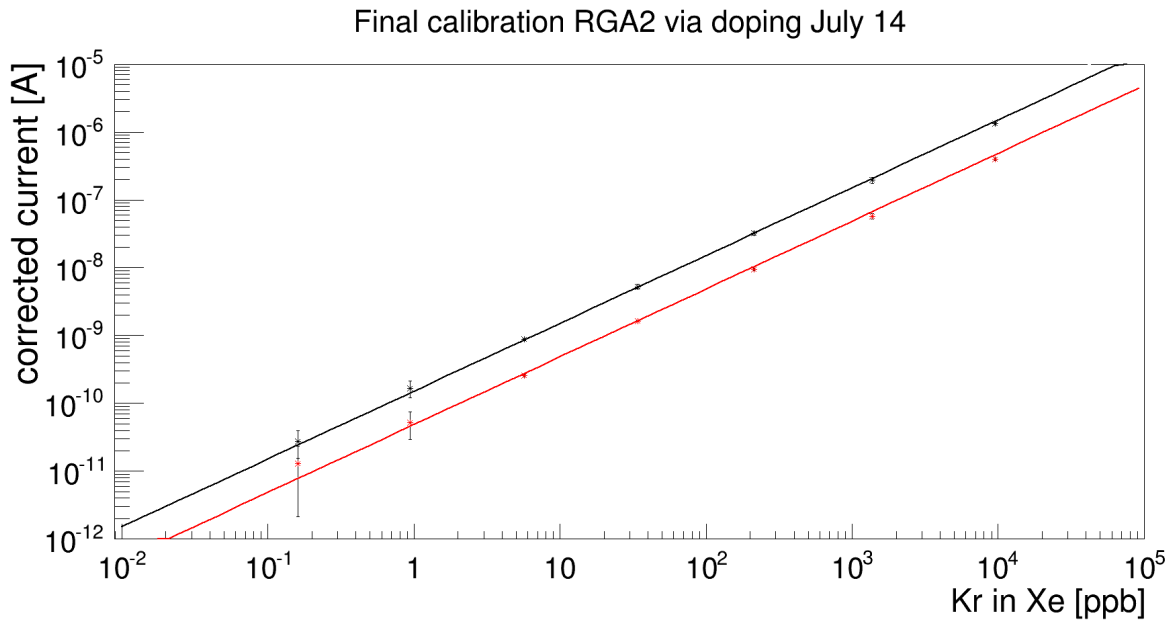

Figure 6.15: *Calibration function of the RGA-II setup. The relation of the krypton concentration in xenon to the measured corrected signal strength for the isotopes ^{84}Kr and ^{86}Kr is shown from the sub-pbb to the ppm-level. The respective data is fitted with a fit function as described. While the uncertainty of the corrected current is obtained by the standard deviation of each signal, the uncertainty of the concentration is taken into account separately as discussed. For a better visualization both axis are on a logarithmic scale.*

6.3.4 Sensitivity limit

A comparison of the two different setups and the respective conversion factors k reveals a difference in the order of one magnitude. The influence of this discrepancy on the sensitivity limits and the determination of this limits is discussed in the following section.

The calibration function 6.10 implies that as the concentration approaches zero, also the signal becomes zero. Although this is true for a real signal component, caused by krypton, the background level is constant and independent from the krypton concentration and therefore setting the limit of the respective RGA setup. Determination of this limit is from crucial importance for the understanding of the system and its future applications.

As described, the estimation of the sensitivity is correlated to an understanding of the background level inside the system. This can be obtained by an evaluation of measurements close to sensitivity limit and below. For this purpose the dopings with very low concentrations (sub-ppb) and additionally, measurements with ultra pure xenon (ppt-concentrations and below), provided by the distillation column, have been analyzed. These samples provide the advantage of a background dominated current. Figure 6.16 shows the measurement of seven presumably clean xenon samples, which have been taken from the distillation column and have been measured by the RGA-II setup. It is visible, that these fluctuate around a value less then zero, which indicates that these measurements are below the sensitivity limit but with almost constant error bars. While for the isotope ^{84}Kr this offset of $(-14.91 \pm 3.14) \times 10^{-11}\,\text{A}$ has been observed, it was not measurable for the isotope ^{86}Kr, where the fit provided a mean of $(-0.08 \pm 2.48) \times 10^{-12}\,\text{A}$ with a reduced $\chi^2_{\text{red}} = 0.3$. Note that only three measurements have been done for ^{86}Kr. As a result of this, it can be concluded that the uncertainties for ^{84}Kr are estimated correctly, while the uncertainties for ^{86}Kr seem to large. However, due to the low statistics and as large uncertainties lead to an underestimation of the sensitivity limit, this still can be used.

An estimation on the limit is now derived from the average of the uncertainties $\Delta \overline{I_s}$ of these measurements. This is reasonable, since a signal smaller then the uncertainty of the background can not be distinguished from the background fluctuations anymore without deep statistical analysis (see 8.3.2). Therefore the uncertainties of the low doping measurements and the purified xenon measurements, at the respective RGA setup, have been averaged for each isotope separately. Additionally, the signal height has been transformed into a minimal detectable concentration by using equation 6.10 for the specific isotope and RGA setup (see table 6.4). For the RGA-I the 1σ-sensitivity limit $S_{\text{RGA-I}}(^{84}84,^{86}86)$ has been calculated to:

$$S_{\text{RGA-I}}(^{84}\text{Kr}) = (206 \pm 35)\,\text{ppt}$$
$$S_{\text{RGA-I}}(^{86}\text{Kr}) = (318 \pm 58)\,\text{ppt}$$

Accordingly the 1σ-sensitivity limit $S_{\text{RGA-II}}(^{84}84,^{86}86)$ of the RGA-II setup has been determined to:

$$S_{\text{RGA-II}}(^{84}\text{Kr}) = (67 \pm 12)\,\text{ppt}$$
$$S_{\text{RGA-II}}(^{86}\text{Kr}) = (191 \pm 35)\,\text{ppt}$$

The uncertainty has been calculated by Gaussian error propagation of the equation 6.10, using the standard deviation σ for the averaged background fluctuations and the Δk obtained
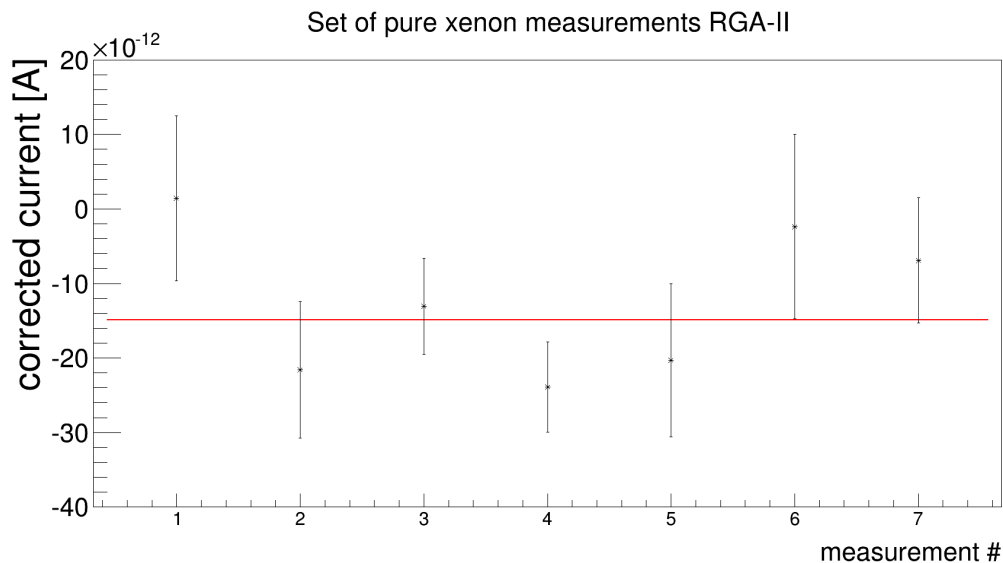
Figure 6.16: *Corrected current of ^{84}Kr for different purified xenon gas measurements. A linear fit (red) has been added with $\chi^2_{red} = 1.20$. As seen this fit does not match the zero line, which would be expected, instead of this, it is shifted towards negative values with an offset of $(-14.91 \pm 3.14) \times 10^{-12}$ A.*

in equation 6.11. The concentration sensitivity can also be seen graphically as the intersection of the sensitivity limit line and the calibration fit (see figure 6.17 for an example of the zoomed sector around the zero signal line for the RGA-I setup). Additionally it can be observed that the doping at 0.06 ppb, which is below the sensitivity limit of both isotopes for the RGA-I (see table 6.4), has a negative current. This is expected, since when a current is measured with a concentration below the sensitivity limit, it should fluctuate around the zero line with an uncertainty close to the sensitivity limit.

Discussion on the sensitivity

An aspect which has to be considered when estimating sensitivity limits, is the question for the inflow at the calibration of the systems. Although, all obtained signals are flow-corrected, the sensitivity still depends on the flow itself.

Given a sample with a concentration c_{kr}, this will lead to a signal I at the detector, which is dependent on the amount of particles in the detector. This amount changes with inflow, thus a doubled inflow leads to twice the signal intensity. As the calibration function corrects for this, it has no influence on the conversion factor k. However, if the signal is doubled, it can

Table 6.4: Estimation of the sensitivity limit S_{RGA} based on the average uncertainties $\Delta\overline{I_s}$ at low concentrations.

	$\Delta\overline{I_s}(^{84}\mathrm{Kr})$ [A]	$\Delta\overline{I_s}(^{86}\mathrm{Kr})$ [A]	$S_{\mathrm{RGA}}\ (^{84}\mathrm{Kr})$ [ppt]	$S_{\mathrm{RGA}}(^{86}\mathrm{Kr})$ [ppt]
RGA-I	2.90×10^{-12}	1.05×10^{-12}	206	318
RGA-II	1.00×10^{-11}	9.09×10^{-13}	67	191
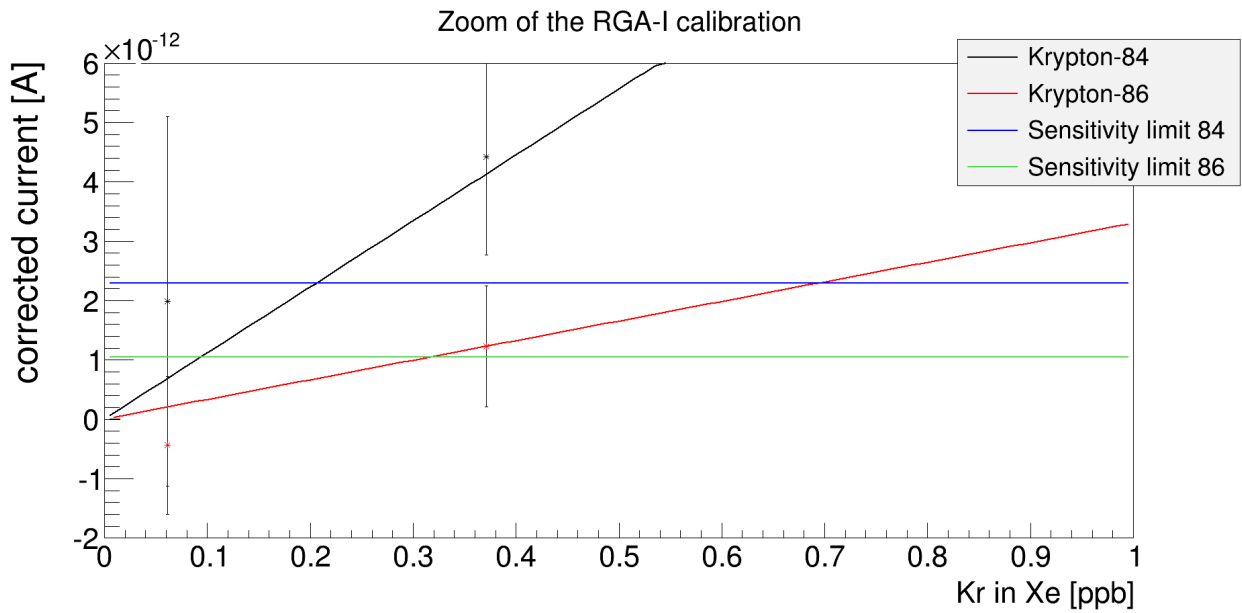
Figure 6.17: *Zoom into the RGA-I calibration plot. The sensitivity limits, obtained from the averaged uncertainties, are indicated by blue (^{84}Kr) and green (^{86}Kr) lines. The x-axis value of the intersection of these lines with the respective calibration fits in black (^{84}Kr) and red (^{86}Kr) marks the sensitivity limit of the RGA-I.*

overcome the background level, which is not dependent on the inflow, and thus be registered, where it would not be registered for a lower flow. Therefore, it has to be mentioned, that as the inlet pressure of the RGA-II setup has been reduced (around 500 mbar) compared to the RGA-I calibration (around 800 mbar), the inflows are comparable for the presented calibrations, as the RGA-II has a higher flow at same pressures (see 5.2.4 for a comparison of the flows through both systems).

DETERMINATION OF UNKNOWN KRYPTON CONCENTRATIONS

As the previous chapter showed, both setups are able to detect krypton on the sub-ppb level. This allows for screening measurements of xenon gas bottles for the XENON1T experiment provided by commercial suppliers. In the best case, these gas bottles have been tested by the companies itself down to 10 ppb, which can be controlled and quantified more precisely with the cold trap enhanced RGA method. Therefore gas bottles from three different companies have been tested and the results will be presented within this chapter. Additionally, first results will show the capability of the measurement method as a diagnostic tool for the cryogenic distillation column.

7.1 Cross check of the calibration of RGA-I and RGA-II

Before any further investigations have been made, the calibration of both setups has been tested with an artificially doped xenon gas sample of only roughly known krypton concentration c_{cross} ($\sim$ ppm). For a comparable measurement, the pipette was attached to the RGA-I setup and filled with this gas sample, while at the same time the measurement volume of the RGA-I setup was filled at equal pressure. The pipette was attached to the RGA-II setup and the gas was diluted into its measurement volume. Both RGA setups were filled with the same gas sample this way and thus, a cross check of both setups is possible. A determination of the concentration c_{cross} was performed using the previously described respective conversion functions. As a result of this, the concentration has been calculated two times for every setup (see table 7.1) in dependence of the two isotopes, and as these values are

Table 7.1: Determination of the concentration c_{cross}

	$c_{\mathrm{cross}}(^{84}\mathrm{Kr})$ [ppb]	$c_{\mathrm{cross}}(^{86}\mathrm{Kr})$ [ppb]
RGA-I	6479 ± 1148	6607 ± 1186
RGA-II	6378 ± 1143	5944 ± 1142

matching within the uncertainties, an average concentration $\overline{c}_{\mathrm{cross}}$ can be calculated for each RGA setup:

$$\overline{c}_{\mathrm{cross}}(\text{RGA-I}) = (6543 \pm 808)\,\text{ppb}$$
$$\overline{c}_{\mathrm{cross}}(\text{RGA-II}) = (6186 \pm 825)\,\text{ppb}$$

The matching concentrations is a relative cross check of the calibrations, showing that the same results are obtained, independent of the used RGA setup.

7.2 Gas bottle sample measurements

For test measurements of gas bottles with the RGA-I setup, pipettes have been filled at LNGS from gas bottles of two different companies (Praxair and Iceblick), which are designated for the filling of the XENON1T detector. Additionally, a xenon gas bottle from AirLiquide, which was used for gas operations at the distillation column at the Univserity of Münster, was measured several times with the RGA-II setup. The measurements can be compared with concentration levels, stated as upper limits $\overline{c}_{\mathrm{limit}}$ by the companies itself. In addition to this, measurement results from investigations made with the GC-RGMS setup (see chapter 4.3.2) can be compared to the results of the RGA setup measurements. Although, no results on the exact same bottles are provided, bottles from the same set of filling by a company have been measured, which have pressumably comparable concentrations (by at least one order of magnitude) [XEN14]. If more then one measurement on such a set was available, the comparison was done towards an average concentration extracted from this set.

The results (see table 7.2) show that the uncertainties of the Iceblick and Praxair are very large ($\sim 37.5\,\%$ and $\sim 47.5\,\%$), which is due to the low statistics provided as the region of interest has been measured for only $30\,\text{s}$, while usually at least $100\,\text{s}$ are used for averaging. Although the AirLiquide gas bottle could be measured three times, the difficulty was the low intrinsic concentration. This caused the signal of the isotope $^{86}\mathrm{Kr}$ to drop below the detection limit of the mass spectrometer shortly after gas injection. Thus, its current was read-out as zero, which prohibits a proper fitting as needed for the low-doping analysis. However, to account for this, two different approaches for analysis of this sample have been applied. First, the usual low-doping analysis was performed, as described in chapter 6.3.2, but only on a short time scale ($\sim 20\,\text{s}$), where the signal of $^{86}\mathrm{Kr}$ was present. This has the disadvantage of very low statistics and therefore a large uncertainty but provides the advantage of the isotopic fraction cross check, which clarifies if a signal is present or not.

The second approach uses the low-doping analysis only on the isotope $^{84}\mathrm{Kr}$, but on a large time scale (~ 400s). This provides high statistics, but no possibility of cross-checking the isotopic fraction. Despite that fact, this can also produce feasible results, because of the

Table 7.2: Results of the gas bottle sample measurements in comparison to GC-RGMS results and limits stated by the supplier

Company	$\overline{c}_{\text{measured}}$ [ppb]	$\overline{c}_{\text{limit}}$ [ppb]	$\overline{c}_{\text{GC-RGMS}}$ [ppb]
Iceblick	6.6 ± 2.1	<300	6.0 ± 2.7
Praxair	45 ± 21	<100	-
AirLiquide	0.20 ± 0.02	<10	0.40 ± 0.01

other clear signal-like signs compared to the background-dominated masses (see figure 7.1). Due to the fact that this gas sample was measured three times, a mean concentration $\overline{c}$ can be calculated for both approaches. Therefore, the obtained concentrations have been averaged and the respective uncertainties $\Delta\overline{c}$ have been calculated by Gaussian error propagation. For the first analysis approach, the concentrations $\overline{c}_1$ of both isotopes are evaluated as:

$$\overline{c}_1(^{84}\text{Kr}) = (186 \pm 54)\,\text{ppt}$$
$$\overline{c}_1(^{86}\text{Kr}) = (196 \pm 60)\,\text{ppt}$$

As the concentrations match within the uncertainty, it can be stated that the isotopic fractions match. Moreover, it can be seen that the determined concentration is within the sensitivity limit of ^{86}Kr (191 ± 35) ppt at the RGA-II, which can explain the signal vanishing for this isotope. This is confirmed by the results given by the second approach:

$$\overline{c}_2(^{84}\text{Kr}) = (199 \pm 21)\,\text{ppt}$$

While the result is matching the previously calculated values, the relative uncertainty is decreased by a factor 3 from about 30 % to 10 %.

Summarizing the results, it can be seen that all upper limits stated by the companies are confirmed. Furthermore, the Iceblick sample matches the comparable GC-RGMS measurements, while the AirLiquide is not matching within the uncertainties. It has to be noted that the Iceblick bottle sets have been measured five times by the GC-RGMS, while there is only one result for the AirLiquide bottle. However, as the order of magnitude is confirmed, it is possible that the other bottle from this set had a slightly different composition. Another possibility is a non-uniform krypton concentration within a gas bottle, as this was observed several times for artificially doped gas bottles. A sample of the exact same bottle has been prepared for measurements with the GC-RGMS at the MPIK Heidelberg and the ATTA-setup at the Columbia University, but were not finished in the scope of this thesis.

7.3 Determining a separation factor for the distillation column

A possible application of the setup is the characterization of the cryogenic distillation column during operation. Therefore, the distillation column has different gas outlets for analysis
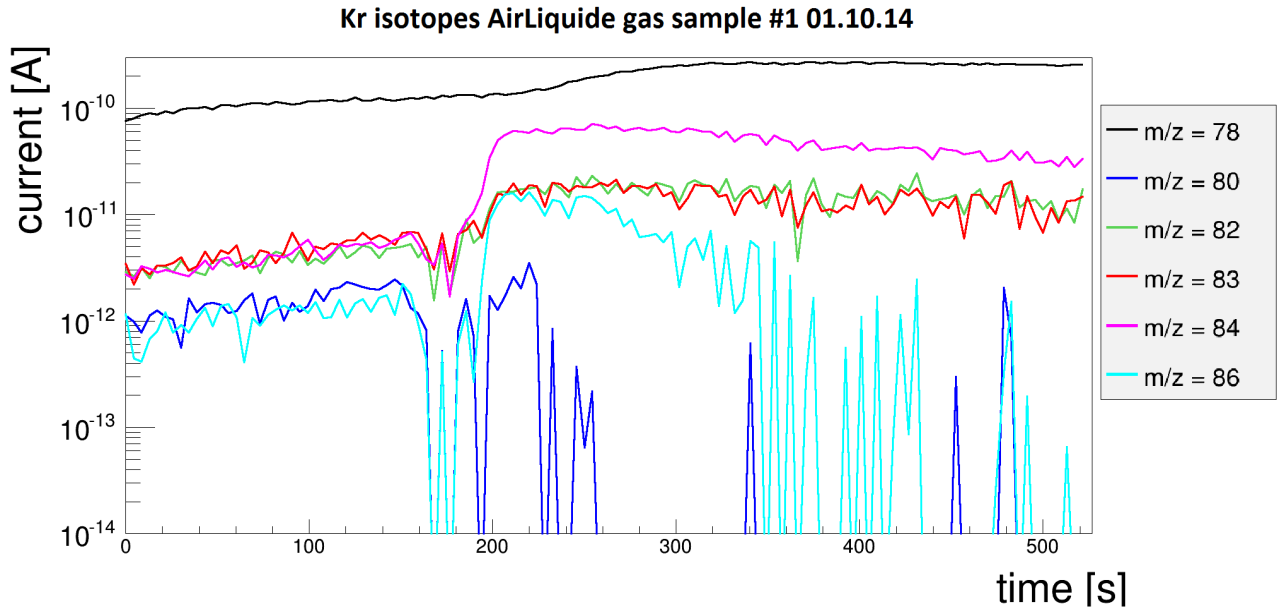
Figure 7.1: *Current time evolution for the first measurement of the AirLiquide gas sample. The ^{84}Kr signal-like m/z = 84 (pink), is clearly having a different behavior than the background dominated m/z = 78 (black). Additionally, it can be seen that the signal at the mass-over-charge ratio of ^{86}Kr (lightblue), is rising in the beginning but falls fast below the detection limit of the mass spectrometer.*

purposes. The most important characteristic of the distillation column, is the separation factor S_f. This key parameter quantifies the difference in krypton concentration between inlet and outlet of the column [Ros14a]. The most stringent way to obtain this parameter, is a measurement of the concentration at the inlet and of the outlet during the same distillation process. Hence, gas samples have been drawn live at operation from the in-going gas and the out-going gas and have been measured with the RGA-I setup[1]. The concentration determination of the inflow provides a clear krypton signal revealing a concentration $\overline{c}_{in}$ of (5963 ± 885) ppb within this gas. However, the concentration determination of the outgoing gas, which is supposedly purified, was not possible, as the current of all isotopes is background dominated in figure 7.2. Application of the low-analysis doping method to this sample provides the following parameter from its fit for the signal mean $\overline{I}_s$ of the respective isotope:

$$\overline{I}_s(^{84}\text{Kr}) = (8.5 \pm 9.1) \cdot 10^{-13}\text{A} \tag{7.1}$$

$$\overline{I}_s(^{86}\text{Kr}) = (-2.8 \pm 4.7) \cdot 10^{-13}\text{A} \tag{7.2}$$

---

[1]The more sensitive RGA-II setup could not be used due to the gas routing.
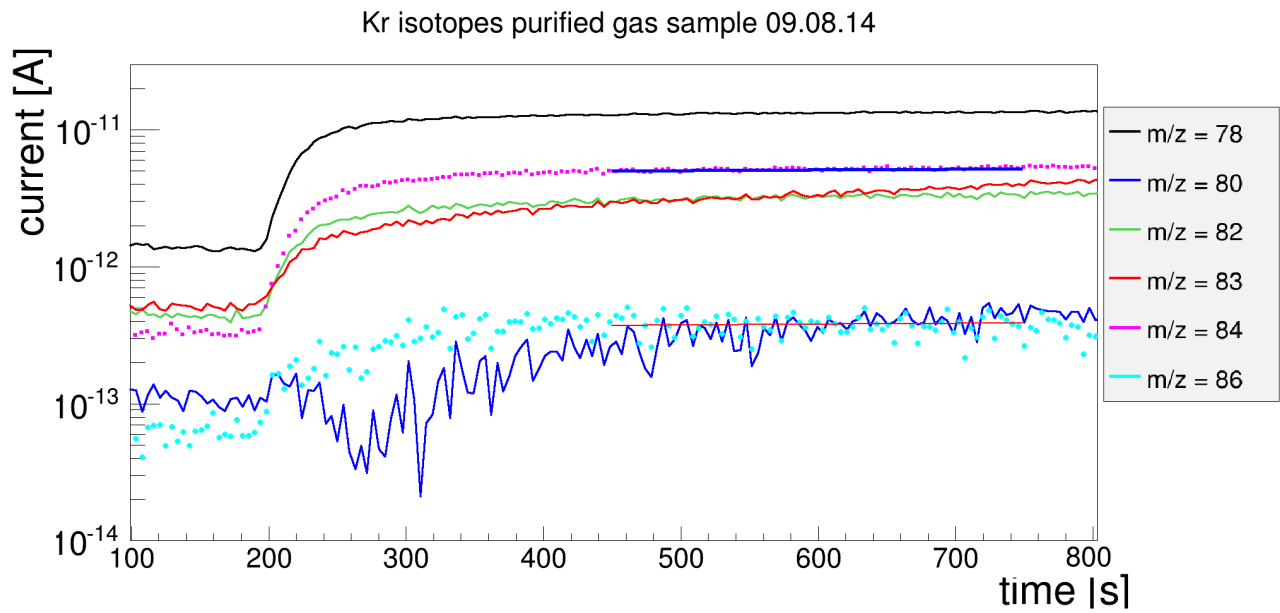
Figure 7.2: *Current time evolution for a purified sample from the outlet of the distillation column. The two signals of interest at ^{84}Kr (pink) and ^{86}Kr(light blue) have been fitted with the function from equation 6.10. The fitting parameter point towards no signal detection, as also indicated by the raising signal behavior.*

As this is clearly within the uncertainty of the background and therefore, also below the sensitivity limit, a direct determination of the separation factor is not possible. Nevertheless, the obtained results allow for an estimation of a lower limit. If the krypton concentration $\overline{c_{\mathrm{in}}}$ is compared to the sensitivity limit of the detector $S_{\mathrm{RGA\text{-}I}}\left(^{84}\mathrm{Kr}\right)$ a separation factor limit is given by:

$$S_f = \frac{\overline{c_{\mathrm{in}}}}{S_{\mathrm{RGA\text{-}I}}\left(^{84}\mathrm{Kr}\right)} \tag{7.3}$$

With the sensitivity limit $S_{\mathrm{RGA\text{-}I}}\left(^{84}\mathrm{Kr}\right)$ of about $0.2\,\mathrm{ppb}$, this leads to a lower limit for S_f of:

$$S_f > 30000$$

DISCUSSION & OUTLOOK

Although it has been demonstrated that a reliable, fast concentration determination is possible, some further investigations can be done, as well as improvements to the system for an increase of the sub-ppb sensitivity limit. This chapter will provide a discussion on different aspects of the thesis, but also emphasizing possible future aspects of improvement and evaluation.

8.1 The influence of the gas composition

During careful investigation of the system the question arised, whether if there is an influence of other impurities to the system response on krypton. As chapter 6.1.1 showed, an increase in vapor pressure is directly related to the level of impurities, but it has still to be investigated, if the krypton signal is affected by the impurity level. Moreover, the reproducibility of the system for changing the total pressure in the measurement chamber, which is directly related to the cold trap pressure, has not been demonstrated yet. Measurements for an evaluation on this, can be performed, using the installed butterfly valve, which allows for a control of the pressure inside the measurement chamber. Although, theoretically it is expected that the signal intensity is directly correlated to the effective pumping speed reduction by the butterfly valve, a research on the influence of the opening position has still to be performed. Therefore, a first test measurement of the signal at two different butterfly valve positions has been made (see 8.1). This measurement was started with a 15° opening at the RGA-I and within the measurement, the butterfly valve was closed to 0°. As expected the signal shows a uniform increase within the different isotopes, with a factor of about 7.5.
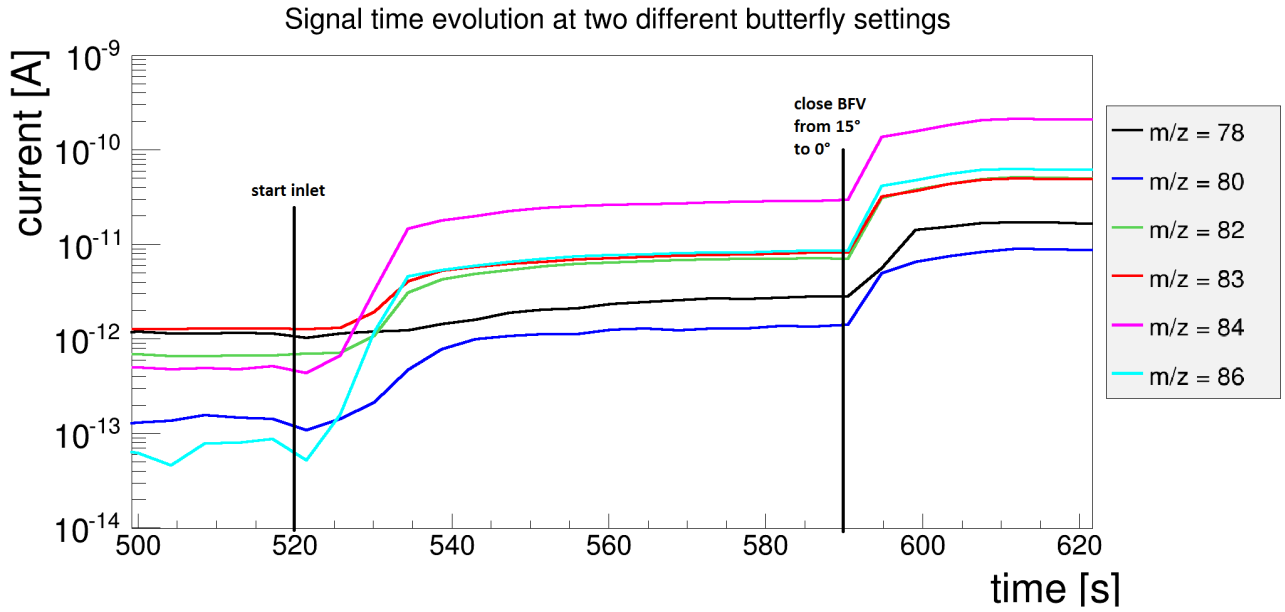
Figure 8.1: *Signal time evolution for different butterfly settings, with indicated changes of the butterfly valve position. Before the closure of the butterfly valve it was set to 15°.*

This is a small discrepancy compared to the factor 5.2 of pumping speed reduction obtained from table 5.1. Hence, a statistical reliable measurement set is needed for the determination of a correction factor for the butterfly valve position. Once this is done, an analysis of the signal dependency on the gas composition can be performed. The measurement of other impurities, besides krypton, shows a possible use of the RGA setups as a detector for other contamination, as long as its partial pressure is below its vapor pressure (see [Leo10]). This can be applied as a tool to characterize the working performance of the distillation column, if the krypton concentration determination comes to its limit. This can be achieved by measuring for example the argon concentration at different outlets, and by this, make a qualitative statement about working stability, as this is directly correlated to the specific separation efficiency.

8.2 Quantifying unknown concentrations

The main task of the presented measurement method lies in the quantification of unknown krypton concentrations in given gas samples. As the uncertainty Δk of the conversion factor k, obtained through calibration, is always around 18%, a single measurement of the concentration will always have at least this uncertainty. Therefore, if possible an increased precision can be achieved by measuring a given gas sample more then once. For a future reduction of the uncertainty Δk, a calibration with increased statistics will be needed or a different approach for uncertainty calculation has to be developed. However, for screening purposes, where only the order of magnitude of the contamination is required, one measurement is sufficient to determine a concentration value fast, reliable and without consuming

noteworthy amounts of xenon.

8.3 The sensitivity limit

Besides the aspect of mobility, the RGA-II setup was also designed for an improved sensitivity. This has been achieved, as the RGA-II setup is a factor of 3 more sensitive ($S_{\text{RGA-II}} = 67\,\text{ppt}$) to the signal of ^{84}Kr as the RGA-I setup ($S_{\text{RGA-I}} = \text{SI206ppt}$. Nonetheless, the achieved sensitivity can still be improved, especially, as the experimental apparatus was designed with the reasonable premise of non-freezing xenon. As this was disproved within this thesis (see 6.1.1), the focus for improvements can be redirected to sensitivity enhancement. There are basically three possible ways to optimize the sensitivity, which are all based on an improvement of the signal-to-noise ratio:

- Improvement of the xenon freezing.

- Reduction of the background signal.

- Increase of the introduced krypton amount.

8.3.1 Improvement of the xenon freezing

While it was shown, that the xenon freezes down to its vapor pressure and as consequence a krypton concentration enhancement was possible, it only was performed at liquid nitrogen temperature $77\,\text{K}$. If the temperature is decreased, the krypton concentration will be increased further as long as the vapor pressure of the krypton is not achieved. This due to the fact that more and more xenon particles freeze, but as long as krypton is unaffected, the amount of krypton particles will stay constant. For example, at about $59\,\text{K}$ the vapor pressure of xenon is approximately at $10^{-6}\,\text{mbar}$, while krypton is still at $10^{-2}\,\text{mbar}$ [Wut06], which is above the vapor pressure for a ppt-level of krypton in $1\,\text{bar}$ xenon. This way a further increase by three orders of magnitude for the krypton concentration could be achieved. A strong disadvantage is the technical difficulty (pumping on the LN_2) or the costs (use of liquid helium or a new setup design). Therefore, the other two ways of a sensitivity enhancement should be in the focus of further work.

8.3.2 Reduction of the background signal

Neglecting an exchange of the used mass spectrometer, the possibility to reduce the background by any technical approach is limited. For the RGA-II setup intensive baking has been executed, as well as flushing with clean gas, but any further background reduction is small compared to the time scale needed for it. Therefore, not a decrease of the background signal, but an intensive understanding of the background should in the spotlight.

For measurements close to the sensitivity limit, some of the krypton mass signals consist only of background. By understanding the time behavior of these signals, a discrimination
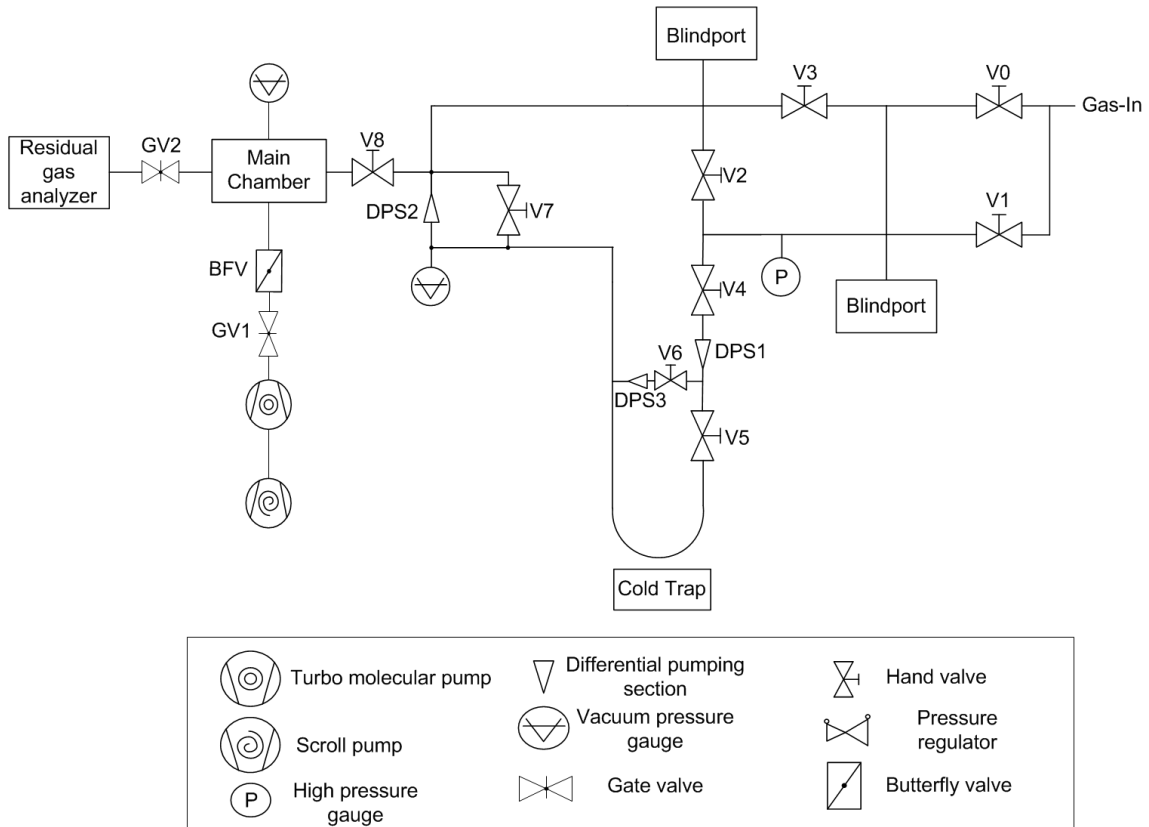
Figure 8.2: *Complete flow chart for the mobile online detection setup, referred as RGA-II setup. The DPS3, at the bypass of the cold trap, is not implemented yet, but is planned to be used for analysis of other impurities.*

of the background fraction from the real signal component can be established. Therefore, investigative measurements with an analysis of the background have to be done. Especially taking the observation into account, that some signals rise, even if no krypton is present (see 6.3.4), which points towards background effects still not completely understood.

In addition to this, measurements with high statistics provide the possibility to distinguish a real signal from a noise-like background behavior. Hence, an analysis method of discrimination has to be developed and measurements with an increased time consumption will be necessary. This will need also a better understanding of the flow correction, as the flow behavior changes at low pressures, which are achieved at long measurements.

8.3.3 Increase of the krypton amount

The most stringent way to enhance the signal strength in dependency of the in-going krypton concentration, is to increase the amount of krypton entering the mass spectrometer. As the advantage of the cold trap supported RGA method is the low consumption amount of expensive xenon gas (about 0.1 sl per measurement), other possibilities have to be considered, instead of a change in the used gas amount. A first approach without any system changes is to make use of an advantageous characteristic at the RGA-II setup. As seen in the flow
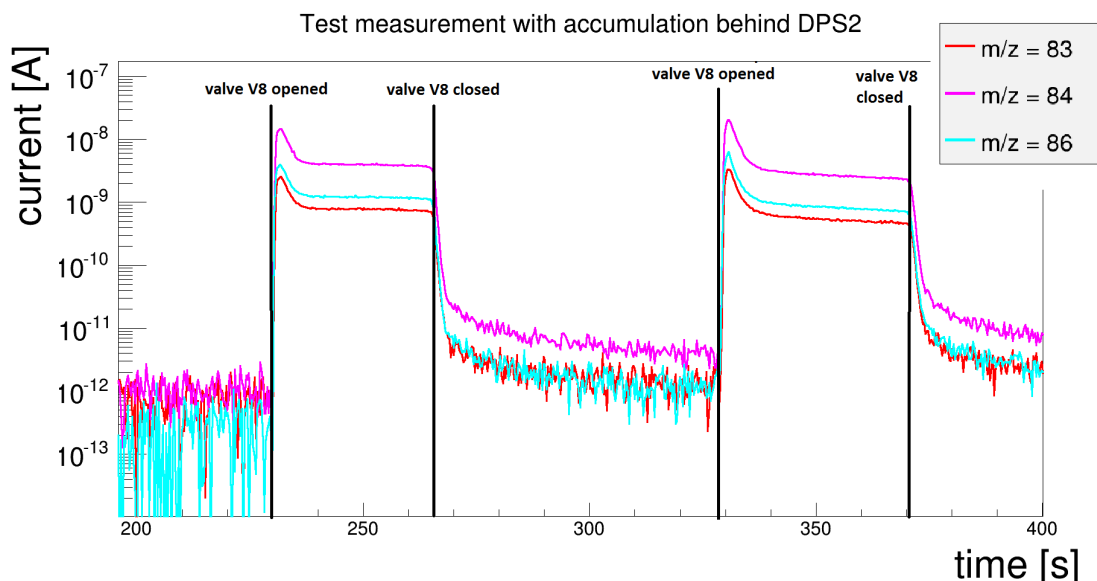
Figure 8.3: *Signal time evolution for a test run of the accumulation method. Two times the accumulation valve V8 was closed and opened. A clear overshoot for three krypton isotopes is observable directly after opening V8. This test run was performed with a highly doped sample at the RGA-II setup.*

chart in figure 8.2, the measurement chamber is connected via a valve (V8) to the rest of the system, which is fully open during the standard measurement process. This brings up the possibility to close this valve during injection of the gas sample into the cold trap, in order to prevent the gas to enter directly the measurement chamber. While the krypton is accumulated over time, the xenon should freeze down to its vapor pressure constantly as long as the surface of the cold trap is sufficient. If V8 is opened, a large amount of krypton is injected at once, instead of being introduced over a longer period of time, which causes a more intense signal at valve opening. The problem within this approach lies in the fact, that the DPS2 is surpassed by a fraction of the gas, and thus a higher inflow to the measurement chamber is produced. Since this is a problem limited to the time directly after opening the valve, as only the gas in the volume between V8 and the DPS2 is flowing fast into the measurement chamber, the residual gas analyzer might be still able to operate as expected. Hence, measurements obtaining the maximum possible accumulation time are necessary, and if this method is working, a new calibration will be required. A first test measurement, with the proof of an increasing signal, can be seen in figure 8.3. The overshoot in signal at the valve opening has to be measured in further investigations as a function of accumulation time and intrinsic concentration. A derivation of this method, eliminating the problem of the surpassed DPS2, is to use another extra valves (V5, V6) implemented in the RGA-II setup already (see figure 8.2). If the valves V6 and V5 are closed, while valve V4 is open, the gas from the measurement volume V_{meas} will accumulate in the volume between those three valves and this way the DPS1 is surpassed. By opening V5 completely for a measurement, the inflow into the cold trap is increased for a short period of time until the volume behind the DPS1 is emptied. Depending on the accumulation time and the freezing capabilities, the vapor pressure will be achieved and only an increased amount of krypton will reach the

measurement chamber but still through the DPS2, which grants a safe inflow in terms of overpressure at the RGA. Nevertheless, this approach has the disadvantage of using only a small extra amount of gas, which surpasses the DPS1, thus the signal enhancement could be not sufficient. Additionally, a flow correction is not as easy executable as for the already existing measurement method, since the pressure sensor is mounted before the DPS1.

Both techniques can be tested without a modification of the system, but also techniques with small changes to the system can possibly provide an improvement in sensitivity limit. If the DPS1 is exchanged with a differential pumping section of a higher conductance (as e.g. a DPS2-like), it will cause a higher in-flow. As long as the cold trap is freezing the in-going xenon down to its vapor pressure, this will lead to reliable measurements comparable with the calibrated ones within this thesis. The signal height will increase, due to the increased krypton amount, while the xenon flow into the measurement chamber stays the same, as the dominating component will freeze to the same level as before. This provides a flow-correctable signal time evolution with an increased signal height, and as the background should not change with the flow, an improvement in the sensitivity limit. Theoretically, an increase of the flow by a factor of 10 should also enhance the sensitivity limit by this factor, as long as the cold trap works as expected, which has to be carefully tested.

Another possible modification, with small changes to the system, can increase the sensitivity by adding an additional differential pumping section DPS4 and another valve V9, as shown in the modified flow chart in figure 8.4. In addition to this, the already existing DPS are obsolete for this version of the setup and have to be removed. The idea behind this changes, is an operation of the system like a cryo-pump. A fixed amount of gas is introduced into the system, with all valves to the measurement chamber closed. By attaching the cold trap, the xenon from the complete system gas will freeze down to its vapor pressure, assuming the freezing capability of the cold trap is sufficient. When the vapor pressure is reached, the valve V9 is opened and a reduced flow will enter the measurement chamber due to the additional differential pumping section DPS4. The inflow into the DPS4 should be higher then in the classical approach but as the pressure is same, the increase in inflow is only amplified by the larger input volume, which even can be controlled by using different valves. The advantage of these measurement method is the possibility to wait for an equilibrium and thus remove the dynamics of the system. A flow correction will not be necessary, as long as the size of the gas samples within different measurements stays constant and if the vapor pressure is achieved. The krypton signal should be at its maximum, as the equilibrium state of the setup should achieve the highest separation efficiency.
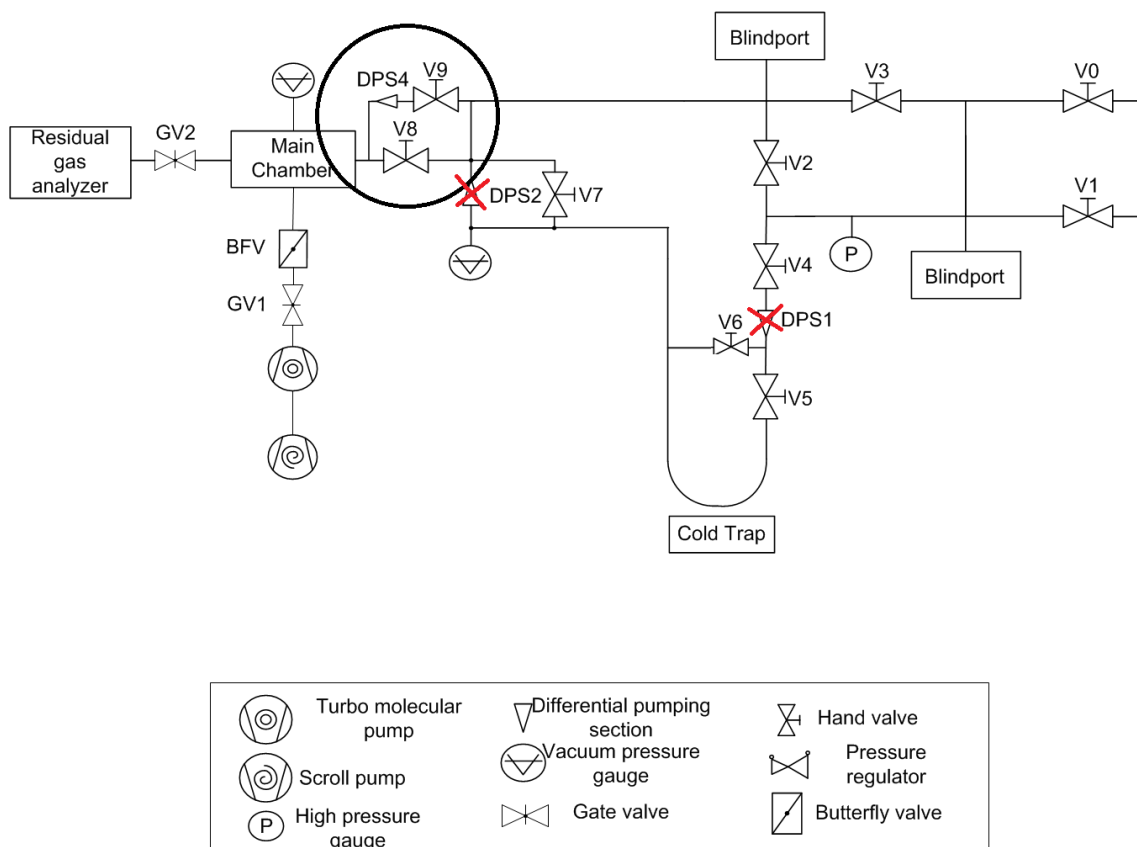
Figure 8.4: *Modified flow chart with an additional added differential pumping section DPS4 and another valve V9 (marked by the black circle). This system is not used in dynamic mode, thus the DPS1 and DPS2 are not necessary.*

Conclusion

Motivated by the existence of dark matter, being introduced in the second chapter, the XENON dark matter experiment is presented in the following section. This international collaboration searches for a dark matter particle candidate, the WIMP, in the Gran Sasso National Laboratory, 3100 meter water equivalent deep in the Gran Sasso mountain, using a dual-phase time projection chamber filled with liquid xenon. Preparing the next stage of this experiment, XENON1T, the University of Muenster is participating in this project, being responsible for the development and building of a cryogenic distillation column, which is able to purify xenon from krypton down to the sub-ppt level. As described in chapter 4 this is necessary due to the intrinsic impurity ^{85}Kr, which produces one significant background for the direct dark matter search. Due to the extremely low abundance in natural krypton ($10^{-11} \frac{^{85}\text{Kr}}{^{\text{nat}}Kr}$, the determination of the Kr-85 concentration is very limited, as the natural krypton is already only abundant in traces within xenon. However, since the ratio of natural krypton and the radioactive ^{85}Kr is constant, a determination of the natural krypton amount in xenon gas is sufficient. Nevertheless, the detection of natural krypton in sub-ppb traces is challenging to no lesser extent, although different experimental approaches have already proven to be able to measure even below this level as shown in chapter 4. As these methods have in common that either the xenon consumption or the measurement time are disadvantageous, an alternative online measurement method, the cold-trap enhanced RGA measurement method, has been introduced in chapter 5. Additionally, investigations and the application in a new mobile system (RGA-II), dedicated to the direct use at XENON1T, have been presented in detail. This included the evaluation of the cold trap behavior at different gas compositions. Within these measurements a vapor pressure of 3.3×10^{-3} mbar for pure xenon at 77 K could be determined.

For a careful calibration of this new setup and an already existing system (RGA-I), a special artificial doping method was used, as explained in chapter 6. Within this doping procedure

an observation of the krypton diffusion time in xenon gas was made, pointing towards an unexpected diffusion time scale. Therefore, an investigation with the usage of the radioactive isotope ^{83}Kr was performed, confirming diffusion time scales of several hours. Taking this into account, the calibration of the two systems worked properly and confirmed the expected linear behavior of signal height and concentration. The developed analysis methods for high and low concentrations have been explained within chapter 6, as well as the sensitivity limit on the determination of natural krypton. These sensitivities could be quantified below the ppb-level for both setups, with a maximum sensitivity for the natural krypton detection at the RGA-II setup of 67 ppt.

Application of the measurement method, namely gas-bottle screening and the online characterization of the operating distillation column for the XENON1T experiment, are the topics of chapter 7. These measurements have shown a successful measurement of different gas bottles, including a sample with a sub-ppb contamination, quantified as (199 ± 21) ppt by the RGA-II setup. Concluding, different approaches for improvement and further investigation have been introduced in chapter 8. Mentioning one, a possible gain in sensitivity by newly developed approaches of gas accumulation has been presented, being testable even without modifying the system physically.

BIBLIOGRAPHY

[Ang08] J. Angle et al. XENON Collaboration, First Results from the XENON10 Dark Matter Experiment at Gran Sasso National Laboratory Phys. Rev. Let. 100, 021303 (2008)

[Apr09] E. Aprile and T. Doke, Liquid Xenon Detectors for Particle Physics and Astrophysics, Rev.Mod.Phys.82:2053-2097,2010, arXiv:0910.4956v1, (2009)

[Apr10] E. Aprile (XENON1T), XENON1T at LNGS, Technical Design Report, October 2010

[Apr11] E. Aprile et al. (XENON100), Study of the electromagnetic background in the XENON100 experiment, Phys. Rev. D 83, 082001 (2011), arXiv:11101.3866

[Apr12a] E. Aprile et al. (XENON100), Dark Matter Results from 225 Live Days of XENON100 Data, Phys. Rev. Lett. 109, 181301 (2012), arXiv: 1207.5988

[Apr12b] E. Aprile et al. (XENON100), The XENON100 Dark Matter Experiment, Astropart. Phys. 35 (2012), 573-590 , arXiv:1107.2155

[Apr13] E.Aprile et al., An Atom Trap Trace Analysis System for Measuring Krypton Contamination in Xenon Dark Matter Detectors, Rev. Sci. Instr. 84, 093105 (2013)

[Apr14] E.Aprile et al., Conceptual design and simulation of a water Cherenkov muon veto for the XENON1T experiment, arXiv:1406.2374 (2014), called 11.08.2014

[Bab39] H.Babcock, The Rotation of the Andormeda Nebula, PhD thesis, University of California (1939)

[Beg91] K. G. Begeman et al., Extended rotation curves of spiral galaxies - Dark haloes and modified dynamics, Mon. Not. R. Astron. Soc. 249 (1991) 523

[Bel08] P. Belli et al., First results from DAMA/LIBRA and the combined results with DAMA/NaI, Eur.Phys.J.C56:333-355, 2008

[Ber04] G. Bertone et al., Particle Dark Matter: Evidence, Candidates and Constraints, Phys. Rep. 405 (2005) 279-390

[Bie09] J. Bieringer et al., Trace analysis of aerosol bound particulates and noble gases at the BfS in Germany, Applied Radiation and Isotopes,Volume 67, Issue 5, Pages 672–677, 2009

[Bra08] M. Bradac et al., Revealing the Properties of Dark Matter in the Merging Cluster MACS J0025.4-1222, The Astrophysical Journal, Volume 687, Issue 2, pp. 959-967

[Bro13] E. Brown et al., In situ measurements of Krypton in Xenon gas with a quadrupole mass spectrometer following a cold-trap at a temporarily reduced pumping speed, 2013 JINST 8 P02011, arXiv:1212.5136, 2013

[Bul14] E. Bulbul et al., Detection of An Unidentified Emission Line in the Stacked X-ray spectrum of Galaxy Clusters, accepted for publication by ApJ, arXiv:1402.2301 (2014)

[Clo06] D. Clowe et al., A direct empirical proof of the existence of dark matter, The Astrophysical Journal, Volume 648, Issue 2, pp. L109-L113, 2006

[Dob11] A. Dobi et al., Detection of krypton in xenon for dark matter applications, Nucl. Instr. Meth. Phys. Res., Volume 665, 11 February 2011, Pages 1–6

[Du03] X. Du et al., A new method of measuring ^{81}Kr and ^{85}Kr abundances in environmental samples, Geophys. Res. Lett., 30 2068, 10/2003

[ESA10] ESA/Hubble and NASA, http://www.spacetelescope.org/images/potw1032a/, downloaded on 23.06.14

[Esm12] A. Esmaili, O. Peres, KATRIN sensitivity to sterile neutrino mass in the shadow of lightest neutrino mass, Physical Review D - Particles, Fields, Gravitation and Cosmology ,Volume: 85, Issue: 11, (2012)

[Exo11] EXO Collaboration, Observation of Two-Neutrino Double-Beta Decay in Xe136 with the EXO-200 Detector, Phys. Rev. Lett. 107, 212501 – Published 17 November 2011

[Gro11] J. Gross, Mass spectrometry. A textbook., Springer Verlag, 2011

[Gel10] Graciela Gelimini and Paolo Gandolo, DM Production Mechanism, 2010

[Han11] V.Hannen et al.: Limits on the release of Rb isotopes from a zeolite based ^{83m}Kr calibration source for the XENON project, 2011 JINST 6 P10013 (2011)

[Ho12] S. Ho et al., Clustering of Sloan digital sky survey III photometric luminous galaxies: the measurement, systematics, and cosmological implications. ,Astrophys. J., 761, 14 (2012)

[Inf99] Inficon, Technical Note, 1999

[Inf04] Inficon, Technical Note, 2004

[Inf09] Inficon, Transpector 2 Brochure, 2009

[Jun96] G. Jungman et al., Supersymmetric Dark Matter, Phys. Rept., 267 (1996) 195-373

[Kam97] M. Kamionkowksi, WIMP and Axion Dark Matter, arXiv:hep-ph/9710467 (1997)

[Ket12] H. Kettling, Trace Gas Analysis of Krypton for the XENON Dark Matter Project, diploma thesis, University of Münster (2012)

[Kuz08] R. Kuzio de Naray et al.,Mass Models for Low Surface Brightness Galaxies with High-Resolution Optical Velocity Fields, ApJ 676 920, 2008

[Leo10] D.S. Leonard et al., A simple high-sensitivity technique for purity analysis of xenon gas, Nucl. Instr. Meth. Phys. Res., Volume 621, Issues 1–3, 1–21 September 2010, Pages 678–684

[Lev14] C. Levy, Light propagation and Reflection off Teflon in Liquid Xenon Detectors for the XENON100 and XENON1T Dark Matter Experiments, PhD thesis, University of Münster (2014)

[Lid07] D.R. Lide, CRC Handbook of Chemistry and Physics, 87th edition, CRC press, 2006-2007

[Lin13] S. Lindemann, Intrinsic Kr^85 and Rn^222 backgrounds in the XENON dark matter search, PhD thesis, University of Heidelberg 2013

[Lin14] S. Lindemann and Hardy Simgen, Krypton assay in xenon at the ppq level using a gas chromatographic system and mass spectrometer, Eur. Phys. J. C 74:2746, 2014

[LUX13a] LUX Collaboration, First Science Results from the LUX Dark Matter Experiment, http://luxdarkmatter.org/talks/20131030_LUX_First_Results.pdf, 2013

[MKS08] mks Baratron Manometer data sheet, mks company, 2008

[MKS12] Operational and Installation Manual for 972B DualMag^{TM} Vacuum pressure transducer, mks company 2012

[MKS14] Gas correction factors for vacuum gauges, http://www.mksinst.com/docs/ur/mfcGasCorrection.aspx acessed on 28.09.14

[Mur14] M. Murra, Set up and test of a cryogenic distillation column for the XENON1T experiment, Master thesis, University of Münster (2014)

[Ost03] J. P. Ostriker and P. Steinhardt, New Light on Dark Matter, Science 300 (2003) 1909

[Oer08] Oerlikon Leybold, PENNINGVAC PTR90, operating manual, 02/2008

[Pla13a] Planck Collaboration, Planck 2013 results. XVI. Cosmological parameters, arXiv:1303.5076 (2013)

[Pla13b] Planck Collaboration, Planck 2013 results. XV. CMB power spectra and likelihood, arXiv:1303.5075v2, 2013

[Pfe14] Pfeiffer Vacuum, www.pfeiffer-vacuum.com/know-how, called on 30.09.2014

[Ros14a] S.Rosendahl, PhD thesis, expected 2014

[Ros14b] S.Rosendahl, pre-separator paper in development, to be published in 2014

[Ros14c] S.Rosendahl, A novel ^{83}Kr tracer method for characterizing xenon gas and cryogenic distillation systems arXiv:1407.3981 (2014)

[Rot14] D. Roth, Kalibrationsaspekte der kryogenen Destillationssäulee für das XENON1T-Experiment, bachelor thesis, University of Münster (2014)

[Sch11] J. Schulz, Design of a 2-Phase Time Projections Chamber for Electron Drift Length Measurements, diploma thesis, University of Münster (2011)

[Sch12] M. Schlak, Calibration Methods for the XENON1T Distillation Column for the Xenon Dark Matter Experiment, bachelor thesis, September 2012

[Sel12] M. Selvi (XENON1T collaboration), Independent calculation of the number of background events due to Kr85 in LXe, internal note, 2012

[Sto14] D. Stolzenburg, On the krypton background in the XENON100 and XENON1T dark matter search experiments, Master thesis, University of Heidelberg, 2014

[Wut06] K.Jousten(Hrsg.), Wutz Handbuch Vakuumtechnik - Theorie und Praxis, 9. Auflage, 2006

[XEN14] XENON1T internal documents, in courtesy of the Xenon-Collaboration (2014)

[Zwi37] F. Zwicky, On the Masses of Nebulae and of Clusters of Nebulae, Astrophys. J. 86, 217, (1937)